The Dissertation Committee for Zachary Ryan McCarty Certifies that this is the approved version of the following dissertation:

From small molecules to macromolecules: design, synthesis, and evaluation of functional organic materials.

Committee:

C. Grant Willson, Supervisor

Carlos R. Baiz

Jennifer S. Brodbelt

Nathaniel Lynd

Dmitrii E. Makarov

From small molecules to macromolecules: design, synthesis, and evaluation of functional organic materials.

by

Zachary Ryan McCarty

Dissertation

Presented to the Faculty of the Graduate School of

The University of Texas at Austin

in Partial Fulfillment

of the Requirements

for the Degree of

Doctor of Philosophy

The University of Texas at Austin

May 2018

Acknowledgements

I first would like to thank my advisor, Dr. Willson. Not many graduate students are fortunate enough to have a supervisor that genuinely cares about their students as much Dr. Willson and I will be forever grateful for his support. I would also like to thank Debbie Willson for always treating me so kindly and welcoming me as a part of the Willson group and offering her support and great conversation.

I would not be where I am today without my best friend and partner, Yuri Chornobil. My life has been forever changed because of him. No one else has ever given me the support, motivation, and love that he has and I will be forever grateful for that. His ambitious attitude has inspired me and helped me reach this point and I look forward to all that the future has in store for us and our family in the future. We are both indebted to the city of Austin. It is the place where we fell in love, started a family (of dogs), lived and shared so many memories together. Austin is unlike any other place and it is so special to me because it represents where my life seems to have really begun. So, for Yuri and me, it will always be our city and we will always be Texans no matter where we go.

I would not be the scientist and chemist I am today had it not been for my undergraduate advisor, Dr. Daniela Tapu. I will be forever grateful that I had the opportunity to learn from her. I also would like to thank Dr. Christopher Bielawski for having me in his group for my first 2 years of graduate school and allowing me to have the freedom to work on carbene chemistry that everyone thought would never work!

Apart from my mentors, there are so many other talented researchers that I have worked with that deserve recognition. Thank you to all the former Bielawski group members, specifically Dominika Lastovickova and Jon Moerdyk. Thank you to all the

former Willson group members, specifically Austin Lane, Gregory Blachut, and Sunshine Zhou. I would also like thank Natsuko Ito, not only did she patiently teach me so much about block-copolymers she also is a great friend and I value all the time we got to spend together while in Austin. Thank you to Steve Sirard and LAM Research for their help and support.

Lastly, I would be nowhere without my mother who has also been my biggest supporter and friend. I know she would be proud of me no matter what I choose to do in life, but I know that this accomplishment has made her extremely proud! Finally, thank you to my dog, Reese for being the best companion I could have ever asked for. Reese has been with me through cramming 4 years of undergrad into 3 years, moving to Texas, getting through my first big graduate school exams, becoming obsessed with my research, taking my qualifying exams, and everything since then. She has endured my journey as much as I have and I cannot imagine life without her unconditional love and unique personality!

From small molecules to macromolecules: design, synthesis, and evaluation of functional organic materials.

Zachary Ryan McCarty, Ph.D.

The University of Texas at Austin, 2018

Supervisor: C. Grant Willson

The incorporation of electronic device technology into our everyday lives has become an unavoidable reality in today's connected world. Getting to this point has taken countless ingenious measures by scientists and engineers dedicated to increasing the speed and efficiency of the microelectronic devices that power many of the tools we rely on every day. For more than 50 years, the microelectronics industry has successfully manufactured generations of devices by shrinking the transistors on their chips. This shrinkage was made possible by improvements in photolithography. However, the physical limits to the resolution of lithography has now been reached leading leaving the microelectronic industry to employ costly and inefficient double patterning processes, which are expensive and unsustainable to extend the resolution of photolithography in high-volume manufacturing. Many question whether the ever cheaper and faster demand can continue.

This dilemma has inspired the exploration at alternative patterning processes, one of which is the directed self-assembly (DSA) of block-copolymers (BCPs). Through careful and judicious design, the self-assembly of BCPs allows access to sub-5 nm features which are inaccessible by all current photolithographic technologies. While there has been extensive work done on the DSA of BCPs to produce aligned, lamellae in thin films, there is still a need for improvement in this field.

Forming BCP films with a thickness on the order of their domain size and transferring the patterns formed by self-assembled BCPs into useful substances by reactive ion etching (RIE) is one area that requires more thorough investigation. Several strategies have been devised to impart some degree of etch-selectivity to one of the domains of a BCPs. One such strategy, which will be the focus of the work presented in this dissertation is the selective formation of a metal-oxide etch mask in one of the polymer domains of a BCPs. The development of a suitable BCP candidate will be presented as well as the results of several studies on vapor-phase infiltration processes. The challenges and discoveries made will be presented throughout this work.

Table of Contents

List of Tables

List of Figures

Chapter 1: Introduction to lithography in the microelectronics industry

1.1 HISTORICAL BACKGROUND

Microelectronics is a field that has brought together people from all backgrounds, parts of the world, and areas of specialty. This collaborative and multidisciplinary approach was utilized starting with the earliest computer, which required entire laboratories to bring together mathematicians, engineers, and other scientists in order to achieve something that has since changed our entire way of life. Smart phones which are now ubiquitous in our society are amazingly powerful pocket-sized computers; their construction has only been possible through collaborations and the work of countless scientists, coders, designers, and engineers throughout the world. It is through the constant improvements made in microelectronics and the perfection of the integrated circuits (IC) that we now have access to a seemingly unlimited supply of information and can be connected to all parts of the world all the time; a truly remarkable consequence of innovation.

First revealed to the public in 1946, the Electronic Numerical Integrator and Computer (ENIAC) was the earliest known computer.[1] A behemoth machine, the ENIAC had its own dedicated power lines and 18,000 vacuum tubes requiring constant replacement. A replacement for the inefficient and labor-intensive use of vacuum tubes came following the realization of the transistor. The transistor was first developed in 1947 by John Bardeen and Walter Brattain at Bell Labs, a product of their work on germanium crystals.[2,3] The transistor, which acts a switch in an electrical circuit, was celebrated by the early electronics community because it enabled electronic circuits to be constructed that were more complex, required less power, and were far more reliable than those constructed using vacuum tubes.

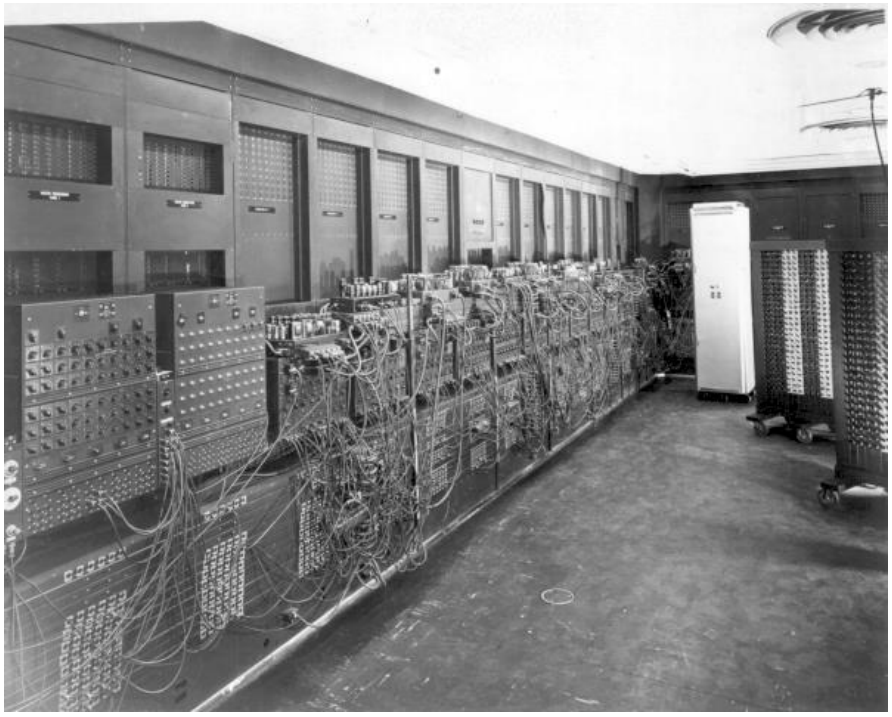

Figure 1.1: Photo showing part of the assembling ENIAC. "U.S. Army Photo" http://ftp.arl.army.mil/~mike/comphist/

As time went on, the circuits that were built from hand-soldered transistors, diodes, rectifiers, and capacitors reached a limitation. In order to make the circuits faster and more reliable, more and more of the cumbersome circuit elements needed to be wired together making the devices unmanageable in size, time consuming to construct, and costly. This dilemma was solved independently in 1958 and 1959 by Jack Kilby at Texas Instruments and Robert Noyce at Fairchild Camera with their demonstration of the first integrated circuits, **Figure 1.2**.[2,4] The transformative power of the IC is the ability to *integrate* or pattern any number of electrical components onto a single piece of semiconductor simultaneously, without the need to individually install each component, a discovery that truly had transformed our world.

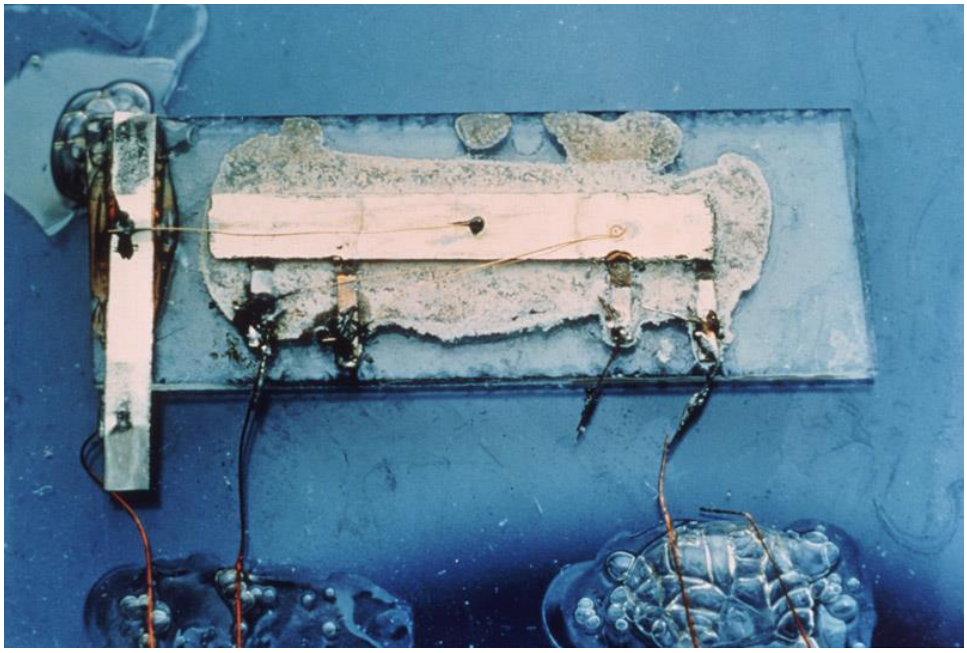

Figure 1.2: Jack Kilby's original integrated circuit. Courtesy of Texas Instruments.

What followed was indeed the beginning of a period of technological innovation that has been characterized by a constant stream of new technology, most of which is powered by ever faster and more capable IC's. Indeed, this was first articulated by Gordon Moore in 1965 in his famous "Moore's Law" which states that the number of transistors on a chip would double every year.[5] While not an actual law at all, Moore's law has been a self-fulfilling prophecy that has set the pace for the remarkable innovations produced by the microelectronics industry over the past 50 years.

1.2 PHOTOLITHOGRAPHY

The method of choice used to manufacture ICs is photolithography.[6] In its most basic form, the process of photolithography involves using light, which is passed through a mask containing an image to "print" onto a substrate to create a 3-dimensional relief image of the structures of an IC. Specifically, a light-sensitive polymer called a photoresist

is coated onto a substrate (commonly a silicon wafer), light of a specific wavelength is then passed through a photomask which contains a pattern of an IC component.[7] Depending on the photochemical reaction that a given resist undergoes, the areas exposed either become soluble (for positive tone resists) or insoluble (for negative tone resists) in a specific solvent called a developer, which is applied to the films after the exposure step, constituting the development step. Thus, after development the resultant relief image can be transferred into the underlying substrate by etching. A generalized optical lithography scheme is shown in **Figure 1.3**.

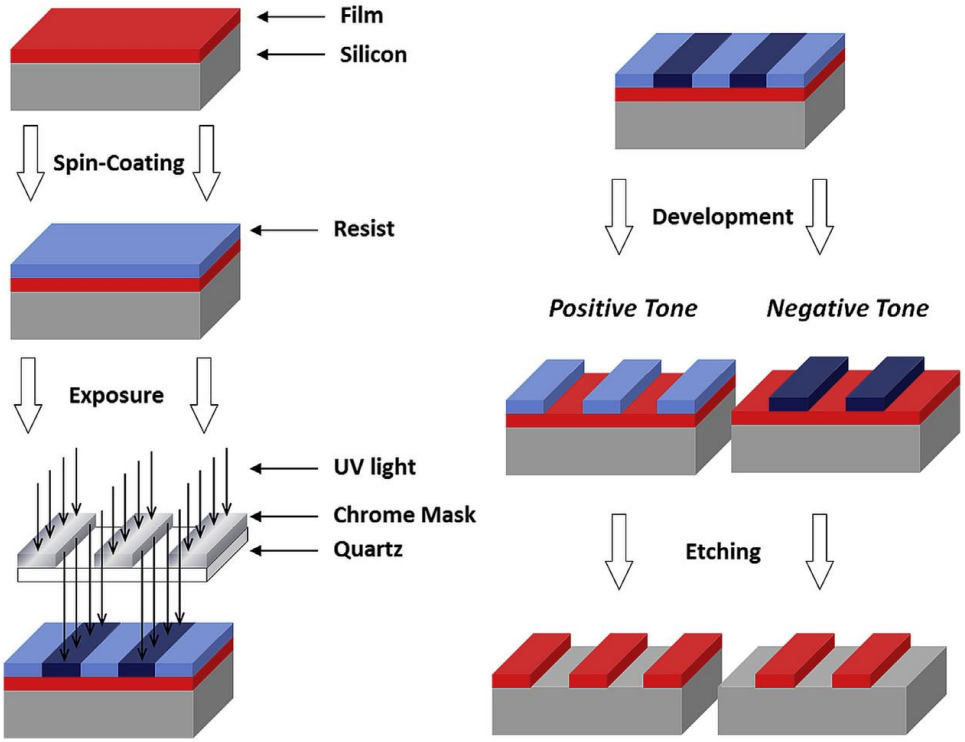

Figure 1.3: General scheme for a photolithography process showing the difference between positive and negative tone resists. Reproduced with permission.[8] Copyright 2016 Elsevier.

The fundamental factor that has enabled optical lithography to maintain its utility for IC production for so long is referred to as the "critical dimension" or minimum resolution. The resolution of a photolithographic process is the smallest sized transistors elements that can be produced. The resolution, R can be described by Rayleigh's criterion:

$$R = k_1 \frac{\lambda}{NA} \qquad \text{(Eq. 1.1)}$$

where λ is the wavelength of the exposure light, NA is the numerical aperture of the lens, and k_1 is a process dependent factor. Together, these factors form the basis for years of efforts to continually print smaller features, until reaching the physical limitations of optical lithography.

As it can be seen in Equation 1.1 one way to increase the resolution is by decreasing the wavelength of light used. This idea was heavily investigated and is responsible for the progressive utilization of ever shorter wavelengths of light (436 nm), to UV (365 nm), to deep-UV (248 nm), and to finally 193 nm.[7] Although there was a large effort made to move towards using light with a wavelength of 157 nm, issues with optics prohibited any further progress to be made and those pursuits were eventually abandoned. In the progression of steps taken to improve the resolution achieved during a lithographic process, reducing the k_1 factor can be achieved by optimizing the resist processing and design, a pursuit which has resulted in an impressive library of photoresists available.[9] The remaining parameter is the numerical aperture, NA of the lens. Referring to Equation 1.1, the resolution, R can be increased when the NA parameter is increased. Like the exposure wavelength, this parameter has experienced phenomenal improvements in a very short period of time.[7] The earliest projection tools had a NA of only 0.28, compared with the technology largely used

today which operates with a NA greater than 1. Indeed, the tools today are operating at their physical limitations. A NA larger than 1 has only been achieved by a clever technique referred to as immersion lithography.

Conceived in an effort to extend the utility of 193 nm lithography, immersion lithography was vital in keeping with up "Moore's law" when it was first introduced in 2006. The fundamental difference behind immersion lithography is the introduction of a fluid, with a refractive index larger than that of air, in between the lens and the wafer/sample.[7] While a substantial amount of work was done to identify a fluid with a higher refractive index than water to be used in immersion lithography, water remains to be used for immersion lithography in most manufacturing settings today.[10] With immersion lithography, the resolution limit for a single optical patterning processing was reached at 45 nm half-pitch.[11]

1.3 Beyond Optical Lithography

While single step photolithographic processes including 193 nm immersion was able to sustain the IC industry's pace of innovation, once those limitations had been reached a variety of patterning techniques became intensely investigated. One of the earliest techniques to be used to reach the 32 nm and 22 nm half-pitch nodes was multiple patterning.[12] In the most general description, multiple patterning processes provide access to producing single layer patterns with smaller features by increasing process complexity, usually by repeating steps of a process. Several patterning schemes were developed as multiple patterning techniques including the more successful litho-etch-litho-etch (LELE),[13] litho-freeze-litho-etch (LFLE),[14] and self-aligned doubled patterning (SADP).[15] Through the use of repeated photolithography and etch steps, multiple patterning techniques are able to surpass the 45 nm half pitch limitations of traditional single exposure

lithography, albeit at a much higher cost and increase in process complexity leading ultimately to lower device yields.

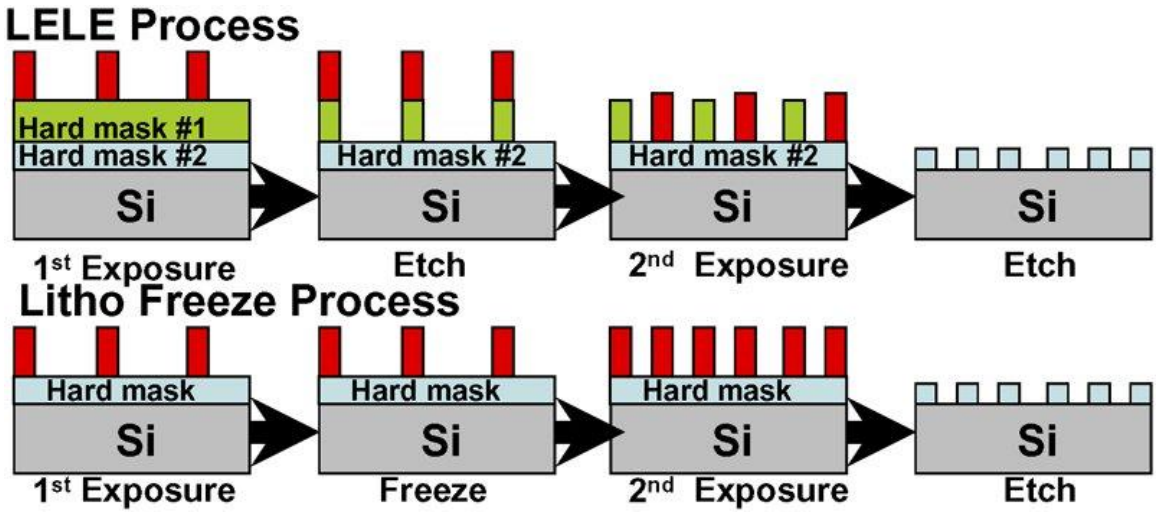

Figure 1.4: Graphical representation of the process for two multiple patterning processes. Shown is the litho-etch-litho-etch (LELE) process and the litho-freeze-litho-etch (LFLE) process. Reprinted with permission from Zimmerman, P. *SPIE Newsroom*, "Double patterning lithography: double the trouble or double the fun?" **2009**[16]

Although multiple patterning techniques have been able to keep up with semiconductor technology roadmaps, their increasing costs have inspired the global semiconductor industry to heavily invest in replacing 193 nm lithography with extreme ultraviolet (EUV) lithography. EUV radiation that is most relevant for lithography is in the range of 11-14 nm. While there has been significant progress in developing and implementing EUV technology, it has been a laborious and lingering process which has proven to be incredibly expensive mainly due to the complexity of the light source and power required; as well as issues with photomasks and mirrors.[17] Despite these drawbacks, as of early 2018 manufacturers including Globalfoundries, Taiwan Semiconductor

Manufacturing Co., Samsung, and Intel all have acquired EUV tools and have committed to begin using EUV in their manufacturing processes by years end.[18]

1.4 ALTERNATIVE PATTERNING TECHNOLOGIES

Other lithographic technologies exist that do not rely on photons for patterning and have taken on niche roles in device fabrication that have evolved over time. These include E-beam lithography, nanoimprint lithography (NIL), and chemical patterning by self-assembly, to name a few.[19] E-beam lithography uses a focused beam of electrons to pattern a resist film and does not require using a mask, for this reason it is commonly used to produce the masks used in other lithography processes. E-beam lithography has superior resolution to other optical lithographic techniques but its use in high-volume manufacturing is limited due to the significant amount of time required to produce patterns using this technology. Nanoimprint lithography (NIL) is a contact lithography technique that is a non-radiation based method for patterning which patterns with high resolution.[19] In a nanoimprint process a template creates a pattern on a resist covered substrate through physical deformation; the pattern can then be transferred into the substrate. One obvious advantage of NIL is that the resolution is entirely determined by the template pattern. However, concerns and issues with particle contamination and template lifetime has prevented a widespread adoption by manufacturers.[8] However, Toshiba and SK Hynix recently announced plans to implement NIL technology in their high volume manufacturing processes. Finally, a chemical patterning technique, namely directed self-assembly is a technology that uses materials which form the desired patterns spontaneously. Self-assembly relies on exploiting the thermodynamic behavior of certain materials, mainly block-copolymers, to form patterns that can be guided or unguided. Much

of the work discussed in this dissertation will be focused on self-assembly and a more thorough discussion of the theory and its implementation will be reserved for Chapter 2.

Chapter 2: Self-assembly of block-copolymers and applications in nanotechnology

2.1 Introduction to block-copolymer self-assembly

BCPs are an interesting class of compounds that are particularly attractive as candidates for next-generation nanotechnologies due to their ability to phase-separate into periodic nanostructures. The time is "right" for BCPs since they readily form structures with dimensions in the range of 5 to 50 nm, which is inaccessible by traditional optical lithography. While there is a battery of different structural arrangements that can be classified as a BCP, the discussion for the purposes of this dissertation will focus on linear, A-B type diblock-copolymers of the sort shown in **Figure 2.1.** BCPs can be intuitively treated as two chemically distinct polymers that are joined together through a covalent linkage.

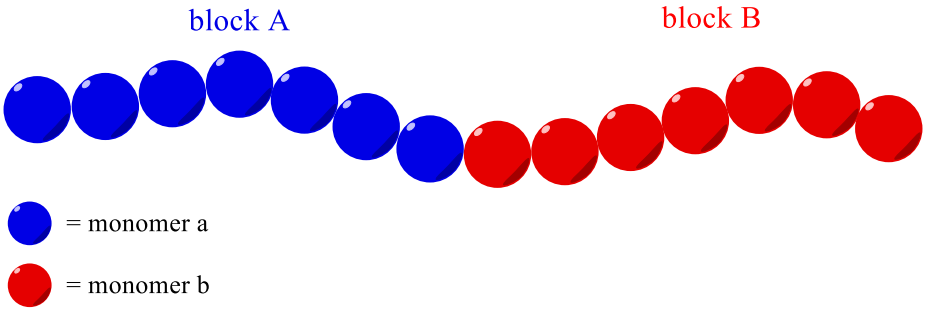

Figure 2.1: Graphical representation of a general A-B type block-copolymer

Being covalently linked, the affinity for block A and block B to macrophase separate is precluded. Thus, when polymers of the type shown in **Figure 2.1** consisting of two chemically incompatible blocks demix the polymer chains, phase separation leads to the formation of periodic microstructures or microdomains.[20] The phase behavior and the morphology of a BCP is determined by several parameters; volume fraction of each block

(*f*), degree of polymerization (N), and the interaction parameter (χ) or the segregation strength.[21–23] A theoretical phase diagram for a simple A-B diblock copolymer is shown in **Figure 2.2**. The phase diagram is useful for guiding the synthesis of a block copolymer to obtain a particular morphology. More specifically, a morphology can be targeted by altering the volume fraction, *f* and the product χN. The product of χN is used the quantify the segregation strength between two blocks of BCPs and must be equal to at least 10.5 to produced ordered microstructures, based on theoretical work.[24] Lamellar morphology has been identified as the most lithographically relevant morphology and will therefore be the focus of the following discussions.

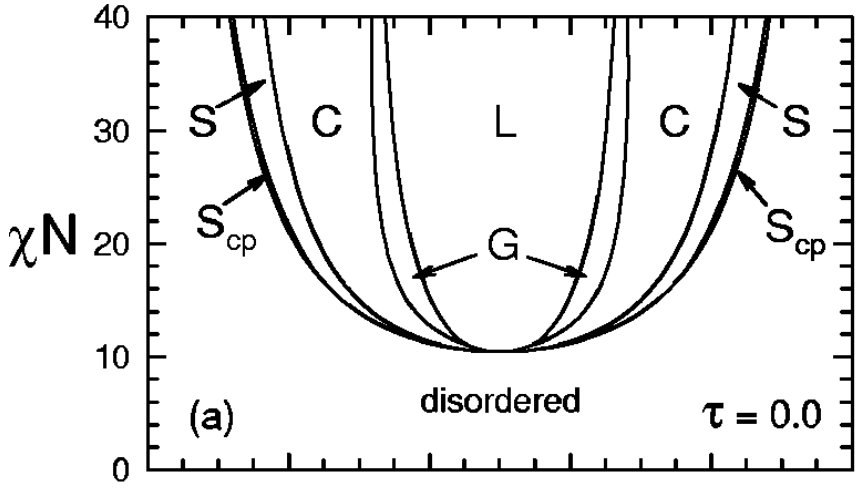

Figure 2.2: Theoretical phase diagram for diblock copolymer. X-axis represents volume fraction of block A (f_A). Morphologies represented on diagram include: spherical (S), lamellar (L), gyroid (G), cylindrical (C), and closed-packed spherical (S_{cp}). Reproduced with permission.[25] Copyright 2000 American Institute of Physics.

In addition to the morphology exhibited by a BCP, consideration must be given to the size of the microdomains expressed upon phase separation. The full pitch of a BCP,

also known as the natural periodicity (L_0) describes the size of the lamellae microdomains. For a symmetric diblock copolymer the L_0 can be described numerically by **Eq. 2.1**.

$$L_0 \sim N^{2/3}\chi^{1/6} \qquad \text{Eq. 2.1}$$

Therefore, as both N and χ increase, the pitch also increases but the function is more strongly dependent on N (degree of polymerization), which is also proportional to the molecular weight). This relationship is conceptually rationalized by considering that as a BCP increases in size or polymer chains are made longer, the domain spacing grows. Taking this into account, the requirement that $\chi N \geq 10.5$ gives the smallest feature sizes a BCP will form. This has been corroborated by experiment.[26] Once the compositional aspects of a BCP have been established, in order to exploit their utility in lithographic application the orientation in thin films must be considered. This topic is covered in Section 2.2.

2.2 BCP BEHAVIOR IN THIN FILMS

In practice, the self-assembly of BCPs is carried out on thin films. Ideally, the BCP should be soluble in a variety of casting solvents from which solutions can be deposited onto a substrate; typically, by spin coating. The choice of casting solvent and spin-coating conditions effects on the quality of the films produced is largely empirical and unique to each BCP. In order to produce ordered films, the polymer films are heated subsequent to spin-casting. Annealing provides the mobility necessary to produce ordered films of the BCP. Two methods are typically used for annealing: solvent annealing and thermal annealing. In thermal annealing, BCP thin films are heated to a temperature above the BCP's glass transition temperatures (T_g) of both blocks of the BCP (but below the

decomposition temperature) for a given period of time. Thermal annealing can be executed under vacuum, in an inert gas atmosphere, or under atmospheric conditions.[23] In solvent annealing, thin films are exposed to an atmosphere of solvent vapor(s) which are chosen based on their interactions with each BCP domain. The absorption of the vapor lowers the T_g of the blocks and provides the mobility necessary for the BCP domains to reorganize into their equilibrium state. However, due to the large variability in solvent combinations and process reproducibility concerns, thermal annealing is the preferred method for achieving self-assembly in a high-volume manufacturing environment.

Following the anneal step, one of the BCP block domains can be selectively removed by etching, resulting in a relief image that provides patterned areas to the substrate. The resulting pattern can then be transferred into the underlying substrate by a subsequent etching step. The idealized process described in this section for DSA is shown graphically in **Figure 2.3**.

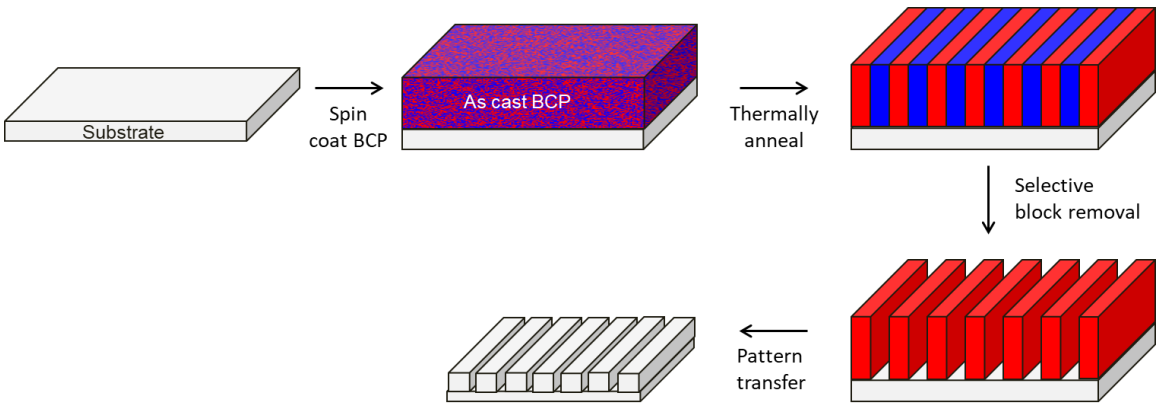

Figure 2.3: Graphical representation of the DSA of a BCP. Note, this is an idealized representation and is meant to only represent the general process steps.

2.3 SURFACE CONSIDERATIONS FOR SELF-ASSEMBLY

In practice, self-assembly of BCPs to form lithographically relevant patterns is more complicated than what was described in Section 2.2. This complication is a result of the tendency of BCPs to form "wetting" layers on a substrate that preferentially interacts with one of the BCP domains. Specifically, because the chemically distinct domains of a BCP typically have different surface energies, upon orientation on a substrate (e.g., silicon wafer, SiO_2) one block will migrate to or wet the substrate preferentially and the other will wet the top interface; a phenomenon which minimizes surface energies at the interfaces.[27–29] Consequentially, for lamellae forming BCPs, annealing films on a preferential substrate induces orientation parallel to the substrate, while perpendicular orientation is desirable for most applications. However, the perpendicular orientation of BCPs can be induced by employing a substrate and interface which "wets" or interacts with both blocks equally (i.e., a neutral surface).

The preferential interaction of a BCP and a particular surface results in the formation of distinct surface topography that can be used as a diagnostic tool for identifying neutral surfaces. The surface topography formed is commonly referred to as islands and holes and their formation is highly dependent upon the film thickness (L_{avg}) and the BCP pitch (L_0).[30] When the same block wets the substrate and interface (symmetric wetting); islands form when $nL_0 < L_{avg} < (n + 0.5)L_0$ and holes form when $(n – 0.5)L_0 < L_{avg} < nL_0$. Under asymmetric wetting conditions; islands are formed when $(n – 0.5)L_0 < L_{avg} < nL_0$ and holes formed when $nL_0 < L_{avg} < (n + 0.5)L_0$. Formation of islands and holes occurs only for incommensurate film thicknesses. This phenomenon is not observed under commensurate conditions; when $nL_0 \approx L_{avg}$ for symmetric wetting or when $(n – 0.5)L_0 \approx$

L_{avg} for asymmetric wetting.[31,32] A graphical depiction of island and hole topography is shown in **Figure 2.4**.

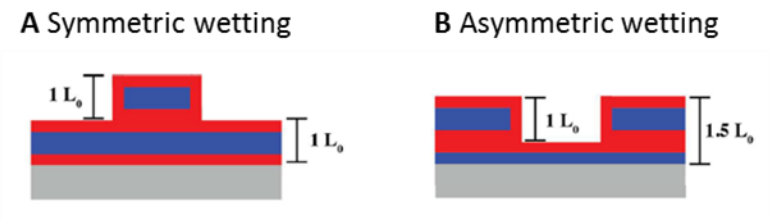

Figure 2.4: Graphical representation of the formation of islands (A) or holes (B) under different wetting conditions. Adapted with permission from Maher, M. J.; Bates, C. M.; Blachut, G.; Sirard, S.; Self, J. L.; Carlson, M. C.; Dean, L. M.; Cushen, J. D.; Durand, W. J.; Hayes, C. O.; Ellison, C. J.; Willson, C. G. *Chem. Mater.* **2014**, *26*, 1471-1479. Copyright 2014 American Chemical Society.

Therefore, it is advantageous to evaluate the wetting behavior of a BCP using a free surface (air) at a film thickness incommensurate to both symmetric and asymmetric wetting (e.g., 1.2 L_0). The formation of island or hole structures is observable by optical microscopy and can be quantified with atomic force microscopy (AFM), whereby features heights can be measured to be multiples of a BCP's L_0. The evolution of island/hole features over differing film thicknesses using both optical microscopy and AFM is illustrated in **Figure 2.5** for poly(styrene-*block*-methyl methacrylate), PS-*b*-PMMA films of differing molecular weight.[33]

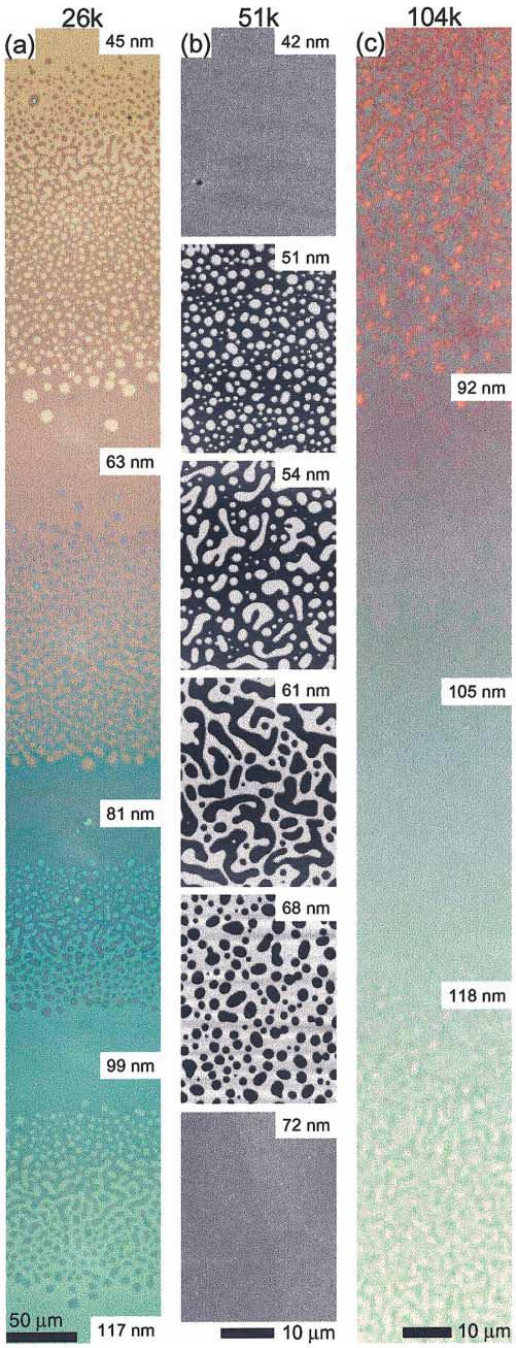

Figure 2.5: Representation of the formation of either islands or holes as a function of different film thicknesses. Representative films are of PS-b-PMMA annealed at 170 °C. (a) $M_n = 26$ kDa, $L_0 \approx 17$-18 nm; (b) $M_n = 51$ kDa, $L_0 \approx 27$-30 nm; (c) $M_n = 104$ kDa, $L_0 \approx 42$ nm. Copyright 2001 by The American Physical Society.[33]

Employment of the "island-hole test" in a system in which one block is known to be preferential to one of the interfaces (such as the free-surface/air), allows determination of the wetting preference of the other. This is a particularly useful tool for finding a surface which is overall neutral for a BCP. Furthermore, the island-hole test provides a powerful method for identifying a neutral surface. If a BCP is annealed between a preferential interface and a non-preferential (neutral) interface, the topography generated is $0.5L_0$ thick islands and holes.[34,35] Knowledge of the formation of half-features provides a convenient and reliable method to achieve perpendicular orientation in BCP thin films, as the $0.5L_0$ structures are easily identified from the classical $1L_0$ structures when measured by AFM. Lastly, the topography with step heights of $0.5L_0$ is found to always invert around a film thickness of $(n \pm 0.5)L_0$ but the half features persist at all film thickness under neutral conditions.

2.4 Interface Design and modification strategies

With an understanding of the various interactions of BCP films with their top and bottom interfaces, under confinement conditions many strategies have been devised for modifying the surface energies to achieve non-preferential interfaces, which is a prerequisite to inducing the formation of perpendicular lamellae. The substrate and interface (top surface) must be dealt with separately, however both share some practical requirements. Mainly, the deposition of one layer either on a substrate or on top of an already deposited BCP layer (in the case of spin-coating a top-surface treatment on a pre-cast BCP film) must not affect the solubility such that another film is altered in any way.

To begin, a surface can be made neutral by a variety of methods all involving the introduction of some chemical component that balances the surface energy to match a given BCP. These methods include using self-assembled monolayers,[36,37] or films of statistically

random copolymers, which are often comprised of the same monomers as that of the BCP to be orientated (which is not a requirement).[38–41] Furthermore, there is a practical requirement that any surface/substrate treatment must be rendered insoluble after deposition in order for BCP-solutions to be spin-coated on top without disrupting the films. Several groups have employed a cross-linkable or grafting moiety installed into the backbone of the copolymers. The advantage of cross-linkable substrates is clear; the resultant thin-films can be rendered insoluble in most common BCP spin-coating solvents.

Although the compositions of the surface treatments have changed throughout their evolution, the Willson group has had a great deal of success utilizing a "family" of cross-linkable surface treatments (XSTs), which are based on poly(4-*tert*-butylstyrene) and poly(methyl methacrylate) (PMMA) copolymers, along with a small percentage of 4-azidostyrene, which is active in cross-linking the films.[34] The copolymers of the aforementioned XSTs have inherently dissimilar surface energies which can be exploited by varying the ratio of each monomer.[42] Thus, a library of XSTs as exemplified in **Figure 2.6** efficiently enables one to screen for surface neutrality over a range of surface energies; using the island/hole analysis of BCP thin films annealed with a free surface.

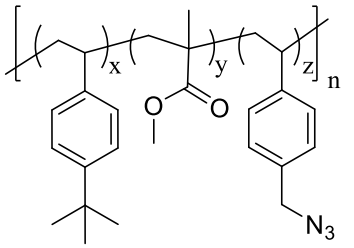

Figure 2.6: General structure of the cross-linkable surface treatments pioneered by the Willson group.

The interaction of block-copolymer domains with the top interface has proven to be a greater challenge to overcome in comparison with the substrate or bottom surface, due to the practical limitations imposed by applying a "top-coat" over an as-cast film of BCP. While the XSTs just described can be cast from common organic solvents because most organic BCPs are soluble in these solvents, the films constituting a top interface must be cast from orthogonal solvents (e.g.; water, methanol). However, a basic understanding of solubility principles of organic compounds would suggest that any compounds soluble in such orthogonal solvents would be inherently very hydrophilic and therefore, films of these would likely favor a preferential interaction with the more polar or hydrophilic domain in a BCP rather than interacting non-preferentially with both blocks.

Indeed, this dilemma has been circumvented with top coat materials pioneered by the Willson group.[43] Utilizing the thermal ring-opening chemistry of maleic anhydride, the top coats can be formulated from the ring-opened form as the trimethylammonium salts which can be spin-coated directly onto BCP films from alcohols or water. Upon subsequent heating of the reactive film stacks the liberation of a volatile amine (e.g., ammonia) quickly produces the ring-closed versions of the top coats, which are less polar and able to serve as a non-preferential interface for a BCP. The top coats can then be removed or stripped from the film stacks by washing with aqueous base, leaving the perpendicularly orientated BCPs. The general structure of the top coats used by the Willson group is shown in **Figure 2.7.** The general methodology established from the top coats of the type shown in **Figure 2.7** can be adapted to a variety of different monomers based on the components of a BCP targeted for DSA.

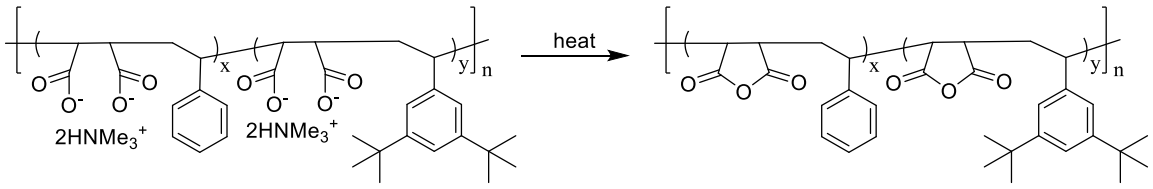

Figure 2.7: Ring-closing reaction example for the general type of top coats pioneered by the Willson group. Note: the ring-closed form is responsible for generating "neutral" surface conditions.

2.5 CONFINEMENT AND ORIENTATION CONTROL

Using the strategies described in the previous sections, perpendicular orientation of lamellae-forming di-block copolymers can be achieved conveniently using the island/hole analysis to identify both a top and bottom non-preferential interface. Confining a BCP between the neutral bottom and top interfaces, thermally annealing the film stack, stripping top coat, and the selective etching of one of the BCP domains provides a path to high resolution patterns that provide access to the substrate. However, these patterns lack long-range ordering and are typically referred to as "fingerprint" patterns, an example of which is shown in **Figure 2.8**.[44]

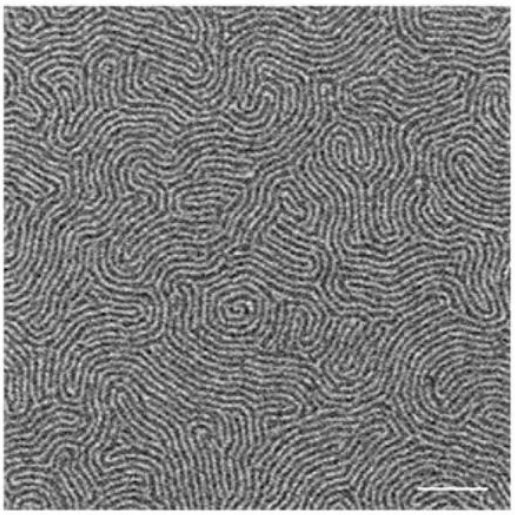

Figure 2.8: Top down SEM image of a fingerprint pattern formed by a 5 nm BCP (L_0 = 5 nm). Adapted with permission from Lane, A. P.; Yang, X.; Maher, M. J.; Blachut, G.; Asano, Y.; Someya, Y.; Mallavarapu, A.; Sirard, S. M.; Ellison, C. J.; Willson, C. G. *ACS Nano*, **2017**, *11*, 7656-7665.

In order to establish long-range ordering of BCP domains to form patterns for device applications, typically a pre-patterned substrate surface is necessary. These pre-patterned substrates or templates typically consist of lithographically pre-defined patterns that guide the alignment in a process referred to a directed self-assembly (DSA). Two methods are preferred for aligning BCPs, both methods involve pre-patterning a substrate with sparsely defined guide lines. DSA based on chemo-epitaxy relies on chemical guide lines that are required to have dimensions commensurate the BCP periodicity, L_0 which can be increasingly difficult to achieve as the minimum feature sizes formed by BCPs contain to scale to smaller and smaller dimensions. Grapho-epitaxy uses topographic features to guide the BCP domains and have a nonplanar presence on wafers which increases thickness and potentially complicates the alignment of some BCPs. However,

grapho-epitaxy does not require the very small guidelines as chemo-epitaxy making it a arguably more popular method.[45–48]

2.6 Pattern transfer and etch contrast of BCPs

The final processing of self-assembled BCPs is etching. Following orientation, alignment, and the selective removal of one of the BCP domains, the result is an etch mask formed by the more etch-resistant block. Thus, among the other parameters that need to be considered when designing a BCP to be applied to lithography such as the interaction parameter, χ the etch contrast of the BCP domains is crucial for successful pattern transfer into an appropriate substrate.[49] Previous work using BCPs has demonstrated successful pattern transfer processes which rely on reactive-ion etch (RIE) or plasma etching for image transfer of a polymer etch mask.[50] Consequently, in most BCPs containing only C, H, and O atoms there is insufficient etch contrast between the BCP domains and the structures that are pattern transferred lack the precision and structural integrity necessary for device fabrication. For this reason, it is widely accepted that for BCP lithography to be considered for high-volume manufacturing improvement of etch contrast between the BCP domains is vital.

In summary, the ability to transfer the patterns created by self-assembled BCPs into the underlying substrate is a vital process step for demonstrating the utility of BCP lithography for device fabrication. However, there are several challenges that need to be addressed in order to pattern transfer structures with high-aspect ratios, namely increasing the etch contrast between the different block-copolymer domains. Maintaining the fidelity of an etching process as the feature sizes (and therefore the film thickness) decrease then becomes ever more challenging. One strategy for overcoming these obstacles will be presented in this dissertation.

Chapter 3: Enriching organic polymers towards enhanced contrast in block copolymer etch masks

3.1 PROJECT MOTIVATION AND BACKGROUND

As briefly mentioned in Section 2.6, etch contrast between BCP domains poses a potentially significant obstacle. Incorporating an inorganic moiety or atom selectively into one of the BCP blocks has been identified as one successful strategy for increasing the etch contrast between the blocks.[51] Two methods exist for incorporating an inorganic group or atom, selectively into the polymer chains of one BCP domain: vapor-phase infiltration of assembled BCP nanostructures and use of metal-containing monomers during the synthesis of one of the BCP blocks.[51,52]

The importance of metal containing monomer has the been the central focus of an effort by the Willson group directed towards the miniaturization of patterned device structures. This effort has focused on the use of silicon-containing BCPs, a few examples of which are shown in **Figure 3.1**. Incorporating silicon into the backbone of one of the BCP blocks was chosen because it has been shown that in addition to increasing the value of χ, an etch-resistant SiO_2 layer is formed when these materials are exposed to oxidizing reactive ion etching (RIE) conditions.[53,54] These Si-BCPs were used to produce both fingerprint and self-assembled lamellae patterns with half-pitch dimensions from 20 nm to 14 nm, and more recently features as small as 5 nm.[44,55]

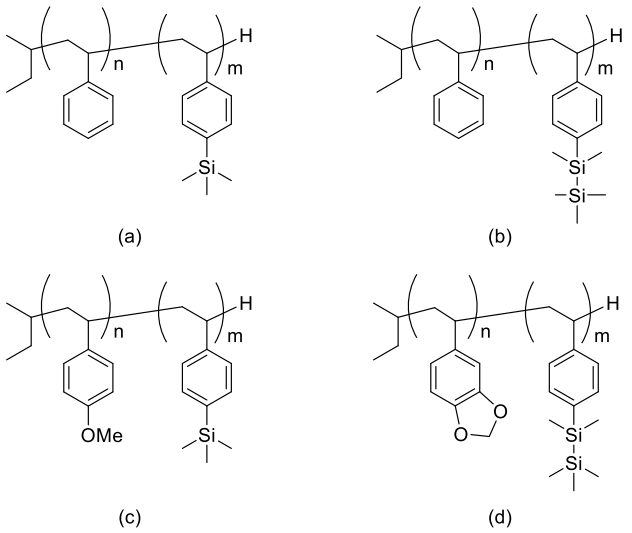

Figure 3.1: Select examples showing the structures of silicon-containing block-copolymers from the Willson group. (a) poly(styrene)-*b*-poly(4-trimethylsilylstyrene), PS-*b*-PTMSS; (b) poly(styrene)-*b*-poly(4-pentamethyldisilylstyrene), PS-*b*-PDSS; (c) poly(4-methoxystyrene)-*b*-poly(4-trimethylsilylstyrene), PMOST-*b*-PTMSS; (d) poly(4-methoxystyrene)-*b*-poly(4-pentamethyldisilylstyrene), PMOST-*b*-PDSS.

However, early studies evaluating the etch properties of the perpendicular patterns formed by polymers a-c (**Fig. 3.1**) indicated that while silicon incorporation into polymers does indeed retard the initial etch rate, there is a concomitant loss in film thickness which is a penalty incurred for the formation of the silicon-oxide etch mask from the Si containing polymers. While this phenomenon did not inhibit pattern transfer in the silicon-containing BCPs with L_0 > 10 nm, in films with features in the sub-10 nm range, the loss of a few nanometers of mask-material was viewed as a significant issue that needed to be addressed in order to also generate high aspect ratio features. The representative etch rate data measured for the relevant homopolymers is shown in **Figure 3.2**. The data displayed in **Figure 3.2** provide confirmation that designing BCPs that contain a pre-installed inorganic moiety impart a greater resistance to RIE conditions in comparison to purely organic BCPs.

In the two Si-BCPs, the initial 10-14 s of the etch process is characterized with a rapid loss in ca. 4-7 nm of film thickness which can be interpreted as formation of the silicon-oxide etch mask; this is followed by a very low "steady-state" rate period for the duration of the measurement, presumably due to the resistivity provided by the silicon oxide formed.[55] Therefore, although this loss may be tolerated in films of sufficient thickness, it was anticipated to be a problem in films that are made on the order of 10 nm thick.

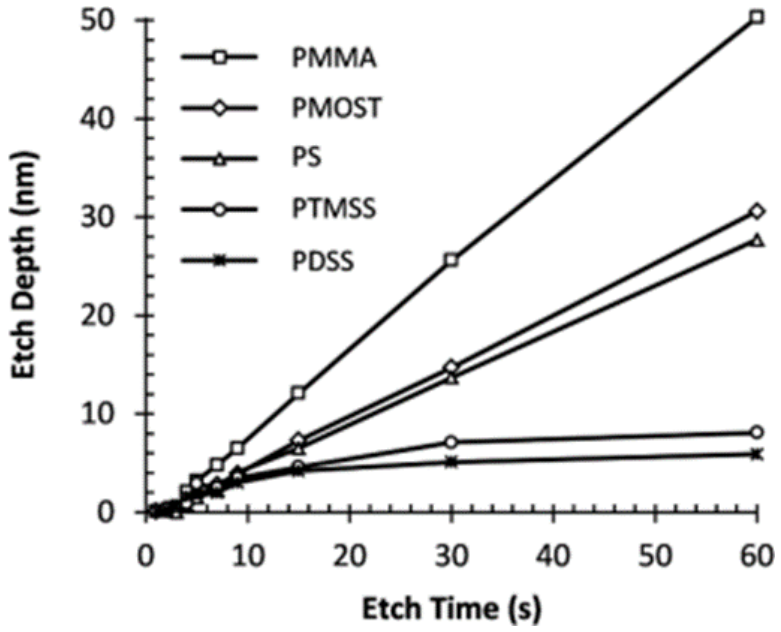

Figure 3.2: Etch rate data for organic homopolymers (PMMA, PMOST, PS) and silicon containing homopolymers (PTMSS, PDSS). Reproduced with permission from Durand, W. J.; Blachut, G.; Maher, M. J.; Sirard, S.; Tein, S.; Carlson, M. C.; Asano, Y.; Zhou, S. X.; Lane, A. P.; Bates, C. M.; Ellison, C. J.; Willson, C. G. *J. Polym. Sci. A Polym. Chem.* **2014**, *53*, 344-352. Copyright 2014 Wiley Periodicals, Inc.

Inspired by the prospects of producing BCPs capable of forming sub-10 nm patterns and being able to demonstrate the ability to transfer the structures into a substrate with high

fidelity, we were interested in exploring another method to increase the etch resistance of BCPs, namely using a vapor-phase infiltration process. During the first part of an etch process on a Si-BCP, the loss of thickness is due to the formation of the silicon oxide etch mask. We postulated that by forming a metal oxide before the etch step, this loss of material would be avoided thereby preserving the structural integrity of the etch mask, improving the quality of the transferred patterns, and gaining more control of the final aspect ratio. Finally, we envisioned being able to execute a "zero-volume" change process whereby the dimensions of the patterned features were not changed by forming the metal oxide. Several methods exist for selectively incorporating an inorganic moiety into one of the domains of a BCPs in thin-films, an overview of those processes and their limitations is described in Section 3.2.

3.2 VAPOR-PHASE INFILTRATION: GENERAL DESCRIPTION AND LIMITATIONS

Vapor-phase infiltration (VPI) is a term used to describe a number of different processes that are used to modify polymer films. In general, VPI techniques allow organic polymer films and surfaces to be selectively transformed to organic-inorganic hybrid materials by exploiting preferential interactions between a gaseous reactant (also referred to as "precursor") and chemically reactive groups on polymers.[52] One of the earliest example of using VPI on polymeric materials utilized atomic layer deposition (ALD) to deposit Al_2O_3 on the surface of polyethylene particles, leading to the discovery that polymers were permeable to precursor gases.[56] It has since been established that depending on the amount of time a polymer is exposed to a gaseous reactant, the concentration of the inorganic material that diffuses through the film can be controlled; particularly when there are reactive groups on all or some of the polymer chains. A graphical depiction of the general principles behind VPI processes is shown in **Figure 3.3.**

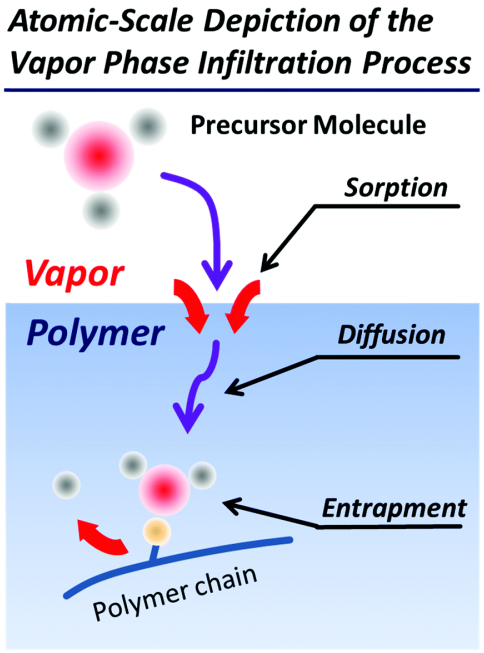

Figure 3.3: Graphical representation of the microscopic processes occurring during vapor phase infiltration of a polymer. Reproduced with permission from Leng, C. Z.; Losego, M. D. *Mater. Horiz.* **2017**, *4*, 747-771. Copyright Royal Society of Chemistry 2017.

Atomic layer deposition (ALD) instruments are widely available in a variety of academic and industrial laboratories, thus utilizing a method that employed an ALD machine to introduce an inorganic precursor into BCP patterns was targeted. ALD is a technique which uses self-limiting reactions, typically two distinct reactions that ultimately lead to the formation of monolayer films with smooth and uniform properties.[57] During an ALD process, a single atomic layer is grown when a gaseous precursor is adsorbed on a surface, the second reactant is then introduced to the sample which drives the reaction to completion constituting one ALD cycle. The ALD cycles can be sequentially performed on a given surface to systematically build up atomic layers where the desired final thickness dictates the numbers of cycle performed. An example of a surface that can be produced

with ALD is Al_2O_3; the process consists of introducing trimethylaluminum, $Al(CH_3)_3$ precursor gas. This is followed by introducing water vapor which converts the adsorbed $Al(CH_3)_3$ to Al_2O_3 completing the reaction cycle which can then be repeated.

Indeed, ALD has been used on polymer and BCP films for patterning applications. However, conventional ALD process schemes ($\leq$ 1 s gas pulse times, low reaction chamber pressures) typically result in the formation of a top surface layer with no diffusion into the polymer films, or formation of a spacer layer between features patterned by photolithography.[58,59] While conventional ALD has been an important technique for IC device fabrication, we wished to utilize a process which allowed for the complete diffusion of the inorganic precursor clear through the entire thickness of a film, rather than formation of a thin layer on top of the patterns. Such a technique has been established and used on BCP patterns as a modified ALD process called sequential infiltration synthesis (SIS).

3.3 SEQUENTIAL INFILTRATION SYNTHESIS AND ITS APPLICATION TO BLOCK-COPOLYMER LITHOGRAPHY

Sequential infiltration synthesis (SIS) relies on controlled reactions between a gas phase material and surface to precisely grow nanomaterials. The distinction between ALD and SIS is that in a SIS experiment, the gaseous reactants are given a much longer time to interact with the surface of which they are to be deposited on, allowing for diffusion and more complete reaction. An additional advantage of SIS when applied to BCP nanostructures is that it could be used to selectively modify specific domains of a BCP which can be controlled by installing certain functional groups to the polymer chains of one domain, whereas ALD will form a surface layer on a BCP film regardless of the polymer functionality. SIS was initially applied to PS-*b*-PMMA cylinders and lamellae modified with a variety of inorganic groups which selectively interact with the carbonyl

groups of the PMMA domains.[60–63] An illustrative summary of SIS on PS-*b*-PMMA is shown in **Figure 3.4** and suggests that after an initial SIS step which modifies the PMMA unit, other materials could potentially be grown off the modified sites that would otherwise not react with PMMA.

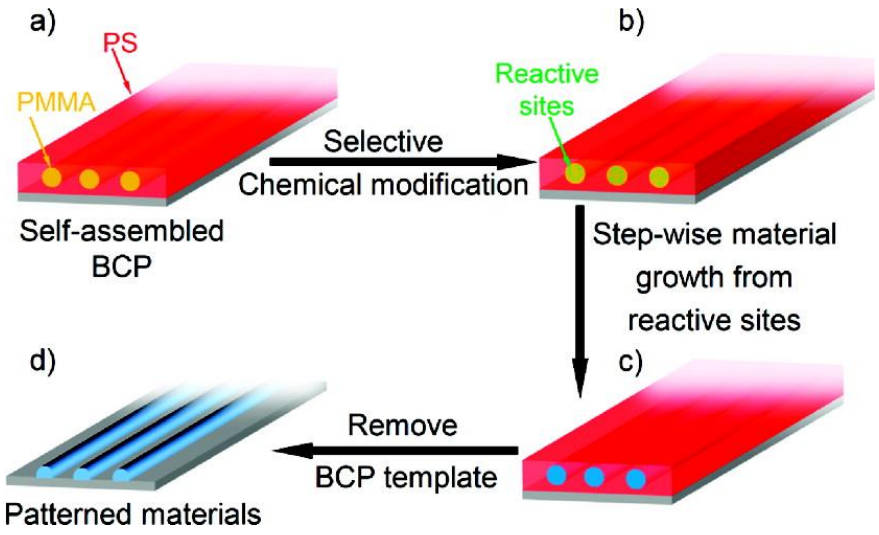

Figure 3.4: Graphical depiction of SIS on cylinder forming PS-*b*-PMMA with $AlMe_3/H_2O$. Reprinted with permission from Peng, Q.; Tseng, Y.; Darling, S. B.; Elam, J. W. *ACS Nano*, **2011**, 5, 4600-4606. Copyright 2011 American Chemical Society.

While there have been a number of promising results using SIS on BCP templates, with the exception of a more recent report utilizing poly(4-*tert*-butylstyrene-*block*-2-vinylpyridine), SIS studies have all been performed on PS-*b*-PMMA BCPs.[64] Indeed, the PMMA unit provides a convenient and selective group with a demonstrated affinity to react with a variety of gaseous precursors. However, the use of PS-*b*-PMMA should be viewed as limited due to the fact that the smallest features that can be generated from the BCP are ~ 27 nm and currently smaller features are necessary for next generation technologies.[46] Due to the fact that the Willson group has demonstrated the formation of 5 nm line/space

patterns generated using BCP lithography, one of the goals of this project was to investigate VPI of BCPs which are chemically distinct from PS-*b*-PMMA, thus demonstrating a process with a broader scope that could be applied to BCPs that suffer from poor etch performance or lack any appreciable etch contrast.

Furthermore, many of the materials generated after undergoing SIS or a VPI step(s) suffer from poor image quality which is dependent on the number of SIS cycles performed. The issues commonly encountered are displayed in **Figure 3.5** which contains the SEM images of lamellar patterns formed by L_0=41 nm (a) and L_0=27 nm (b) PS-*b*-PMMA infiltrated with alumina.[65] For clarity, the images marked "After ALD dep." represent the materials after a certain number of SIS cycles with $AlMe_3/H_2O$ and those marked with "All polymer removed" are the corresponding samples after undergoing RIE with O_2 plasma which presumably leaves behind only the aluminum oxide. According to Ruiz, et al. the color tone of the SEM images reverses going from 1 to 7 cycles whereby the modified PMMA domains are dark-colored in the samples which only had 1 cycle performed whereas the corresponding domains are brighter in color (compared to PS) in the samples subjected to 7 cycles.[65]

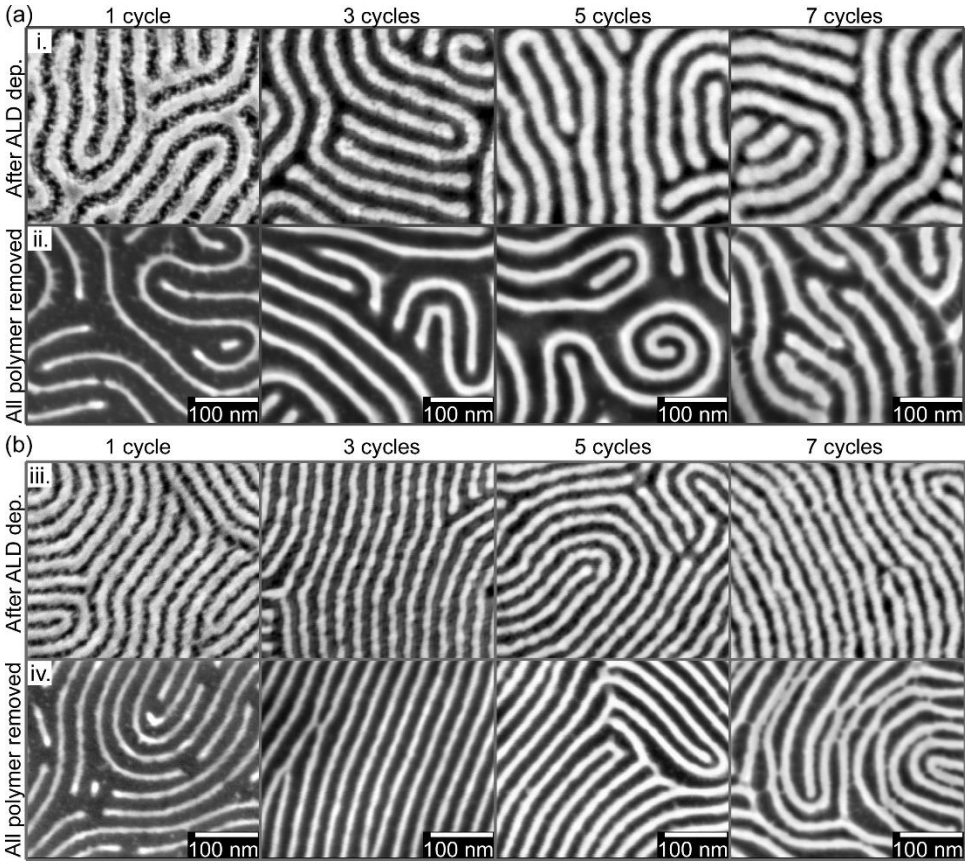

Figure 3.5: SEM images of (a) L_0=41 nm and (b) L_0=27 nm PS-*b*-PMMA after infiltration with alumina (i, iii) and after O_2 plasma etching (ii, iv). Reprinted from Ruiz, R.; Wan, L.; Lille, J.; Patel, K. C.; Dobisz, E.; Johnston, D. E.; Kisslinger, K.; Black, C. T. *J. Vac. Sci. Technol. B* **2012**, 30, 06F202. Copyright 2012, American Vacuum Society.

Upon careful inspection of **Fig. 3.5** two issues become apparent, the first of which is in the materials which were only subjected to 1 infiltration cycle, these materials appear rough, noncontinuous (fragments appear in the etched images), and porous. The second issue can be seen in the samples subjected to additional cycles, especially in those subjected to 7 cycles, which are found to have an increase in roughness, visible pattern collapse after plasma etch, and widening of the lines. In fact, in the study by Ruiz et al. the increase in the width of the patterns was so pronounced that it could be correlated. Using the metric

CD/L_0 as a measure of how different the patterns containing alumina are from those of the original BCP, after the single SIS cycle $CD/L_0 = 0.27$ due to the scarce amount of alumina constituting the patterns. With an average original $CD/L_0 = 0.53$ for both BCPs used in **Fig. 3.5**, it was found the CD/L_0 increased linearly at a rate of 0.04 per cycle.[65] While many of these issues can be minimized, we sought to utilize SIS while improving the quality of the materials made with this technology.

3.5 PROJECT REQUIREMENTS AND PRECEDENCE

In order to address the concern that as feature size (L_0) and therefore the feature height (film thickness) decreases there could be a loss of a significant amount of material after the final etch steps, we sought to incorporate a vapor-phase infiltration step in our process such that a metal oxide is created on one of the polymer domains of an aligned BCP. One way to achieve this goal, the BCP can be designed such that one of the BCP domain's bears an acid-labile group that can be removed following exposure to UV light in the presence of a photoacid generator (PAG). Furthermore, it was envisioned that this entire process could evoke a "zero-volume" change in the films, such that after the deprotection step and incorporation of the inorganic oxide, the films did not grow or swell relative to their original, as-cast film thicknesses/CD.

To begin designing an appropriate BCP for the purposes of this project, a suitable monomer needed to identified that would undergo a chemical reaction upon exposure to acid. Additionally, after the deprotection the resultant group needed to be compatible with inorganic precursors of interest, such as common ALD gases ($AlMe_3$, $TiCl_4$, etc.) and organo-silicons (HMDS, TMS-Cl, etc.). Two monomers were identified for these purposes: 4-*tert*-butoxycarbonyloxystyrene (TBOCS) and 4-*tert*-butoxystyrene (TBOS). Both TBOCS and TBOS are readily polymerized by a free-radical initiator such as AIBN.

Figure 3.6 shows the representative polymerization scheme for both monomers and their structures.

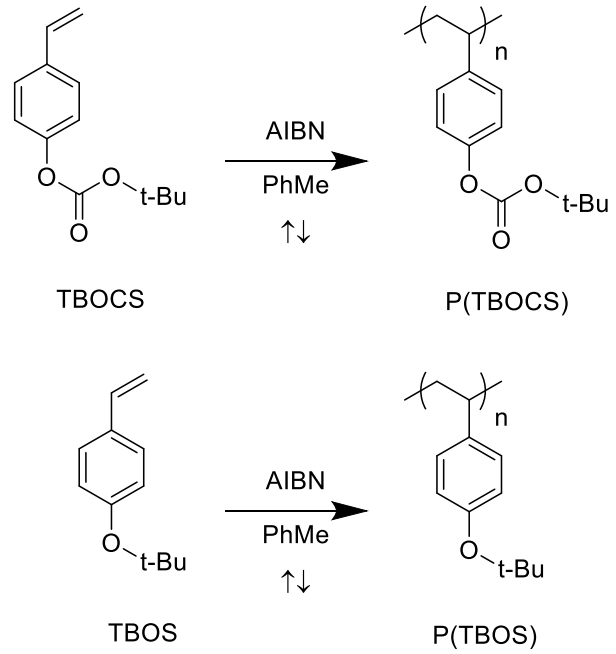

Figure 3.6: Polymerization reaction schemes of the monomers used in this work. P(TBOCS) = poly(4-*tert*-butoxycarbonyloxystyrene); P(TBOS) = poly(4-*tert*-butoxystyrene).

P(TBOCS) and P(TBOS) are both protected versions of poly(hydroxystyrene), (PHOST). P(TBOCS) has been extensively studied as a photoresist and is the first example of a chemically-amplified resist which was first invented by Dr. Willson and his coworkers at IBM.[66,67] Furthermore, both P(TBOCS) and P(TBOS) provide a convenient way to control the amount of mass or volume lost upon exposure to photoacid. The reaction of both P(TBOCS) and P(TBOS) with a photoacid is shown in **Figure 3.7** and **Figure 3.8** along with the reaction of PHOST with an organosilicon reagent. It can be seen in **Figure 3.7** that the deprotection of P(TBOCS) occurs concomitant with the liberation of CO_2 and

isobutylene gases whereas the deprotection of P(TBOS) releases only isobutylene gas, shown in **Figure 3.8**. Therefore, the liberated materials provide a convenient handle that can be used to match the mass or volume of the inorganic oxide that is to be introduced.

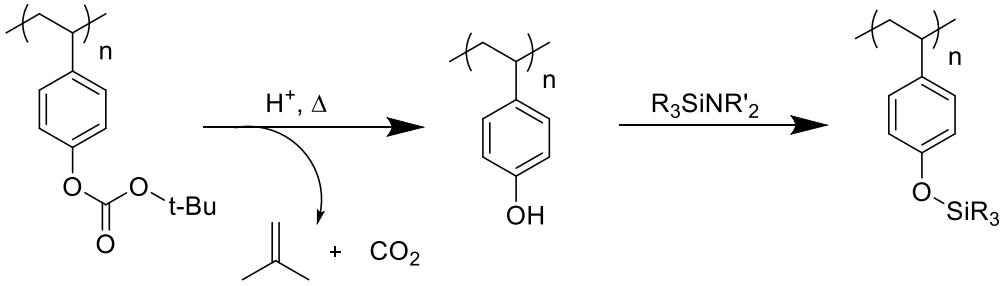

Figure 3.7: Representative reaction of P(TBOCS) with an acid and heat followed by the reaction with a generic organosilicon reagent.

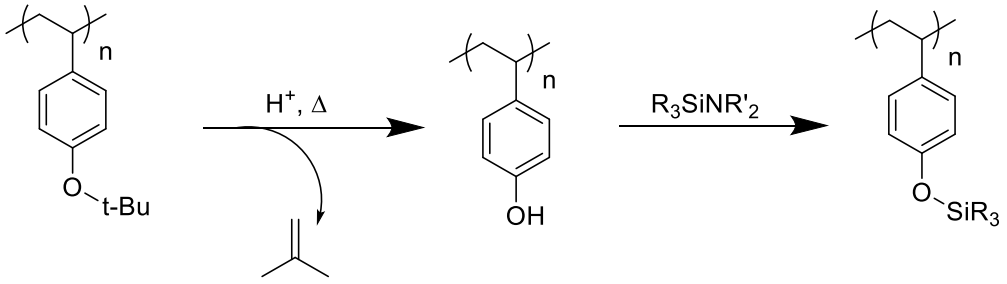

Figure 3.8: Representative reaction of P(TBOCS) with an acid and heat followed by the reaction with a generic organosilicon reagent.

In addition, P(TBOCS) was the principle material that was used to demonstrate the lithographic technique of "top-surface imaging" which involved exposing the deprotected, PHOST films to a gaseous silylating reagents (e.g., HMDS) to form a small layer containing a silyl ether which served as an etch barrier on patterns created using a photolithographic mask.[68–70] The silylation of commercially available PLASMASK®

resist (a phenolic novolac resin) films with HMDS was systematically investigated to the extent that a prescribed process was established which became known as the DESIRE (Diffusion Enhanced Silylating Resist) process.[71,72] However, it is useful to be reminded that the aforementioned studies were first reported in the late 1980's; at the time the ability to obtain 400 nm features was noteworthy while todays technological requirements are on the order of 5-7 nm. The impressive amount of data collected on the P(TBOCS) resist and the silylation of PHOST films thus provided evidence that inorganic oxide formation was possible and our efforts therefore first focused on establishing conditions for the silylation of PHOST films.

3.5 INITIAL INFILTRATION OF PHOST FILMS

In order to establish a reliable methodology and response of inorganic precursors reaction with PHOST, studies were untaken using the homopolymers of P(TBOCS) and P(TBOS). Initial studies were performed in collaboration with AMST for the infiltration experiments and in collaboration with LAM Research, who provided the analytical data after the infiltration experiments. While we are most grateful to both parties for their invaluable assistance in collecting this preliminary data, the lack of parameter control in regards to the VPI experiments (such as purge times, temperatures, etc.) limited the scope of the experiments that were initially undertaken.

To begin, films of P(TBOCS), P(TBOS), and control samples of poly(styrene) each formulated with a photoacid generator were spin cast from solution onto silicon wafers and subsequently exposed to UV-light, followed by a post-exposure bake (PEB) for 1 min at 100 °C to activate the thermolysis. The initial experiments focused on VPI of PHOST films with either Al or Ti. The film thicknesses, measured by ellipsometry, were recorded for the as-cast films and for the deprotected films, summarized in **Table 3.1**.

Table 3.1: Film thickness measurements of as-cast films of polymers and the corresponding film thicknesses measured after deprotection using a PAG. The film thickness lost is shown for reference.

Polymer	As Cast FT (nm)	Post photoexposure and bake (nm)	Loss (nm)
P(TBOCS) 1	289.2	190.7	98.5
P(TBOCS) 2	282.2	199.4	82.8
P(TBOCS) 3	279.9	195.2	84.7
P(TBOCS) 4	280.5	194.4	86.1
P(TBOS) 1	299.4	234.7	64.7
P(TBOS) 2	291.7	229.9	61.8
P(TBOS) 3	325.7	254.8	70.9
P(TBOS) 4	320.8	238.5	82.3
PS 1	286.6	N/A	N/A
PS 2	286.8	N/A	N/A
PS 3	277.6	N/A	N/A
PS 4	273.8	N/A	N/A

The study was designed to test several variables. All films would first be placed under vacuum for 8 h prior to the infiltration with inorganic reagents. For both the Al and the Ti reagents, the wafers were cleaved such that the same sample would be exposed to the different conditions. The infiltrations were performed at either 20 °C or at 60 °C using either a 5 s or a 300 s purge time. Following the VPI, the samples were analyzed for film thickness, d-SIMS (dynamic secondary ion mass spectrometry), and XPS (x-ray photoelectron spectroscopy). The film thickness data revealed that at all conditions tested, there was no incorporation of either Al or Ti. **Figure 3.9** graphically shows the data for the samples exposure to $AlMe_3$ for 300 s at 60 °C and **Figure 3.10** shows the corresponding data for exposure to Ti.

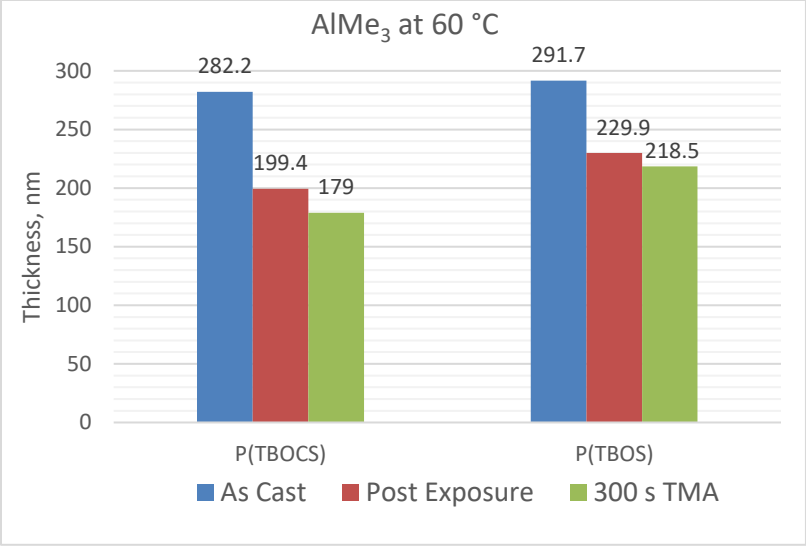

Figure 3.9: Film thickness data for samples of P(TBOCS) and P(TBOS) exposed to $AlMe_3$ for 300 s at 60 °C.

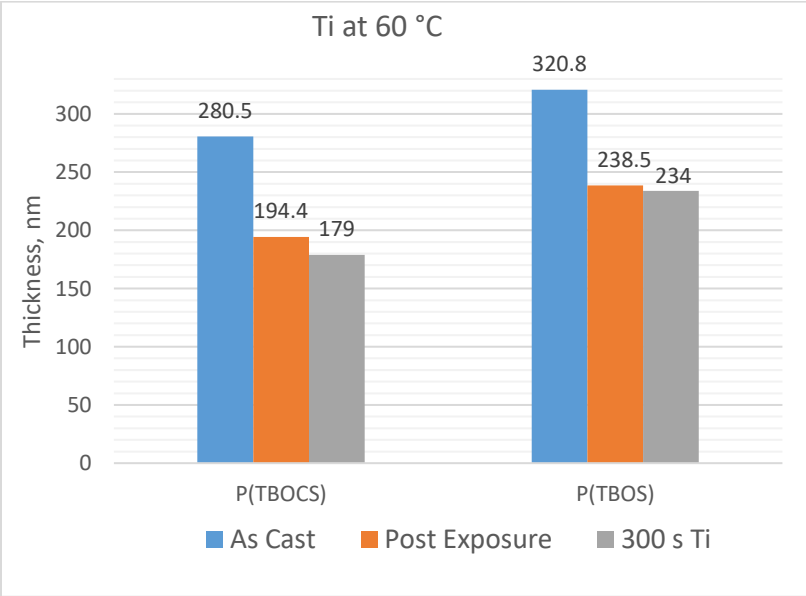

Figure 3.10: Film thickness data for samples of P(TBOCS) and P(TBOS) exposed to Ti gas for 300 s at 60 °C.

As previously mentioned, the samples were further analyzed by d-SIMS and XPS. The data from both those analyses suggested that neither Al or Ti was present throughout the bulk of the films. However, the d-SIMS data indicated a high concentration of Al and Ti on the surface of the films, suggesting either an impermeable "crust" had formed that prevented further penetration through the polymer films or the infiltration procedure performed was following an ALD-type growth of a thin monolayer on the surface of the films. Regardless, both of the scenarios were undesirable. The d-SIMS data collected from the films of P(TBOCS) and P(TBOS) exposed to $AlMe_3$ for 300 s at 60 °C are shown in **Figure 3.11** and **Figure 3.12** respectively, which corresponds to the samples described in **Figure 3.9**.

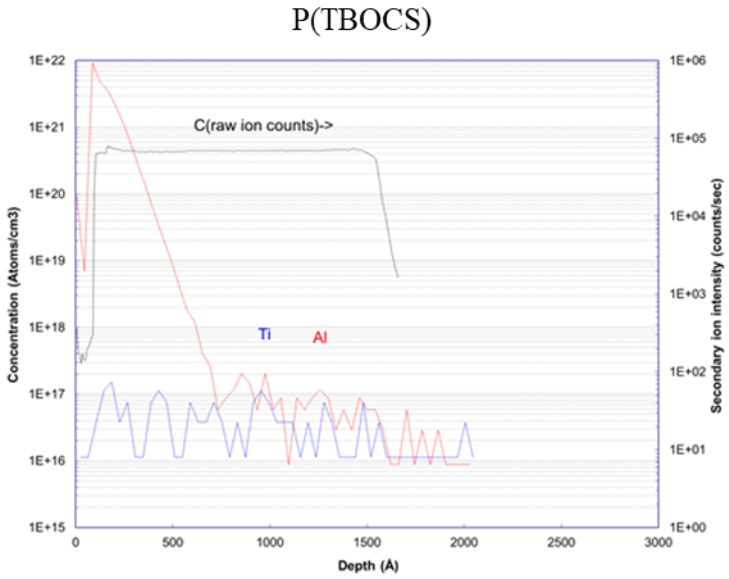

Figure 3.11: d-SIMS data collected after exposure of P(TBOCS) to Al for 300 s at 60 °C.

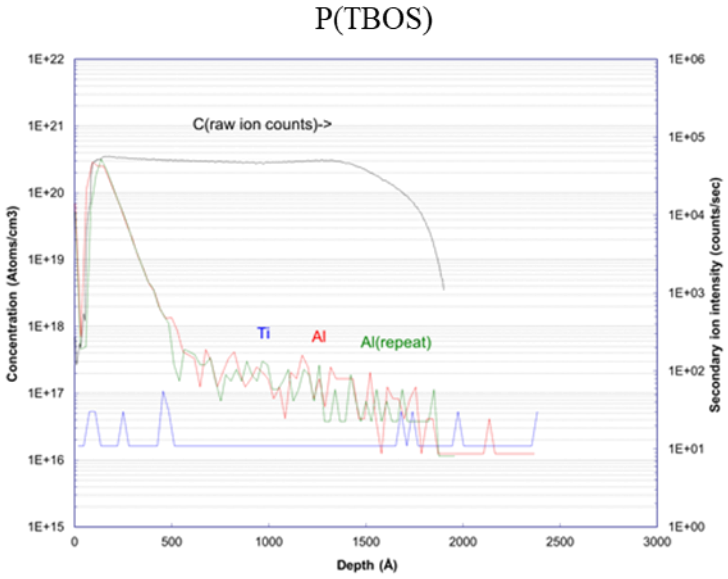

Figure 3.12: d-SIMS data collected after exposure of P(TBOS) to Al for 300 s at 60 °C. Note: the green data set measuring Al content is a duplicate measurement.

In light of initial results obtained with our collaborators, we sought to verify these results "in-house" at The University of Texas by executing the VPI processes using an ALD instrument that is available and capable of offering a variety of gaseous inorganic precursors (e.g., Al, Ti, Hf). The analysis was done with the assistance of the Texas Materials Institute which has a TOF-SIMS instrument (time-of-flight secondary ion mass spectrometry). While it is expected that depending on whether P(TBOCS) or P(TBOS) are used as the protected-PHOST films there will be an overall difference in film thickness that is measured after a deprotection step to yield films of PHOST, for the purposes of these experiments the incorporation of an inorganic precursor was the primary variable to be measured and thus only films formulated from P(TBOCS) were used. Two samples were prepared using a formulation of P(TBOCS) and the PAG, triphenylsulfonium nonaflate (TPS-Nf). After the polymer was spin-cast onto a silicon wafer, it was exposed UV-

radiation with λ = 254 nm for 1 min, followed by a 1 min PEB at 100 °C to give PHOST films. Using an ALD instrument, the PHOST films were exposed to AlMe3 vapor followed by H2O vapor at 100 °C to generate Al2O3. **Table 3.2** lists the film thicknesses for the as-cast P(TBOCS) films, the PHOST films, and the films after exposure to the Al precursor.

Table 3.2: Film thickness data for films exposed to $AlMe_3/H_2O$ at 100 °C using an ALD instrument. The number of cycles refers to the number of times the films were exposed to the gaseous reactants. One cycle represents a pulse of $AlMe_3$ gas followed by a pulse of H_2O vapor.

As-cast P(TBOCS) FT (nm)	PHOST FT (nm)	FT after ALD with $AlMe_3/H_2O$ (nm)
24.9	14.0	24.3 (110 cycles)
48.6	29.4	47.5 (210 cycles)

At the time of these experiments, I was not permitted to modify the pulse sequences, therefore the pulse times (introduction of the gaseous reactants into the sample chamber) were very short 0.015 s, conditions under which an ALD growth was expected rather than the desired diffusion into the films. TOF-SIMS data were collected for the films described in **Table 3.2**. The Al content in the film was measured by sputtering through films down to the substrate (SiO2) as well as the organic content known be present such as -CO and -CH by first sputtering through a PHOST film that had not been exposed to the Al gas, generating a "signature" for the polymers response. The data collected from these experiments are shown in Figure 3.13 for the 24.3 nm thick film and in Figure 3.14 for the 47.5 nm thick film.

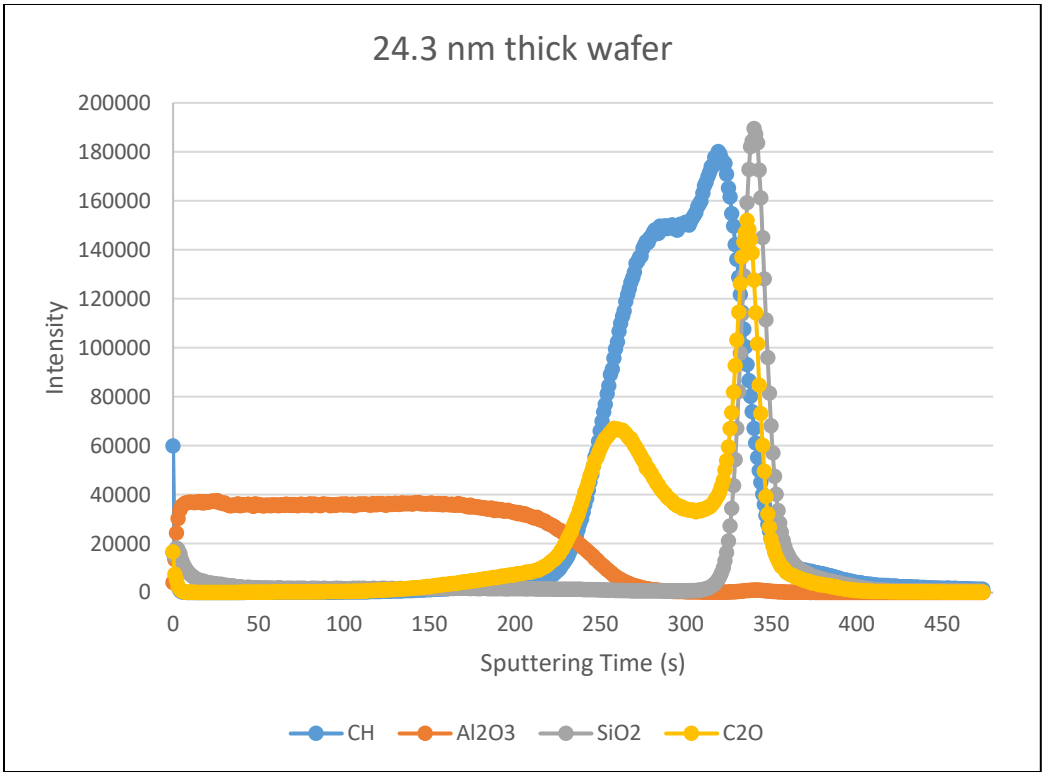

Figure 3.13: TOF-SIMS data for the 24.3 nm thick sample exposed to Al gas using an ALD instrument. The corresponding film thickness details are contained in **Table 3.2**.

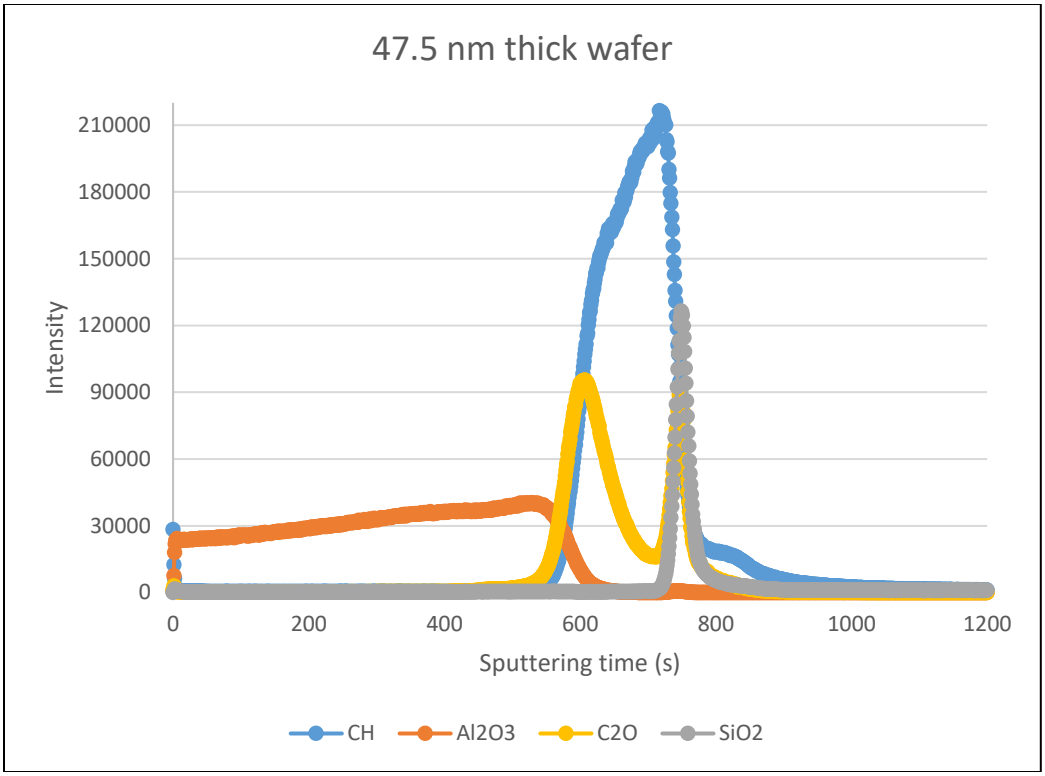

Figure 3.14: TOF-SIMS data for the 47.5 nm thick sample exposed to Al gas using an ALD instrument. The corresponding film thickness details are contained in **Table 3.2**.

As exhibited in the TOF-SIMS data shows that there is a detectable amount of Al measured at the beginning of the analysis, which quickly disappears upon detection of the organic matter which is attributed to the PHOST film. Overall, these data describe a discrete layer of Al_2O_3 on top of the PHOST films which did not diffuse and presumably, did not interact with the hydroxyl groups to an appreciable extent. The ideal data would have detected Al content throughout the detection of the organic content terminating with the signal attributed to SiO_2.

3.6 EXPLORING THE SILYLATION OF PHOST FILMS

The results summarized in the previous section, the use of inorganic reactants such as Al and Ti did not appear to be a viable route partially due to very short pulse times. Consequentially, because there was well documented evidence that organosilicon reagents, particularly hexamethyldisilizane, HMDS react with the hydroxyl groups of PHOST films to form O-Si bonds, we wanted to establish that these experiments could be reproduced using the instrumentation available today. Additionally, because the majority of the studies investigating top-surface imaging and the DESIRE process using organosilicon reagents were reported at a time when the leading technology was producing features on the micron scale, we needed to establish that the same results could be obtained on the nanometer scale relevant to today's requirements.

A commercially available HMDS oven was used to expose films of PHOST. Because HMDS ovens in IC fabs are typically used to create a layer of an adhesion promoter on silicon wafers, the ovens function by an automated control system that is restricted to a few pre-set recipes that control the sequence of gases introduced to wafer samples, as well as the temperature and pressure of the gas. While this inability to modify the experimental conditions freely was seen as a disadvantage, an initial experiment was performed to establish if the method was viable. PHOST films were placed in a Teflon sample carrier in an HMDS oven and run using a sequence that purged the sample chamber with HMDS vapor for 5 min after an initial period of evacuation cycling with $N_{2(g)}$ all of which was performed at a temperature of 150 °C. The PHOST samples had films thicknesses close to what would be expected for BCP materials with the exception of two thicker samples, the thickest sample match what had previous been disclosed. The data is summarized in **Table 3.3**.

Table 3.3: Results from HMDS silylation experiment on PHOST films. HMDS oven was used with a pre-set 5 min HMDS purge time and at 150 °C.

As-cast P(TBOCS) FT (nm)	PHOST FT (nm)	Post HMDS silylation FT (nm)
26.2	14.5	15.3
24.8	13.9	14.8
42.8	28.3	26.7
41.6	27.4	26.4
256.1	147.5	145.6
701.4	461.3	745.8

Inspection of the results summarized in **Table 3.3** provides some evidence that the incorporation of HMDS in PHOST films, which were less than a certain film thickness did not occur. While this observation was not anticipated, this unexpected result warranted further investigation as this result had not been reported previously. Therefore, a thorough investigation was undertaken to see if we could explain why PHOST only incorporated HMDS at or above a certain film thickness and if this was true for other silylating reagents. These studies constitute the material for Chapter 4.

3.7 EXPERIMENTAL

3.7.1 Polymer Materials

The synthesis of P(TBOCS) and P(TBOS) has been previously described.[66,73] Solvents were purchased from commercial suppliers and used as received.

3.7.2 Thin-film preparation and photoexposure

Spin coating and PEB were performed on a Brewer Science 100CB spin coating/hot plate station. Typical spin-coating solutions contained 4 wt% (PAG to polymer wt) triphenylsulfonium nonaflate in a solution of PGMEA. All solutions were filtered through a PTFE filter prior to use. Large area exposures at $\lambda = 254$ nm and intensity of 6.48 mW/cm^2 was performed using a Canon mask aligner without a mask present. Ellipsometry was performed at UT-Austin using a J.A. Woollam Co, Inc. VB 400 VASE Ellipsometer with wavelengths from 382 to 984 nm and a 65° angle of incidence.

Chapter 4: A study of the silylation of PHOST films with HMDS

4.1 Film thickness and how it affects the silylation of PHOST films

As described in Chapter 3, it was observed that upon exposure to HMDS vapor only PHOST films with greater than a film thickness (FT) incorporated/reacted to form the expected silyl ether as indicated by a "growth" in film thickness. In the course of these studies, two main questions were posed and tested:

1. Does the temperature of the HMDS exposure have an effect on the reaction due to a difference in the glass transition temperature (T_g) of the PHOST films of differing thicknesses?
2. Do PHOST films of relatively thinner thicknesses incorporate other silylating agents or is this phenomenon observed for all silylating agents?

4.2 Investigating the effect of temperature on the silylation of PHOST films

The correlation between film thickness (along with other properties such as molecular weight and composition) and the glass transition temperature T_g is a well-documented and understood relationship.[74–79] Moreover, reports which study this relationship also connect T_g to polymer film density. Relative to this work, studies have shown for a variety of polymers and even polymer blends, that the apparent or effective T_g of a polymer film is found to decrease as film thickness decreases. This information lead us to speculate that the samples with a relatively thinner film thickness that were exposed to HMDS were being placed in an environment above their T_g which was causing the films to undergo some kind of densification that made them become impermeable to the silylating material. Although previous work reported using silylation reaction temperatures similar (150 °C to 170 °C) to the temperature at which I had run the HMDS oven (150 °C),

those were mainly focused on silylating the top-surface of materials with very thick films relative to the those of interest in this study (20-100 nm).[70,80] However, it has been explained that silylation using HMDS is found to occur at a faster rate (1 min) at elevated temperatures and is the reason that these conditions were used.[70,71,80] Since much of this work was performed by individuals with ties to the semiconductor industry, it is understandable that this efficiency would be capitalized on.

While the work previously reported on the silyation of PHOST films with HMDS suggests that elevated temperatures such as 150 °C are suitable for performing the reaction, the films used were of much greater film thickness than what I was interested in and thus, this complimentary work was pursued. HMDS silylation experiments were run at a reduced temperature of 100 °C. The film thickness data were recorded using ellipsometry for the P(TBOCS) precursor films, the corresponding PHOST films following the photo-deprotection reaction, and after the HMDS exposure at 100 °C; these data are summarized in **Table 4.1**.

Table 4.1: Film thickness measured for HMDS silylation at 100 °C. A 5 min HMDS purge was used for all samples.

As-cast P(TBOCS) FT (nm)	PHOST FT (nm)	Post-HMDS silylation at 100 °C FT (nm)
25.0	14.2	14.6
41.4	27.3	24.7
334.4	201.9	202.1
388.4	235.2	234.6
623.5	383.0	647.7

As summarized in **Table 4.1** performing the silylation reactions at a lower temperature of 100 °C appeared to have no effect on the thinner films. Only the 383 nm PHOST film incorporated HMDS. Interestingly, before running the experiment tabulated above another sample was prepared with a PHOST film thickness of 387 nm, this sample was heated above the T_g of PHOST (ca. 155 °C) at 170 °C for 5 min, which reduced the film thickness to 355 nm (difference in film thickness may be attributed to residual solvent loss). This sample was then exposed to HMDS alongside the samples from **Table 4.1** and was found to not have incorporated any HMDS. The series of process steps just described is shown graphically in **Figure 4.1**.

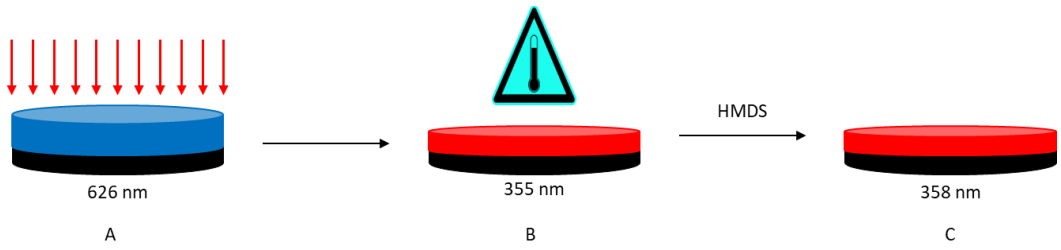

Figure 4.1: Experiment testing the effects of heating a sample above the T_g of PHOST. (A) photoexposure of P(TBOCS) to form PHOST (red) (B) heating the PHOST at 170 °C for 5 min (C) no HMDS incorporation measured as exposing the PHOST film to HMDS.

The experiment described by **Figure 4.1** suggested that if the "thinner" films of PHOST being measured had a significantly different T_g than their "thicker" counterparts, then perhaps heating either above or close to the effective T_g was causing the films to soften or densify in such a way that they are not permeable to the silylating agent. In order to gain more insight into the T_g of a film with a thickness below one that does react with HMDS. The T_g of a 180 nm and a 370 nm thick PHOST, was measured. The T_g of each film was measured using variable temperature ellipsometry, which measured the film thickness over

time as the sample was gradually heated. The data are then fit and the T_g can be calculated.[81] The variable temperature ellipsometry data was collected from approximately 50 °C to 200 °C. The data for both samples is graphically shown in **Figure 4.2**. Unfortunately, due to the limitations imposed by the data collection, films with a thickness below 100 nm could not be accurately measured by this method.

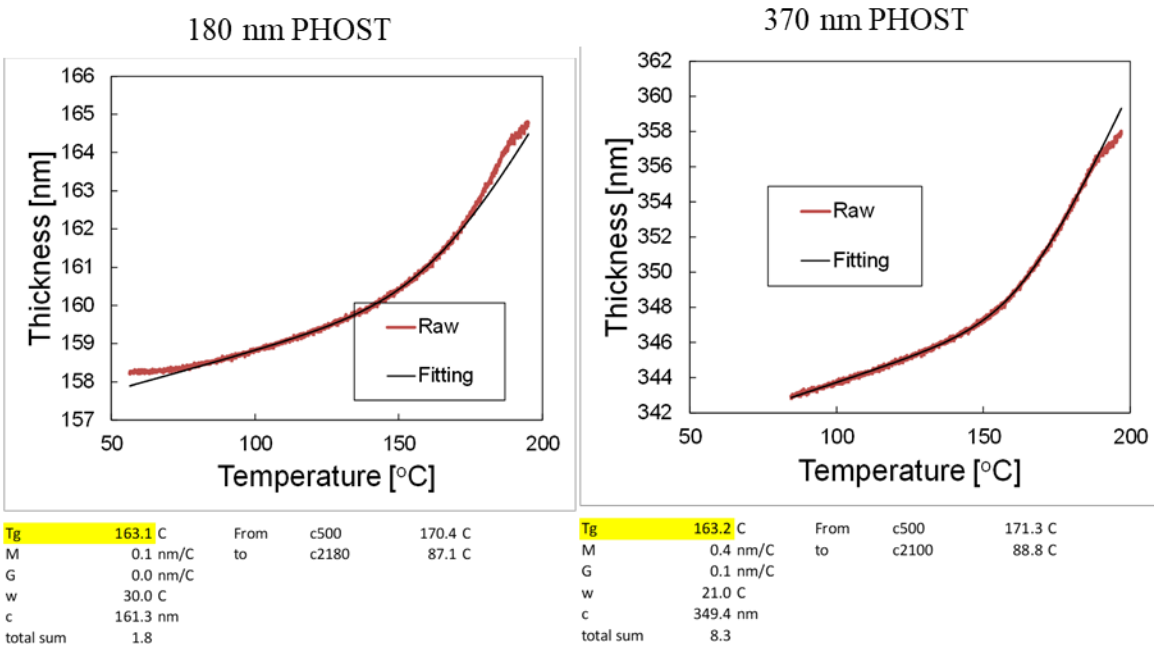

Tg	163.1 C	From	c500	170.4 C
M	0.1 nm/C	to	c2180	87.1 C
G	0.0 nm/C			
w	30.0 C			
c	161.3 nm			
total sum	1.8			

Tg	163.2 C	From	c500	171.3 C
M	0.4 nm/C	to	c2100	88.8 C
G	0.1 nm/C			
w	21.0 C			
c	349.4 nm			
total sum	8.3			

Figure 4.2: Variable temperature ellipsometry data. Raw data was collected from the ellipsometer and is not altered. Fitting data refers to the data after it has been fit to a theoretical model.[81]

The T_g values calculated for the two PHOST films of different film thicknesses are highlighted in yellow in **Figure 4.2** and indicate that both have approximately the same measured T_g value. This result therefore contradicts the assumption that the thinner films that do not react with HMDS have a T_g which is significantly different from the "thicker" films which ultimately leads to some sort of densification process in the films.

In addition to the experiments performed above, a follow-up experiment from the VPI experiments described in Chapter 3 was also performed at 100 °C. These experiments were again performed with an ALD instrument; however, the pulse sequences were modified such that a 1 s delivery of the gases could be achieved; a significant improvement over the 0.015 s which was used previously. These experiments were again performed using $AlMe_3/H_2O$ and the data from the samples tested is contained in **Table 4.2**.

Table 4.2: Film thickness data for two samples exposed to Al gas at 100 °C using a 1 s pulse sequence.

As-cast P(TBOCS) FT (nm)	PHOST FT (nm)	Post ALD with $AlMe_3/H_2O$ at 100 °C FT (nm)
25.5	15.2	17.0
41.4	27.2	28.7

As further evidenced by the data shown in **Table 4.2** lowering the temperature at which the "thinner" PHOST samples are exposed to the inorganic reactants does not result in a significant change in the reactivity of the films. Overall, based on the data presented in this section, the effect of temperature on the reactivity of thin films of PHOST does not appear to play a role. While it was initially hypothesized that there would be a measured difference in the T_g between the thick and thin film samples, this was shown to not be the case. However, when a sample with a film thickness that should have qualified it for HMDS incorporation was heated above the T_g of PHOST prior to exposure to the HMDS vapor, it did not react. This result complicated any attempt to draw a definitive conclusion.

4.3 EXPLORING OTHER SILYLATING AGENTS WITH THIN FILMS OF PHOST

Although HMDS was the only silylating agent that was readily accessible in an apparatus specifically built for exposing thin-films to the vapor, a number of viable precursors exist that could be utilized by other means. In order to introduce a vapor phase reactant to thin films, I worked with the glass shop at UT-Austin to build a simple yet very effective device which would allow the reaction chamber to be placed under a static or dynamic vacuum. Additionally, the temperature where the wafer samples were held could be controlled independently from the temperature of the precursor which usually needs to be vaporized from the liquid phase and/or heated in some cases. For clarity the device is pictured in **Figure 4.3**.

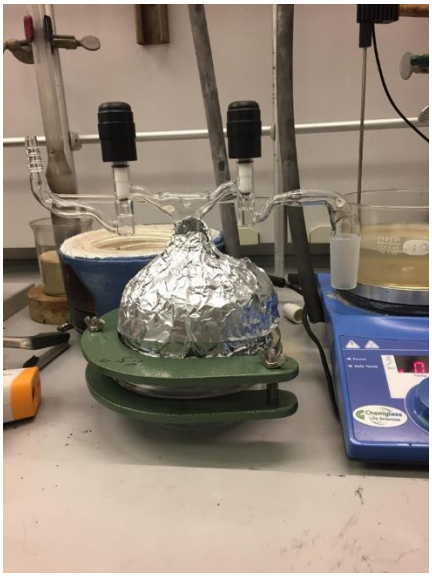

Figure 4.3: Apparatus designed for introducing other silylating agents to thin films. The main chamber is covered with Al foil to assist in keeping the temperature stable.

Although other silylating agents were investigated such as trimethylsilyl chloride, only the most successful one identified will be discussed in this dissertation. Using the

reaction chamber shown in **Figure 4.3**, I studied the reaction of dimethylsilyl dimethylamine (DMSDMA). One of the reasons DMSDMA was chosen as a silylation agent can be illustrated in comparing **Figure 4.4** and **Figure 4.5**.

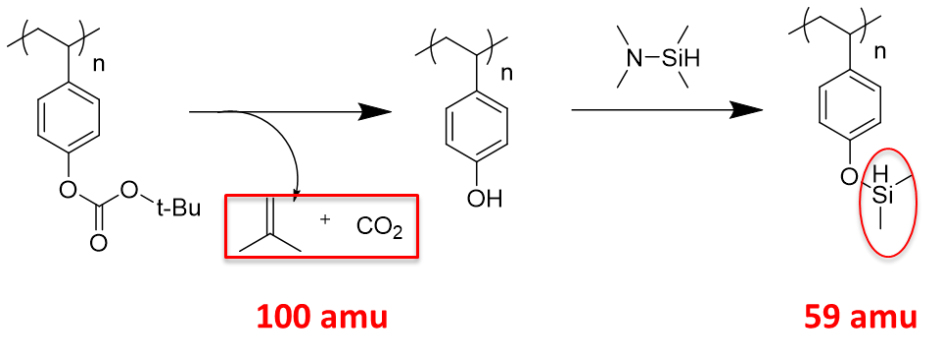

Figure 4.4: Chemical reaction of DMSDMA with PHOST derived from deprotection of P(TBOCS).

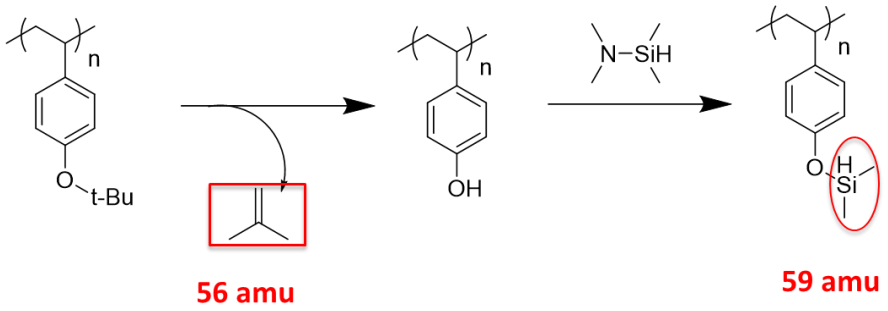

Figure 4.5: Chemical reaction of DMSDMA with PHOST derived from deprotection of P(TBOS).

Shown above in **Figure 4.4** and **Figure 4.5** the mass lost upon deprotection of P(TBOS), 56 amu and the mass gained upon incorporation of DMSDMA, 59 amu is nearly

the same value. In referring back to the original goals of this project, this almost equivalent loss and gain in mass fulfills one of the criteria which was to achieve a “zero-volume” change process. Therefore, DMSDMA was an obvious choice for a silylation reagent for future BCPs with one of the blocks being P(TBOS). To test the utility of DMSDMA in silylating PHOST films, samples of P(TBOS) formulated with 5 % PAG were spin-cast onto silicon wafers and photoexposed and baked to give PHOST films. The PHOST films were placed in my reaction chamber at a temperature of 150 °C and left under vacuum for 10 min to remove any residual water from the films. DMSDMA which has a boiling point of 67 °C was heated just under its boiling point at 57 °C. Once the samples had been evacuated for the allotted time, the reaction chamber was brought under static vacuum, and the valve between the chamber and the flask containing a small volume of DMSDMA was opened to allow the vapors to interact with the wafer samples. While maintaining the aforementioned temperatures, the reaction was allowed to run for 30 min. After which time, the samples were removed and analyzed by ellipsometry. Based on what I had already learned from the studies with HMDS, the film thicknesses used for this initial experiment were made to be “thicker” in order to establish if this was a viable precursor, with the exception of two relatively thinner films. The data from this experiment is summarized in **Table 4.3**.

Table 4.3: Film thickness data for samples of PHOST derived from P(TBOS) exposed to DMSDMA. Samples were kept at a temperature of 150 °C under static vacuum and the DMSDMA was kept at a temperature of 57 °C. The reaction was allowed to proceed for 30 min.

As cast P(TBOS) FT (nm)	PHOST FT (nm)	Post DMSDMA exposure FT (nm)
527	375	543
456	320	465
414	300	428
413	286	417
162	110	161

The results summarized in **Table 4.3** were satisfying, since all samples tested appear to react with DMSDA under the conditions tested and the films "grew" back to almost the same thickness as the parent P(TBOS) film. The last entry in **Table 4.3** in particular was most promising, with a PHOST film thickness of 110 nm this was the surely the thinnest film I had tested with a silylating agent that demonstrated an ability to grow back after exposure.

In light of these promising results, it was decided that efforts should be focused on evaluating BCPs which incorporate the 4-*tert*-butoxystyrene monomer in order to realize goals of this project and apply the work described in this Chapter. The details of the synthesis and work on the self-assembly of a series of BCPs containing 4-*tert*-butoxystyrene is reserved for Chapter 5.

Chapter 5: Block-copolymers containing 4-*tert*-butoxystyrene

5.1 Establishing a Strategy for using BCPs in this project

To begin, it is useful to be reminded of the overall goal that this project has been designed to achieve: design a functional block-copolymer that is capable of selectively incorporating an inorganic reactant to impart etch contrast to self-assembled patterns. This process should also proceed without a net change in film thickness between the self-assembled parent BCP patterns and those functionalized with an inorganic oxide. In Chapter 4, it was established that the 4-*tert*-butoxystyrene monomer would be used as one of the blocks in a BCP. Before beginning the discussion of the three BCPs which were synthesized for this project, it is important to understand how these materials would be implemented. **Figure 5.1** shows the expected process steps which were envisioned for this project in order to achieve self-assembled BCP patterns containing a metal-oxide.

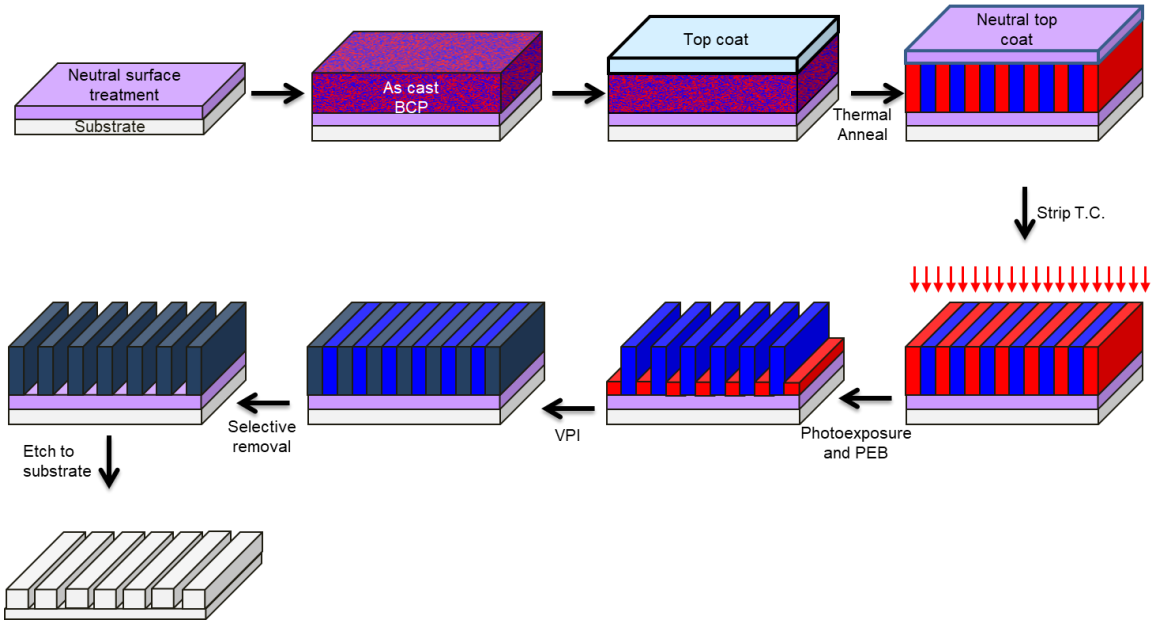

Figure 5.1: Process steps envisioned for this project. The final graphic represents the patterned substrate.

To form BCP patterns of perpendicularly orientated lamellae, the process steps anticipated begin with the typical self-assembly processes which were described in Chapter 2. After identifying a neutral substrate and interfacial layer, a BCP formulated with a photoacid generator (PAG) is spin-cast onto a substrate modified with the neutral surface treatment or XST. The neutral interfacial treatment or top-coat is then spin coated on top of the BCP layer from an orthogonal solvent. Following, the film stack is heated above the T_g of the BCP to thermally anneal the polymer. After, the top coat is then removed by a stripping solvent or by etching.

Completing the aforementioned steps should yield fingerprint patterns of the BCP. For the purposes of this project, the BCP contains a block of P(TBOS) which can further be exposed to UV-radiation and subjected to a PEB step which should liberate isobutylene to yield a PHOST block. The PHOST containing BCP can then undergo vapor-phase infiltration (VPI) with a gaseous reactant such as the silylating agent dimethylsilyl dimethylamine, DMSDMA restoring the film height to its original state. The remaining organic block can then be removed leaving behind a sacrificial etch mask of the modified block which can be patterned into the substrate.

Although some of the fundamental details of this process could were established using homopolymers of P(TBOS), transferring the basic processes to a BCP system involved balancing an array of variables which had to be carefully considered. To the best of our knowledge, this would be the first example of this type of lithographic process. At the very least, no process could be identified which report a BCP undergoing two chemical transformations (deprotection) post-self-assembly that did not cause a distortion in the patterns. Moreover, while there is a collection of reports on copolymers incorporating 4-*tert*-butoxystyrene, the ultimate target is typically poly(4-hydroxystyrene) which cannot be

used in anionic polymerizations of narrowly disperse copolymers. Thus, these polymers are typically hydrolyzed in acidic solutions post-synthesis and are never applied to any thin film investigations. Only a handful of studies deal with copolymers with a block of P(TBOS), however the self-assembly data is limited.[82–86] Nevertheless, the synthesis and evaluation of BCPs containing P(TBOS) was pursued which proved to yield polymers with interesting and unexpected properties. The details of each BCP synthesized is chronicled herein.

5.2 POLY(STYRENE-*BLOCK*-4-*TERT*-BUTOXYSTYRENE)

As one of the simplest iterations of a BCP containing P(TBOS), the first BCP targeted was poly(styrene-*block*-4-*tert*-butoxystyrene), PS-*b*-P(TBOS). In order to obtain BCPs with narrow polydispersity values and with molecular weights which can be precisely controlled, living anionic polymerization is the synthetic method utilized for all of the BCPs reported in this dissertation. Shown in the reaction scheme in **Figure 5.2**, the anionic synthesis involved sequential addition of monomers.

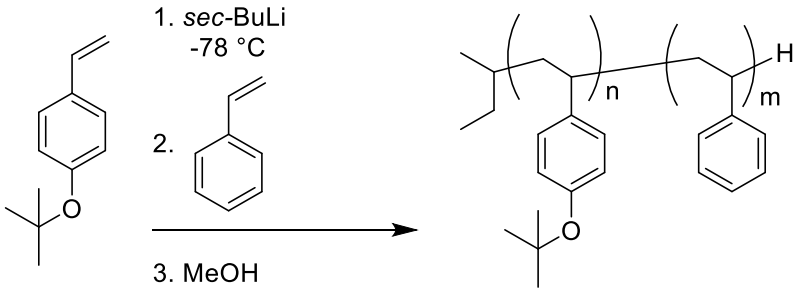

Figure 5.2: Reaction scheme for the synthesis of PS-*b*-P(TBOS)

Using the synthesis of PS-*b*-P(TBOS) as an example of the procedure for performing anionic polymerization, once the monomers have been thoroughly purified to sufficiently remove all traces of water and oxygen, the *sec*-BuLi initiator is added to a volume of THF at -78 °C under an inert atmosphere. The first monomer is added to the initiator, the first block of the BCP is formed which then initiates growth of the second block upon monomer addition by the living anion. Once complete, the reaction is quenched and a monodisperse BCP is obtained after a straightforward purification. In the case of PS-*b*-P(TBOS), two molecular weights were targeted for the synthesis. The characterization data is summarized in **Table 5.1**.

Table 5.1: Characterization data for PS-b-P(TBOS) BCPs. Data was measured by SEC.

BCP	$M_{N,,B1}$ (Da)*	$Đ_{B1}$	$M_{N,\,BCP}$ (Da)	$Đ_{BCP}$
PS-*b*-P(TBOS)-1	9,829	1.06	23,015	1.03
PS-*b*-P(TBOS)-2	8,642	1.08	19,731	1.03

*$M_{N,B1}$ = M_N measured from an aliquot taken of the first block

With the BCP in hand, I began two independent efforts. Working with our collaborators at LAM Research, we wanted to establish the selectively of the silylating agent for only the PHOST block. This information would help support future etch data and image analyses of patterns which could reliably be attributed to the silylated block. The homopolymers constituting the BCP; PS and P(TBOS) were used to test thin films exposed to several conditions, summarized in **Table 5.2**. The P(TBOS) homopolymer contained PAG in the films. Using dimethylsilyl dimethylamine, DMSDMA as the silylating agent

the films were placed under vacuum at 150 °C for 10 min, after the exposure vessel was placed under static vacuum and DMSDMA (heated at 51 °C) was allowed to diffuse into the sample chamber for 30 min.

Table 5.2: Sample details for homopolymer films of P(TBOS) and PS. Samples #2 and #5 were the as-cast homopolymers exposed to DMSDMA. Sample #3 was PHOST. Sample #4 and #6 were the as-cast homopolymers that were not exposed to any further process steps. Sample #5 was found to de-wet during the silylation process or it was thought that PS was dissolved away by the DMSDMA vapor.

Sample #	Polymer/Process steps	As-cast FT (nm)	PHOST FT (nm)	Post silylation FT (nm)
1	P(TBOS)/photoexposure + silylation	167	112	165
2	P(TBOS)/silylation	165	N/A	162
3	P(TBOS)/photoexposure	166	113	N/A
4	P(TBOS)	166	N/A	N/A
5	PS/silylation	158	N/A	-
6	PS	162	N/A	N/A

The purpose of creating the samples detailed in **Table 5.2** was to detect and quantify the Si content throughout the bulk of the films. It was expected that sample #1 would be the only sample containing Si throughout the bulk of the films. The samples were studied using dynamic secondary-ion mass spectrometry (d-SIMS) and x-ray photoelectron spectroscopy (XPS), these two methods provide complementary information regarding the contents of measured materials: d-SIMS provides a depth profile and elemental analysis with incredibly high precision being sensitive enough to differentiate between hydrogen and deuterium,[87] XPS also provides elemental analysis and can be used to quantify

elements and identify functional groups on polymers.[88] Given the large amount of data generated from these experiments, only a select few will be shown herein. Starting with **Figure 5.3**, the XPS data from sample #1 (**Table 5.2**). Satisfyingly, this data showed Si detected throughout the bulk of the film with a maximum value of 10.6 % detected at 695 s (blue dashed line).

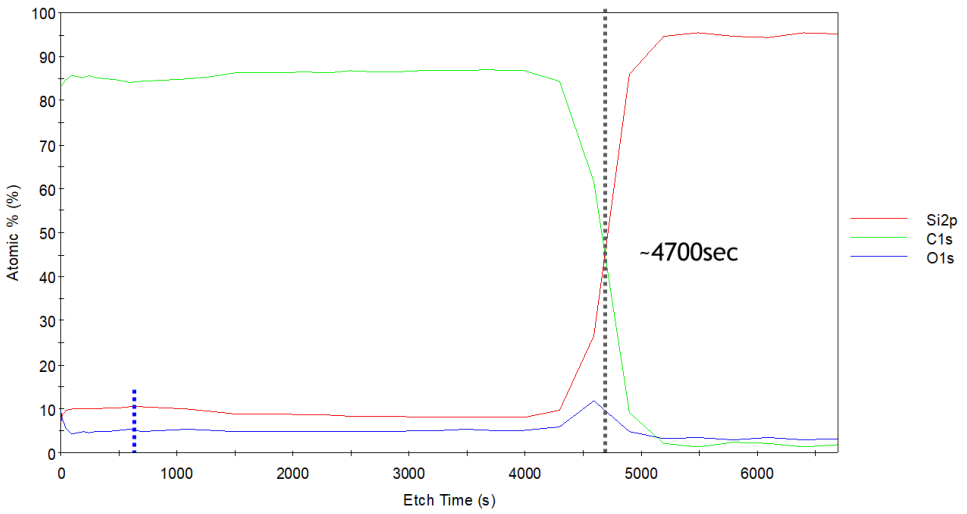

Figure 5.3: XPS data measured for Sample #1 from Table 5.2. The blue dashed line indicates the time at which the highest amount of Si was detected.

In order to support the assertion that the silylation with DMSDMA is selective only for PHOST, the analytical data would need to indicate no Si detected in the bulk of Sample #2. Indeed, this was found to be true, with only 0.5 % Si observed at the surface and no Si detected in the bulk of the film. The XPS for Sample #2 is shown in **Figure 5.4**.

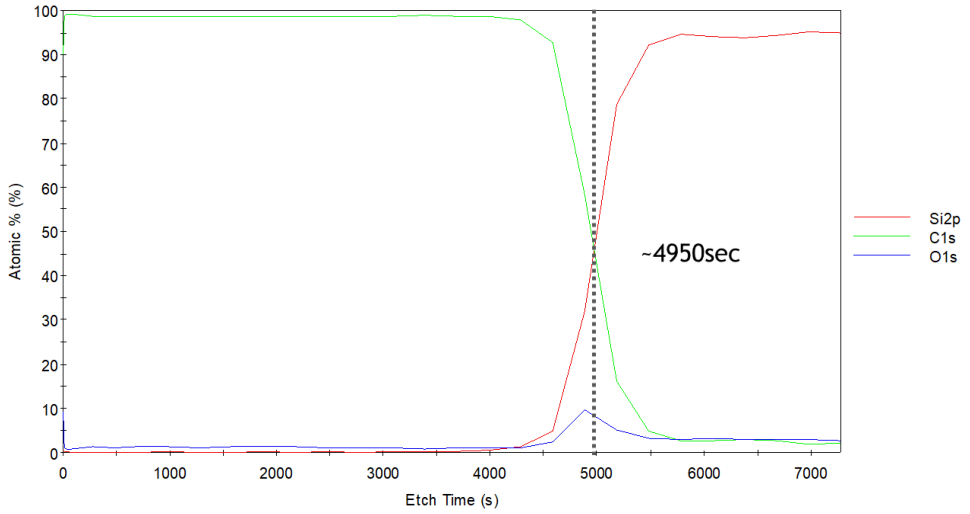

Figure 5.4: XPS data measured for Sample #2 (Table 5.2).

The XPS data collected from all samples except for Sample #1 did not indicate the presence of Si in the bulk of the films. The complimentary data measured by d-SIMS also indicated that the silylation with DMSDMA was selective. However, being a comparatively more sensitive technique, the data was not as absolute as the XPS. In the depth profiling performed during the d-SIMS experiments of the 6 samples tested, the average amount/concentration of Si in the bulk can be quantified. This data for all samples is graphically summarized in **Figure 5.5**.

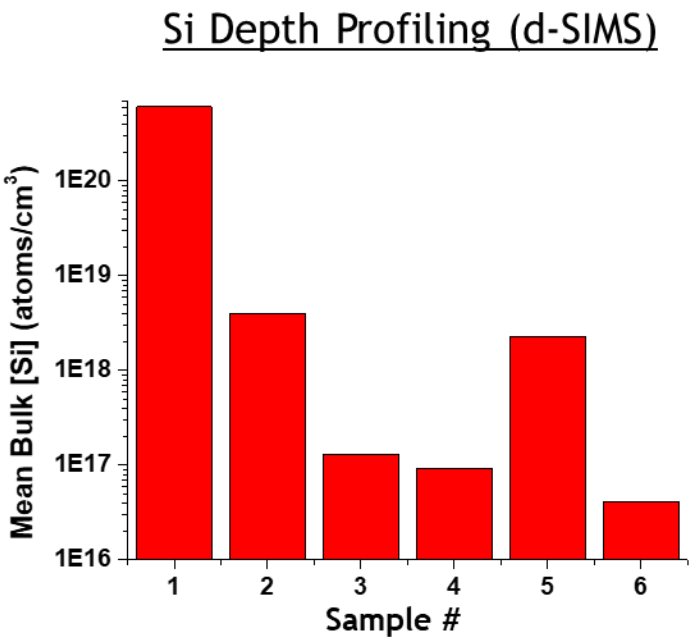

Figure 5.5: d-SIMS data summary for all samples. Data shows only the average Si content detected in the films.

The d-SIMS data shown in **Figure 5.5** indicates that Sample #1 had the highest amount of Si throughout the bulk of the film. While Si was detected in the other samples which were exposed to the silylating conditions (Samples #2 and #5), the amounts detected were approximately 100 times less than the amount detected in Sample #1 but more than what was detected in the control films #3, #4, and #6.

Collectively, the XPS and d-SIMS data provides compelling evidence to conclude that the silylation process with DMSDMA is indeed selective for PHOST. Although the films which should not have contained PHOST were found to have a measurable amount of Si in the bulk when analyzed by d-SIMS, relative to the reactive PHOST films these detected amount were at much lower amounts. Similarly, the XPS data did not indicate the presence of Si in the bulk of any of the films besides the PHOST containing sample.

Concurrent efforts also were underway to analyze the self-assembly of PS-*b*-P(TBOS). As described in Chapter 2, phase-separation of BCPs on a preferential surface usually leads to the formation of island or hole features in the films which can be viewed by optical microscopy or atomic force microscopy (AFM). Additionally, in order for phase separation to occur the segregation strength, χN must be greater than or equal to 10.5. Before the synthesis of PS-*b*-P(TBOS) was undertaken, it was anticipated that a large molecular weight would need to be targeted in order to achieve the conditions that would lead to phase separation. The most efficient way to assess the BCP's ability to phase separate was done by spin-casting the BCPs on to silicon wafers which is presumably a preferential surface for the more polar block (assumed to be PS). This was followed by annealing and imaging to detect the presence of island/hole features. Despite several efforts, both BCPs did not produce island/hole features under any conditions tested such as using a range of film thicknesses, varying the annealing temperature/time, or spin-coating the BCPs onto modified surfaces.

Another way to analyze the ability of a BCP to phase separate is through a technique known as small angle x-ray scattering (SAXS), which also allows one to determine the bulk morphology exhibited by a phase separating BCP. In a typical SAXS experiment, x-rays are passed through a BCP sample which has been annealed above the T_g of both blocks. A diffraction pattern is collected from the x-rays which are scattered at very small angles. After mathematically transforming the data, the q-space or inverse domain space is found which can be plotted into a 2D pattern representing the scattering pattern.[89] For self-assembling BCPs there is usually a strong first-order q* peak with other higher-order peaks that follow. Using the distance between these peaks the morphology of the BCP can be inferred based on the scattering ratios q/q*. The scattering ratios and the correlated

morphologies are summarized in **Table 5.3**. Equally important, the pitch, L_0 also referred to as the domain spacing, d for lamellar BCPs can be calculated using the relationship, $d = 2\pi/q^*$.

Table 5.3: Peak positions (q/q*) of scattering patterns used to identified morphologies in BCPs.[89]

Morphology	Ratio q/q*
Lamellar	1, 2, 3, 4, 5, 6…
Cylindrical	1, $\sqrt{3}$, 2, $\sqrt{7}$, 3, $\sqrt{12}$…
Gyroid	1, $\sqrt{4/3}$, $\sqrt{7/3}$, $\sqrt{8/3}$, $\sqrt{10/3}$, $\sqrt{11/3}$…
Body-Centered Cubic	1, $\sqrt{2}$, $\sqrt{3}$, $\sqrt{4}$, $\sqrt{5}$, $\sqrt{6}$…
Face-Centered Cubic	1, $\sqrt{4/3}$, $\sqrt{8/3}$, $\sqrt{11/3}$, $\sqrt{12/3}$, $\sqrt{16/3}$…

The scattering data of the two samples of PS-*b*-P(TBOS) were collected and analyzed. The SAXS data is shown in **Figure 5.6**. The SAXS data in **Figure 5.6** does not feature any characteristic scattering peaks besides one low resolution scattering peak in each data set. This indicates poor contrast between the blocks and no phase separation, confirming the thin-film experiments performed.

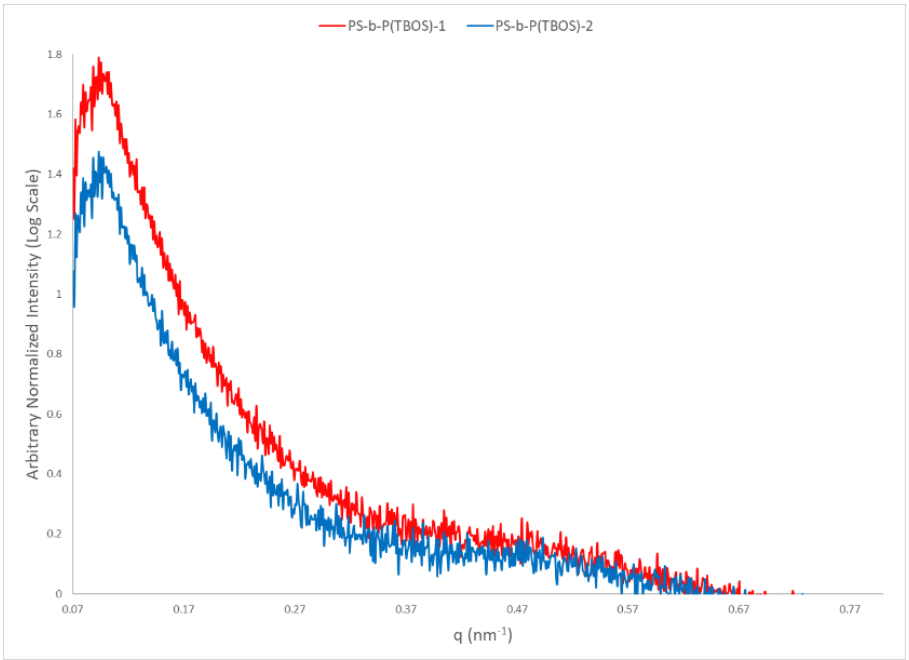

Figure 5.6: SAXS data measured for the two PS-*b*-P(TBOS) synthesized.

While the data collected for two PS-*b*-P(TBOS) BCPs did not suggest either polymer was capable of phase-separation, overall the synthesis and analysis of these polymers provided insight into designing the next BCP so that phase separation could occur. It was anticipated that the successor to PS-*b*-P(TBOS) would require incorporating a more polar block, relative to PS in order to increase the segregation strength between the blocks. Lastly, the selectivity analysis of DMSDMA to only the PHOST block provided encouraging evidence to continue pursuing this project in order to demonstrate the selectively in self-assembled materials.

5.3 POLY(4-METHOXYSTYRENE-*BLOCK*-4-TERT-BUTOXYSTYRENE)

Having concluded that the repulsive strength between the blocks in PS-*b*-P(TBOS) was not great enough to induce phase separation, the replacement of PS with an intuitively more polar block was pursued. While it is possible to synthesize phase-separating BCPs

based on non-aromatic monomers such as poly(methyl methacrylate) PMMA, for the purposes of this work only aromatic monomers based on styrene derivatives were considered largely due to their compatibility with anionic polymerization conditions and relative ease in availability/synthesis. Previously, poly(4-methoxystyrene), PMOST has been used successfully in the Willson group, particularly as a polar block component when compared to PS. Thus, in the 2nd iteration of P(TBOS)-containing BCPs, PMOST was chosen as the other block. The anionic polymerization of poly(4-methoxystyrene-*block*-4-*tert*-butoxystyrene), PMOST-*b*-P(TBOS) was carried out as shown in the reaction scheme in **Figure 5.6**.

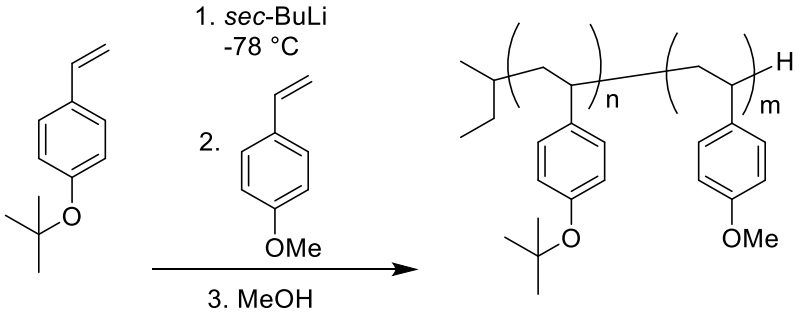

Figure 5.6: Reaction scheme for the anionic polymerization synthesis of PMOST-*b*-P(TBOS).

Two BCPs of differing molecular weights were targeted. However, even larger molecular weights were targeted in these syntheses to ensure phase separation, as it was unclear if the difference in surface energy between the two aromatic ether monomers was great enough to induce phase separation. The characterization data for the BCPs of different molecular weights is summarized in **Table 5.4**.

Table 5.4: Characterization data for the PMOST-*b*-P(TBOS) BCPs. Data was measured by SEC.

BCP	$M_{N,,B1}$ (Da)	$Đ_{B1}$	$M_{N,BCP}$ (Da)	$Đ_{BCP}$
PMOST-*b*-P(TBOS)-1	27,566	1.04	72,846	1.09
PMOST-*b*-P(TBOS)-2	52,548	1.09	104,747	1.08

It is beneficial to note that when beginning to evaluate a BCP, such as performing the island/hole test one must analyze a range of film thicknesses, particularly if the L_0 is unknown. This avoids making the premature conclusion at a single film thickness that there is no phase-separation, as that film thickness could be commensurate with the BCP's natural periodicity, giving a featureless film. When PMOST-*b*-P(TBOS)-1 and -2 were spin-cast onto a silicon wafer and thermally annealed at 180 °C for 10 min, I was encouraged to see the formation of island and hole features visible by optical microscopy. Having observed phase-separation in both BCPs, determining the L_0 of each BCP was required so that further analysis such as identifying a neutral substrate or interface are not complicated by commensurability issues in the film thickness.

As previously described, measuring the SAXS data of a BCP is one method to obtain a BCP's pitch. If a SAXS instrument is not readily accessible, another method that allows one to determine L_0 which takes advantage of the fact that under preferential wetting conditions (Chapter 2), the surface topography will "flip" in $0.5L_0$ intervals with both islands and holes being exhibited over a full nL_0 (n = 1, 2, 3…) film thickness range. Therefore, knowing the film thickness at which each change in topography is exhibited allows one to calculate the L_0 by taking the difference between the film thicknesses at two

commensurate conditions (e.g., $1.0L_0$, $1.5L_0$, $2.0L_0$, etc.) indicated by flat, features films. An example of this analysis is shown in **Figure 5.7** for PMOST-*b*-P(TBOS)-1.

Once the L_0 has been deduced, a scrupulous researcher seeking verification can also analyze the topographies imaged with AFM. Although there are some measured discrepancies between the value of L_0 measured by AFM versus SAXS, AFM is a convenient and efficient technique for an initial analysis especially if sample quantity is limited. However, the most thorough analysis would include data both SAXS and AFM data. To illustrate, two AFM micrographs of the same samples contained in **Figure 5.7** are featured in **Figure 5.8.** This is followed by the corresponding SAXS data in **Figure 5.9** for comparison.

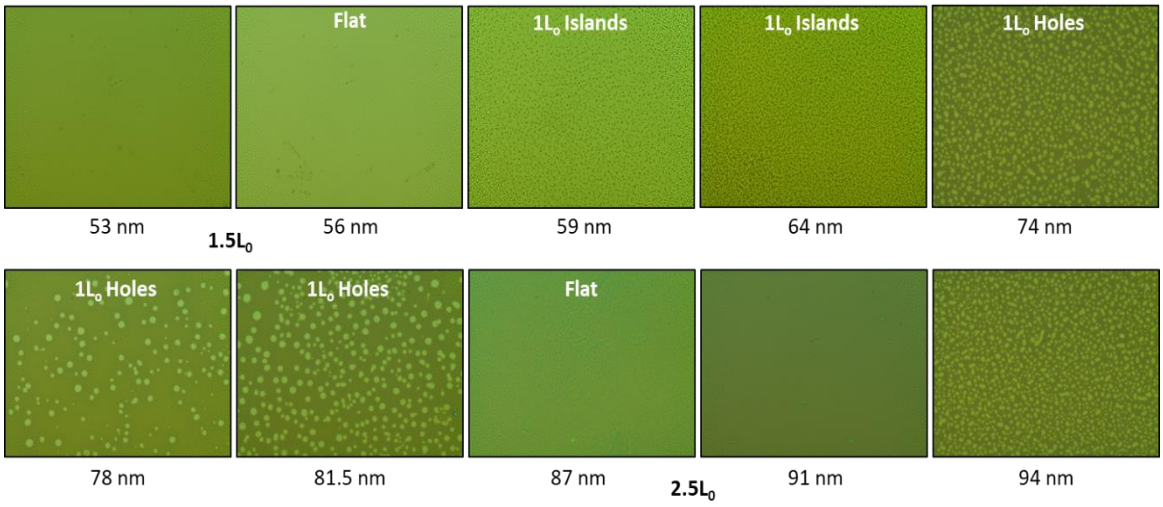

Figure 5.7: Optical microscope images of films of PMOST-b-P(TBOS)-1 on silicon wafers at various film thicknesses. Topography is labeled for clarity on some images.

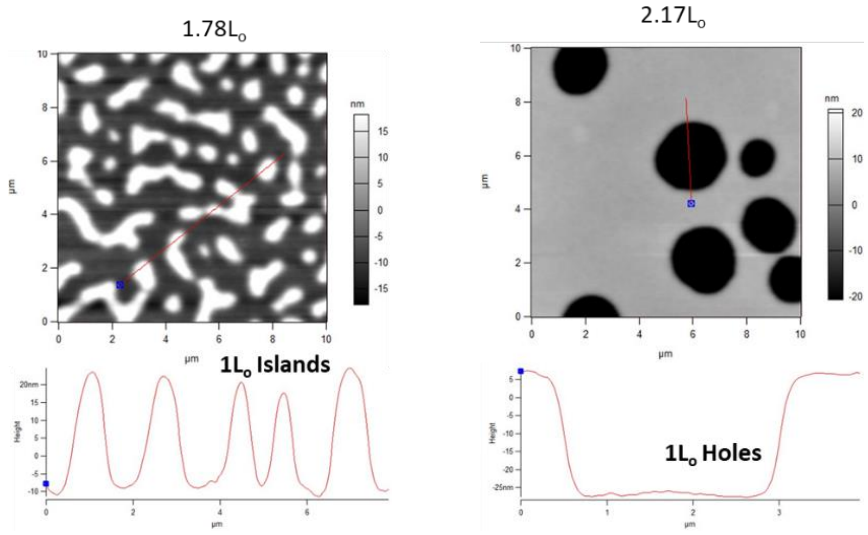

Figure 5.8: AFM micrographs of PMOST-*b*-P(TBOS)-1 on silicon wafers. The samples correspond to the 65 nm ($1.78L_0$) sample and the 78 nm ($2.17L_0$) sample from **Figure 5.7**.

Using the optical microscope images and the film thickness values, the difference between the film thicknesses at each commensurate condition observed indicates that the $L_0 \approx$ 34-36 nm. Upon inspection of the AFM micrographs, it can be seen graphically that the height or depth of the islands or holes measured is equivalent to ca. 36-37 nm in both samples which is in agreeance with the optical-microscopy pitch determination.

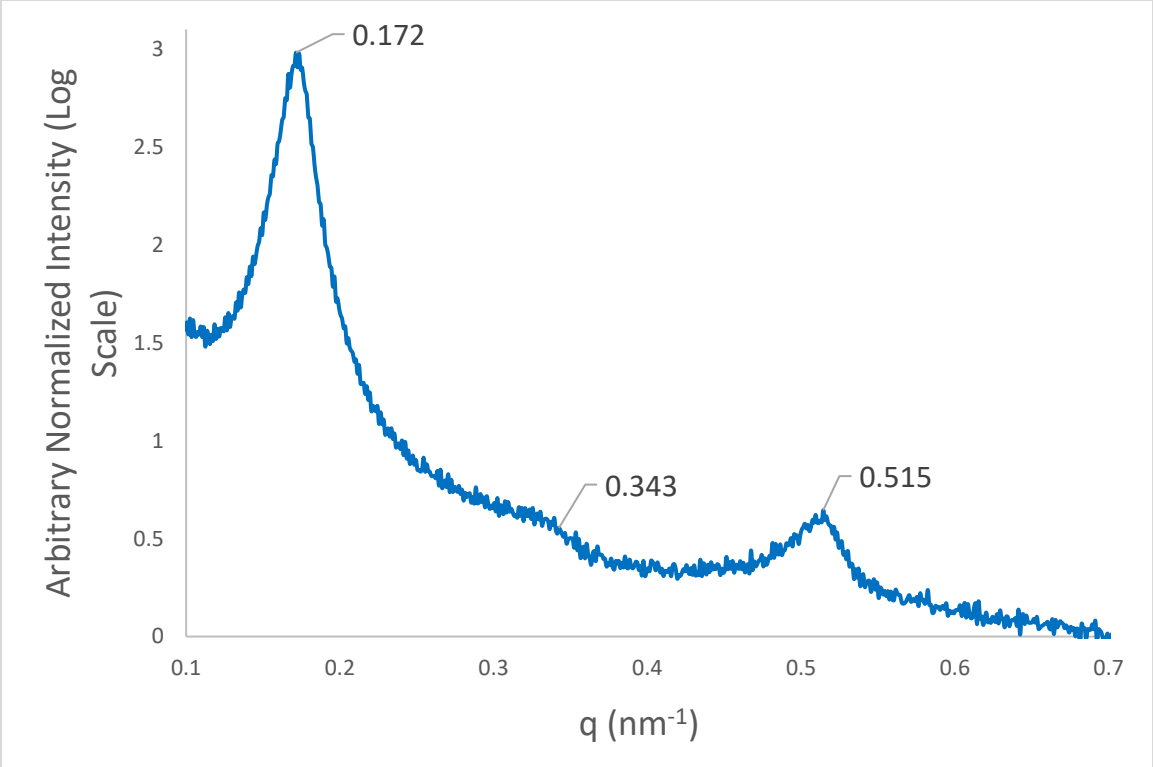

Figure 5.9: SAXS data measured for PMOST-b-P(TBOS)-1. The indicated values of q* were used to calculate L_0.

Similarly, using the values of q* from the SAXS data above and the relationship d = $2\pi/q^*$, the L_0=36 nm. It is satisfying that both methods used to determine L_0 are in agreeance. Additionally, the SAXS scattering pattern provides an indication of the BCP morphology. Based on the values of q/q* identified in Figure 5.9, the scattering pattern is characteristic of the lamellar morphology (Table 5.3) which was the desired morphology for this project. Although not shown here, the SAXS data was collected for PMOST-b-P(TBOS)-2 showing that L_0 = 49 nm and also followed a scattering pattern expected for the lamellar morphology. Having established the pitch of both BCPs, I began the analysis for identifying neutral surface and interface conditions for the BCPs, focusing mostly on PMOST-b-P(TBOS) with L_0=36 nm due to its smaller size.

Disappointingly, despite an exhaustive series of experiments neutral conditions could not be identified. Despite applying almost all of our group's library of XSTs the formation of 0.5L0 features, a diagnostic signal for a non-preferential interaction proved to be elusive. While a neutral surface is typically required alongside a neutral top-coat to induce perpendicular orientation of lamellae patterns, without a neutral substrate identified, it is still possible to identify a neutral top-coat material, acknowledging that the conditions would be carried out on a preferential surface (SiO_2) or one can reverse the order and anneal the BCP with a top-coat material on the bottom whereby the interface (air) becomes the preferential surface that is known or inferred. Following a lengthy pursuit at identifying a neutral interface, efforts to orientate this BCP were paused and it was concluded that such a narrow process window is not desirable for incorporating in the envisioned lithographic process. Once again, the design of a new BCP containing P(TBOS) was undertaken with hopes that "third times the charm!"

5.4 POLY(5-VINYL-1,3-BENZODIOXOLE-*BLOCK*-4-*TERT*-BUTOXYSTYRENE)

In the third iteration of BCPs containing a P(TBOS) block, the choice of monomer to constitute the other block domain was made so that the resultant BCP would feature a wider process window, in comparison to PMOST-*b*-P(TBOS). Thus, based on our group's results using poly(5-vinyl-1,3-benzodioxole), PVBD blocks in BCPs imparts a wide process window in terms of the flexibility in requiring a "perfectly-neutral surface" for perpendicular orientation to occur.[44] The anionic polymerization of PVBD-*b*-P(TBOS) was performed following the general procedure and is shown in **Figure 5.10**. The PVBD is not a commercially available monomer and therefore only one BCP was synthesized for this study. Following the sequence of steps established in this Chapter, the ability of this BCP to phase separate was assessed and confirmed by the formation of island and hole features

after annealing. The characterization data obtained for PVBD-*b*-P(TBOS) and the L_0 found by AFM analysis of island/hole features is summarized in **Table 5.5**.

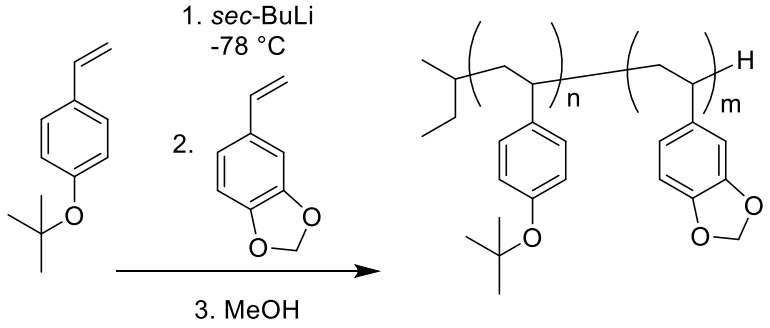

Figure 5.10: Anionic polymerization of PVBD-*b*-P(TBOS).

Table 5.5: Characterization data for PVBD-*b*-P(TBOS).

$M_{N,BCP}$ (Da)	$Đ_{BCP}$	L_0*
59,420	1.04	≈ 32 nm

*L_0 determined by AFM

Prior to evaluating the self-assembly of this BCP, we sought to confirm that this BCP was able to be deprotected using a PAG and would then incorporate DMSDMA and return to the as-cast film thickness. Additionally, we wanted to simulate the process steps which would be used in a typical self-assembly experiment. Therefore, after the films were spin-cast they were thermally annealed before the photoexposure and PEB step. Using a formulation of PVBD-*b*-P(TBOS) with 4 wt% (PAG/polymer), the BCP was spin-cast from PGME solutions onto a silicon wafer, thermally annealed at 180 °C for 10 min, exposed to 254 nm UV-light for 1 min, and baked at 100 °C for 1 min. Film thickness was

measured by ellipsometry and used to confirm that the P(TBOS) block was indeed deprotected to form blocks containing PHOST. The samples were then exposed to DMSDMA using the protocol established for the homopolymer samples (5.1). Satisfyingly, following exposure to the silylating agent the film thickness measured indicated that the BCPs incorporated the DMSDMA and returned to their as-cast thicknesses. These results have been summarized for two samples in **Table 5.6**.

Table 5.6: Film thickness data for PVBD-*b*-P(TBOS) samples silylated with DMSDMA. Film thickness was measured by ellipsometry.

As Cast FT (nm)	PHOST FT (nm)	Post-DMSDMA exposure FT (nm)
73	59	73
37	24	37

Further control experiments to evaluate the compatibility of the process flow from **Figure 5.1** with the materials were also performed. For instance, the compatibility of the process step involving the removal of the top coat after thermal annealing was evaluated. Top-coat removal is typically done by washing the film stacks with trimethylamine, TMA a volatile organic base which caused concern as it was anticipated that the BCP films would contain a PAG to be used in a subsequent process step. The results from this study were unexpected, as it was found that the BCP polymer was soluble to the stripping solutions (typically 1:1 TMA/methanol), resulting in a loss of all materials after subjected to the stripping conditions. Despite this finding, removal of a top-coat can be achieved through

other methods, most accessible is using reactive ion etching (RIE) with O_2 plasma to remove the top-coat material.

Initial efforts to identify a neutral surface treatment using a library of XSTs from the Willson group proved to be challenging. Over 20 XSTs along with12 polymeric brushes were evaluated. An eventual candidate was identified however, evidenced by formation of $0.5L_0$ features measured by AFM. Unfortunately, it was later discovered that the films were actually a mixture of $0.5L_0$ and $1.0L_0$ step-height features which is a thermodynamic phenomenon that has been reported by others.[90]

Despite the issues that arose with neutralizing the surface, a neutral top-coat was able to be identified as evidenced by $0.5L_0$ island/hole features measured in the AFM. The top-coat identified has the structure shown in **Figure 5.11** with the mole fractions (by feed ratio) of each monomer being the following: 0.55 maleic anhydride, 0.35 4-*tert*-butylstyrene, 0.10 styrene. This top coat is designated as AT1-189C, for reference.

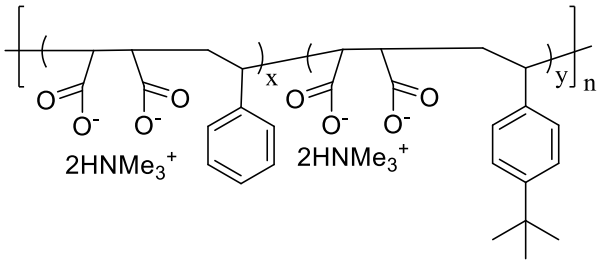

Figure 5.11: Chemical structure of the neutral top-coat identified for PVBD-b-P(TBOS).

In order to obtain a non-preferential surface for the PVBD-*b*-P(TBOS) BCP, we were lead to synthesize XSTs which incorporate the monomers of the BCP in order to more precisely match the surface energy. The XSTs developed were similar to those used by the Willson group for Si-BCPs, functioning by incorporating the cross-linkable 4-azidostyrene

(St-N_3) monomer. The chemical structure of the XSTs synthesized is shown in **Figure 5.12** and the composition of each XST (based on feed ratios) is contained in **Table 5.7**.

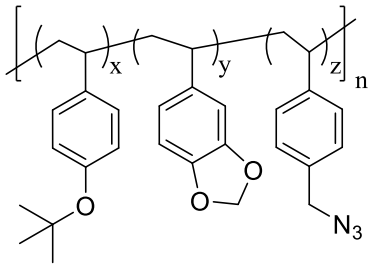

Figure 5.12: Chemical structure of the XSTs synthesized for PVBD-*b*-P(TBOS).

Table 5.7: Composition of XSTs. mol % values are based on feed ratios.

XST	mol % P(TBOS)	mol % PVBD	mol % St-N_3
ZM-2018-098	0.48	0.48	0.04
ZM-2018-099	0.26	0.71	0.04
ZM-2018-100	0.71	0.26	0.04

Upon annealing PVBD-*b*-P(TBOS) on each XST listed above, it was clear that ZM-2018-098 was not neutral indicated with full $1L_0$ features. In contrast, the features obtained when PVBD-*b*-P(TBOS) was annealed on ZM-2018-099 were less obvious and somewhat inconclusive. However, due to the lack in image contrast expected between the two organic blocks, it is not surprising that AFM does not provide a more detailed image to analyze. However, based on the shared wisdom of other Willson group members, XSTs or polymeric brushes which are slightly non-neutral but still produce $0.5L_0$ features are

oftentimes characterized by inconclusive images or topography. Thus, PVBD-*b*-P(TBOS) was confined between ZM-2018-099 on the bottom and AT1-189C at the surface. The film stack was annealed and the top coat was then removed by RIE with O_2 plasma. The AFM micrograph is shown in **Figure 5.13**.

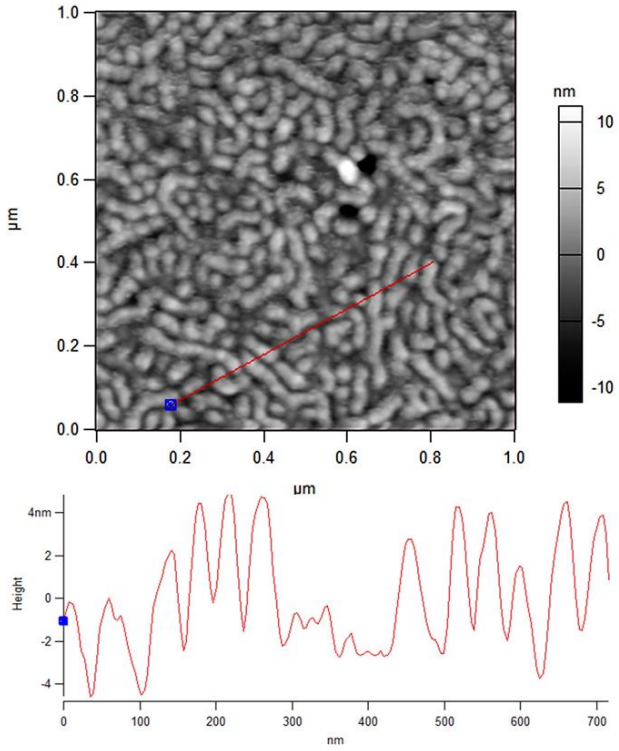

Figure 5.13: AFM micrograph of PVBD-*b*-P(TBOS) after thermally annealing between two surface thought to be neutral. The top-coat was removed by O_2 etching prior to imaging.

5.5 Summary and Project Outlook

Although it is unclear if the above image, **Figure 5.13** is indeed the perpendicularly aligned lamellae patterns of PVBD-*b*-P(TBOS) it seems that the path to eventually realize the overall goals of this project is clear. Although the original process appeared lengthy and complex, the overall impediment has been the self-assembly of the BCPs which contain a P(TBOS) block. Nevertheless, as the self-assembly was a continual challenge, it gave us the opportunity to learn a great deal about this class of BCPs and possibly guide the synthesis of derivative systems and certainly provide the foundation to see the project to the final etch-transfer step. We were able to provide compelling evidence that DMSDMA is selective for PHOST in the presence of other organic blocks. Furthermore, both PMOST-*b*-P(TBOS) and PVBD-*b*-P(TBOS) were found to adopt the lamellar morphology which departs from the limited number of reports which utilize BCPs containing P(TBOS) which are typically cylinder forming BCPs. Future work will continue pursuing the self-assembly of the PVBD-*b*-P(TBOS) in light of the encouraging preliminary results already obtained using the confinement conditions identified. Lastly, this work may also provide guidance to those interested in working with BCPs with low image contrast, shedding light on the difficulties associated with such a system but also inspiring a more diverse and interesting class of BCPs with functional organic monomers that will contribute to the tireless pursuit of progress and invention.

5.6 EXPERIMENTAL

5.6.1 Block-copolymer synthesis

BCPs were synthesized according to the following general procedure. The monomers were trap-to-trap distilled out of dibutyl-butyl magnesium twice and finally collected in an empty, flame dried Schlenk flask. A 500 mL glass reactor with 5 threaded ports was charged with a Teflon-coated magnetic stir bar and the following were attached to the ports: a thermocouple well, a septum-capped inlet port (attached to a Schlenk line and a pressure gauge), a 500 mL solvent flask of ~150g THF, and 2 glass blanks. The reactor was flame dried under high vacuum and purged five times with Ar. The purified THF was added to the reactor while maintaining a slight 3 psig overpressure. After cooling to – 78 °C, a solution of *sec*-butyllithium (1.4 M in cyclohexane, Aldrich) was added to the reactor through the septum via an air-tight syringe. The first monomer was then added, also by syringe, and allowed to react for 1 to 3 hours. An aliquot of approximately 3 mL was taken and injected into degassed methanol, before adding the second monomer by syringe. The reaction continued to be stirred for 1 to 3 hours and then terminated by addition of degassed methanol. The THF solution was concentrated slightly (target: 5 g THF / 1 g polymer) and precipitated into methanol. The isolated white powder was dried *in vacuo*.

5.6.2 XST Synthesis

The following procedure was used for ZM-2018-098 and is representative of all other XSTs described herein. 5-vinyl-1,3-benzodioxole, 4-*tert*-butoxystyrene, and 4-vinylbenzylchloride were stirred with basic alumina for 30 minutes and filtered prior to use. 5-vinyl-1,3-benzodioxole (0.60 g, 3.37 mmol, 0.48 eq), 4-*tert*-butoxystyrene (0.51 g, 3.37 mmol, 0.48 eq), vinylbenzylchloride (0.04 g, 0.28 mmol, 0.04 eq), and AIBN (0.01 g, 0.07 mmol, 0.01eq) were added to a 25 mL 3-neck round bottom flask equipped with a stir

bar, condenser, and three rubber septa. The reagents were dissolved in THF (8 ml) and the solution was deoxygenated by vigorously bubbling nitrogen through the solution for 30 minutes. The reaction vessel, under positive nitrogen pressure, was immersed in an oil bath at 65 ˚C. The reaction was heated and stirred for 12 h and quenched at 0 ˚C. The viscous liquid was dissolved in an additional 10 ml THF and precipitated into methanol (150 ml) and filtered. The polymer was dissolved in 10 ml of THF and reprecipitated into methanol one additional times. The polymer was dried *in vacuo* overnight to yield 0.86 g of dry polymer. The polymer (0.78 g) was placed in a 25 ml round bottom flask and dissolved in 13 ml of DMF. Sodium azide (0.23 g, 33 wt% with respect to the polymer) was added to the flask and the reaction was heated to 60 ˚C for 12 hours. The reaction was cooled to room temperature. The cloudy suspension was filtered and the polymer was precipitated into methanol (3x). Drying the polymer overnight *in vacuo* 0.75 g of ZM-2018-098. The broad benzyl position resonance in the 1H NMR completely shifted from ~4.5 (VBzCl) to ~4.3 (VBzAz).

5.6.3 Characterization

SEC was performed using a Viscotek VE 2001 triple detector gel permeation chromatograph with an Agilent 1100 Series isopump and autosampler. THF was used as an eluent at 1 mL/min and 23 °C with three I-series mixed bed high-MW columns, calibrated against PS standards.

SAXS measurements were made at Cornell University for PS-*b*-P(TBOS) and PMOST-*b*-P(TBOS). SAXS measurements of PVBD-*b*-P(TBOS) were made at University of Minnesota. Samples were prepared by annealing polymer inside of a Viton o-ring in between Kapton tape on a hotplate.

AFM scans were obtained using an Asylum MFP-3D Origin operating in tapping mode. A Brewer CEE 100CB Spincoater was used to coat all thin films. Ellipsometry was performed with a J.A. Woollam Co, Inc. VB 400 VASE Ellipsometer with wavelengths from 382 to 984 nm and a 65° angle of incidence.

Chapter 6: A Cyclic (Alkyl)(Amido)Carbene: Synthesis, Study and Utility as a Desulfurization Reagent

6.1 Background statement regarding this work

Prior to joining the Willson group, I was a member of the former Bielawski group at UT-Austin. During that 1.5 years my research focused on a different aspect of functional organic molecules which was developing electrophilic amid-decorated carbenes that could participate in or facilitate reactions typically reserved for transition metal species. The other author on the paper, Dominicka Lastovickova contributed towards the X-ray diffraction data collection and analyses. Otherwise, all of the experimentation and synthetic were done by myself. The following has been reproduced from McCarty, Z. R.; Lastovickova, D, N.; Bielawski, C. W. *Chem. Commun.*, **2016**, *52*, 5447-5450.

6.2 Electrophilic carbenes as functional organic materials

While the chemistry of the *N*-heterocyclic carbenes (NHCs) continues to expand,[91,92] relatively less efforts have been directed towards the study of carbenes which are structurally, electronically and chemically distinct from the diaminocarbene archetype.[93] For example, our group[94–98] and others[99–108] have shown that the incorporation of carbonyl groups into the heterocyclic scaffolds of various NHCs strongly influences the electronic properties of the resultant compounds. In particular, when compared to their nucleophilic NHC analogues (*e.g.*, I, **Figure 6.1**), the *N,N'*-diamidocarbenes (DACs; *e.g.*, II) were found to be more electrophilic and engaged in reactions more commonly associated with transient, electrophilic carbenes, including inter- and intramolecular C–H insertions,[98,109] the reversible fixation of carbon monoxide,[94,95] and a range of cycloaddition reactions.[110,111]

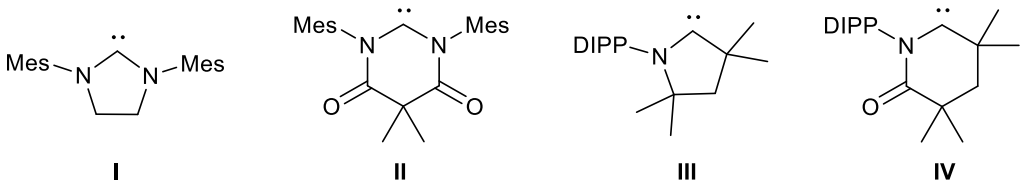

Figure 6.1: Structures of various carbenes. DIPP = 2,6-di-iso-propylphenyl, Mes = 2,4,6-trimethylphenyl

As disclosed by Bertrand and co-workers, the cyclic (alkyl)(amino)carbenes (CAACs; *e.g.*, **III**) also display pronounced electrophilic characteristics, which is believed to stem from the relatively small singlet-triplet gap of the corresponding carbene nucleus; a consequence of the amino group bonded to the carbene nucleus.[112–116] Building on this knowledge, we postulated that a carbene linked to an amide moiety and a σ-donating alkyl group should display an unsurpassed degree of electrophilicity,‡ and thus potentially expand the range of carbene-facilitated transformations. Herein, we report the synthesis and study of a cyclic (alkyl)(amido)carbene (IV).

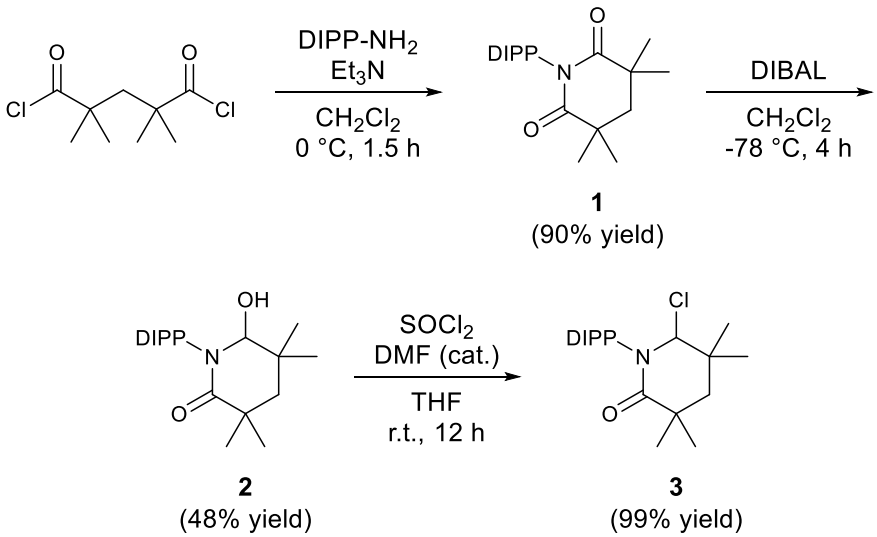

Figure 6.2: Synthesis of the cyclic (alkyl)(amido)carbene precursor 3.

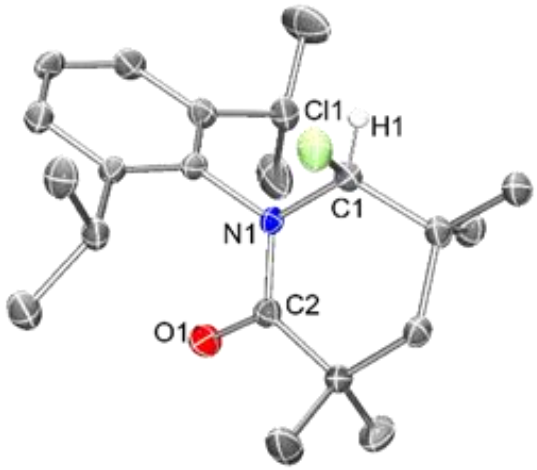

Figure 6.3: POV-ray representation of 3 with the thermal ellipsoids set at 50% probability and most of the H-atoms omitted for clarity. Selected bond lengths (Å) and angles (˚): C1–Cl1, 1.850(3); C1–N1, 1.442(4); C2–O1, 1.223(4); C2–N1–C1, 124.0(2); N1–C1–Cl1, 109.95(19), O1–C2–N1, 119.2(3).

As summarized in **Figure 6.2**, condensation of 2,2,4,4-tetramethylglutaryl dichloride[117] and 2,6-di-*iso*-propylaniline in the presence of triethylamine / CH_2Cl_2

afforded the tetramethylpiperidine-2,6-dione **1** in 90% yield after purification. Subsequent treatment of **1** with 1.5 equivalents of di-*iso*-butylaluminum hydride (DIBAL) afforded the mono-reduced alcohol **2** in 48% yield after purification. Finally, the desired precursor **3** was obtained in high yield via the treatment of **2** with thionyl chloride ($SOCl_2$) following purification. Single crystals suitable for a single crystal X-ray diffraction (XRD) analysis were obtained by cooling a hexanes solution saturated with **3** to -30 °C (**Figure 6.3**). The C(1)–Cl(1) bond distance of **3** (1.850(3) Å) was found to be relatively elongated when compared to a typical sp^3 C–Cl bond (1.76 Å),[118] and similar to the analogous bond length measured in the solid state structure of the HCl precursor of **II** (1.888(2) Å).[95]

With **3** in hand, subsequent efforts were directed toward the generation of the corresponding cyclic (alkyl)(amido)carbene. Treating **3** with 1.2 equivalents of sodium hexamethyldisilazide (NaHMDS) at ambient temperature immediately resulted in the formation of the C–H insertion product **5**, as determined by ^{1}H NMR spectroscopy (C_6D_6). In particular, the appearance of a septet (3.58 ppm) and a singlet (3.42 ppm) were consistent with the methine groups of the corresponding bicyclic product. Similar results were obtained when the deprotonation reaction was performed at 0 °C, as determined using ^{1}H NMR spectroscopy. The structure of **5** was unambiguously confirmed using a single crystal XRD analysis of colorless crystals of **5**, which were grown by slowly evaporating a diethyl ether/pentane (1:1 v/v) solution saturated with the compound (**Figure 6.5**). The propensity of **4** to readily undergo C–H insertion is unique when compared to the intra- and intermolecular C-H insertion reactions previously reported for the DACs, as such transformations typically require elevated temperatures (50-120 °C) as well as relatively long periods of time.[95,109]

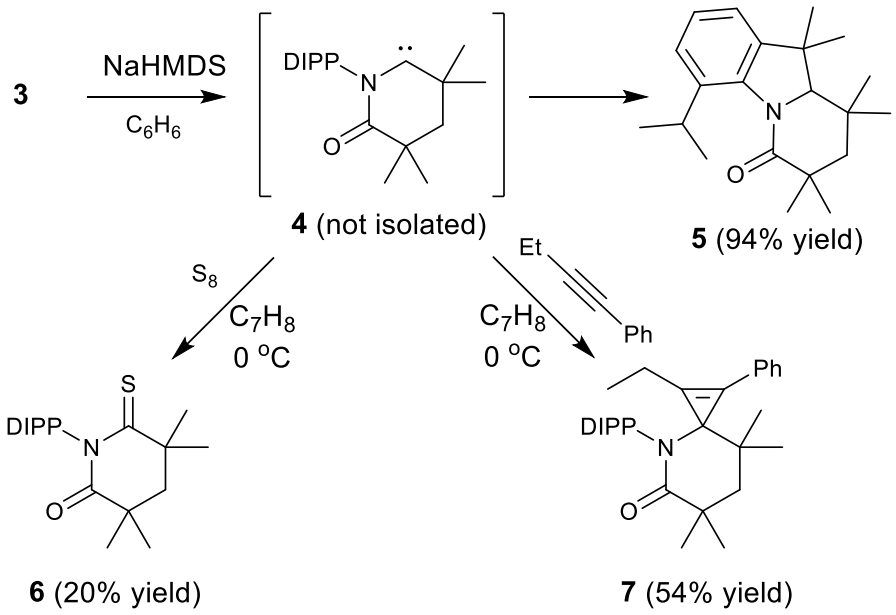

Figure 6.4: Generation of and reactivity displayed by **4**.

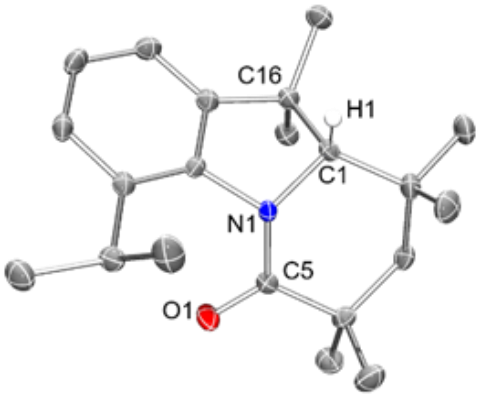

Figure 6.5: POV-ray representation of **5** with the thermal ellipsoids set at 50% probability and most of the H-atoms omitted for clarity. Selected bond lengths (Å) and angles (˚): C1–N1, 1.4964(17); C1–C16, 1.5666(19); C2–N1, 1.3775(18); C2–O1, 1.2222(17); N1–C1–C16, 101.95(10); C1–N1–C2, 123.82(11); O1–C2–N1, 121.16(12).

Despite its high affinity to undergo intramolecular C–H insertion, the generation of the free carbene 4 was corroborated via a series of trapping experiments. For example, generating the carbene 4 in the presence of S8 afforded the corresponding thione 6. Notably, the 13C NMR resonance assigned to the C=S bond (219.02 ppm, CDCl3; 220.08 ppm, THF-d8) of 6 was found to be significantly downfield when compared to those recorded for the analogous five- (177.96 ppm; $CDCl_3$)[103] and six (177.4 ppm; $CDCl_3$)[101] membered DAC-sulfur adducts, but similar to the sulfur adduct of **III** (213.6 ppm; THF-d_8).[119] Moreover, the treatment of *in situ* generated **4** with 1-phenyl-1-butyne at 0 °C afforded the cyclopropene adduct **7** in 54% yield. The structure of **7** was further supported by a single crystal XRD analysis of single crystals of **7** grown by slowly evaporating a saturated pentane/diethyl ether solution (1:1 v/v) (**Figure 6.6**). While other electron deficient carbenes, such as **III**, have been shown to split hydrogen,[114] deprotonating **3** under an atmosphere of H_2 afforded **5** as the main product, even at elevated temperatures.

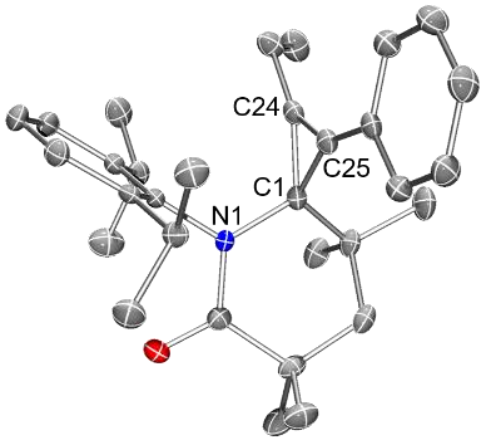

Figure 6.6: POV-ray representation of 7 with thermal ellipsoids set at 50% probability and the H-atoms omitted for clarity. Selected bond lengths (Å) and angles (˚): C1–N1, 1.491(2); C1–C24, 1.497(2); C1–C25, 1.501(2); C24–C25, 1.302(2); C24–C1–C25, 51.48(11); C24–C25–C1, 64.10(12); C25–C24–C1, 64.43(12).

As it is well known that NHCs form stable zwitterionic adducts with electrophilic heteroallenes, such as carbon disulfide (CS_2), we sought to utilize this benchmark reaction to probe the intrinsic nucleophilicity of **4**.[120] To our surprise, treatment of **4** with a slight excess CS_2 (3 equiv.) did not afford the expected zwitterionic adduct; rather, the two major products isolated were identified as the thione 6 and the thiol 8 (**Figure 6.7**). Due to the substantial presence of insoluble precipitates observed in the reaction mixture, we believe that 4 desulfurized CS_2 and produced highly reactive carbon monosulfide which is known to spontaneously polymerize upon formation.[121] As part of a series of control reactions, no reaction was observed between 3 and CS2 in the absence of base. Likewise, performing a similar reaction with 0.5 equiv. of NaHMDS with respect to **3** resulted in the same molar ratio of products **6** and **8**. Collectively, these observations indicated that the free carbene **4** facilitated the desulfurization process.

Building on aforementioned results, we explored the ability of **4** to desulfurize carbonyl sulfide (COS), a reagent which has also been shown to form zwitterionic adducts with NHCs.[122] When **4** was generated under an atmosphere of COS, the thiol **8** was isolated in 57% yield (**Figure 6.7**). The reaction with COS likely favors the release of the more stable CO gas over CS, as products with increased oxygen content (*e.g.*, **1** or **2**) were not observed. Although similar transformations were reported by Berry et al.[123] using a Zr complex, to the best of our knowledge these are the first examples of carbene-facilitated desulfurizations and reveal the potential of 4 to serve as an organic alternative to metal-mediated processes.

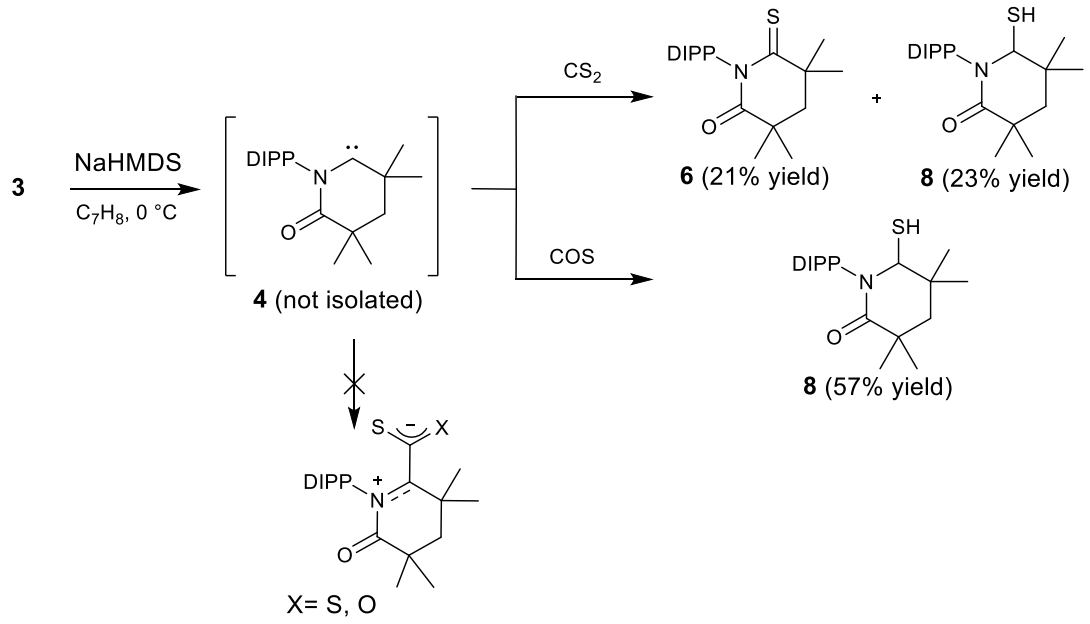

Figure 6.7: Carbene facilitated desulfurizations. Yields shown are based on the molar quantity of **3** used.

To gain additional insight into the unique reactivity displayed by **4,** its σ-donor and π-acceptor abilities were quantified by synthesizing and analyzing various organometallic adducts (**Figure 6.8**). Treating the *in situ* generated **4** with $[Ir(COD)Cl]_2$ (COD = 1,5-cyclooctadiene) afforded the Ir complex [(**4**)Ir(COD)Cl] (**9**). The ^{13}C NMR resonance of the carbene nucleus in **9** was recorded at 287.6 ppm ($CDCl_3$). To the best of our knowledge, this is the most deshielded signal to be reported amongst the analogous carbene-supported Rh or Ir carbene complexes,[124–127] including that of the Rh complex of an acyclic variant of **III** (279.5 ppm, $CDCl_3$).[128] A single crystal XRD analysis of orange crystals of **9** grown via the slow evaporation of a saturated heptanes solution confirmed the structure of the complex (**Figure 6.9**).

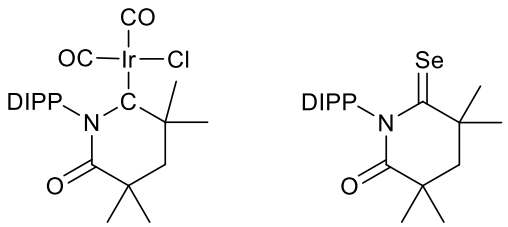

10 **11**

Figure 6.8: Structures of complexes used to evaluate the electronic properties of **4**.

The *σ*-donor ability of **4** was determined from the Ir dicarbonyl complex **10**, which was prepared by sparging a CH_2Cl_2 solution of **9** with carbon monoxide. The corresponding product exhibited a downfield ^{13}C NMR resonance at 280.6 ppm ($CDCl_3$), which was assigned to the carbene nucleus, and supported its electron deficient nature. The infrared spectrum of **10** exhibited two prominent ν_{CO} absorptions at 2068 and 1986 cm^{-1} (KBr, CH_2Cl_2) which, using Nolan's method,[124] translated into a Tolman Electronic Parameter (TEP) of 2053 cm^{-1}, a value similar to that calculated for SIMes **I** (2052 cm^{-1}).[124–127] Based on the reactivity observed for **4,** this result was surprising and indicated that the carbene is a relatively strong *σ*-donor when used as a ligand.

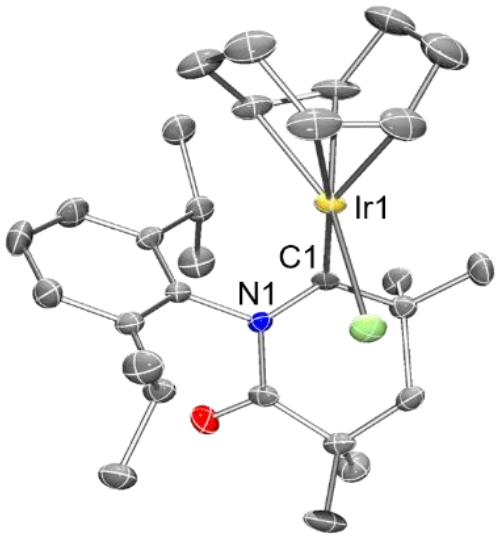

Figure 6.9: POV-ray representation of 9 with thermal ellipsoids set at 50% probability and the H-atoms omitted for clarity. Selected bond lengths (Å) and angles (°): C1–Ir1, 1.944(5); C1–N1, 1.354(6); N1–C1–Ir1, 126.2(3).

While the TEP value provides a useful correlation for assessing the donor ability of carbenes, several new methods have been established to provide information on the corresponding π-accepting abilities.[129] One valuable method entails an ^{77}Se NMR analysis of the corresponding carbene-selenium adduct followed by comparison to other adducts.[130] Treatment of **4** (generated *in situ*) with elemental selenium at ambient temperature afforded **11** in 55% yield. In addition to the ^{13}C NMR resonance assigned to the carbene nucleus nucleus observed at 228.01 ppm ($CDCl_3$), a ^{77}Se NMR signal was recorded at 1179.71 ppm (acetone-d_6). When compared to the series of carbene-selenium adducts evaluated by Ganter and co-workers, the ^{77}Se NMR resonance displayed by **11** represents the most downfield signal reported to date and reflects the strong π-accepting ability of **4**, surpassing even the five- and six- membered DACs (^{77}Se NMR: δ 856 and 847 ppm, respectively).[130,131]

In conclusion, we disclose the synthesis and study of a cyclic (alkyl)(amido)carbene. The corresponding precursor **3** was synthesized in three steps and in good overall yield. Unlike traditional NHCs, **4** displayed a significant degree of electrophilicity as evidenced by an ability to undergo C–H insertion at low temperature and to cyclopropenate alkynes. The observed reactivity profile was supported by ^{77}Se NMR spectroscopy which indicated that **4** is the most strongly π-accepting carbene reported to date while its TEP value indicated that a relatively high degree of σ-donating ability is retained. The discovery of a carbene to function as a desulfurization reagent is expected to catalyze further investigations into the unique transformations facilitated by electrophilic carbenes, particularly as metal-free alternatives in synthetic processes.

6.3 EXPERIMENTAL

6.3.1: General Considerations

All procedures were performed using standard Schlenk techniques under an atmosphere of nitrogen or in a nitrogen filled glove box unless otherwise noted. All compounds, except for **3**, were found to be air stable and all chromatographic separations were performed under ambient conditions. The compound 2,2,4,4-tetramethylglutaryl dichloride was prepared according to a literature procedure.[132] Carbonyl sulfide was purchased from Sigma Aldrich and passed through a drying tube packed with 3 Å molecular sieves to remove the residual moisture prior to use. Solvents were dried and degassed using a Vacuum Atmospheres Company solvent purification system and stored over 4 Å molecular sieves in a nitrogen filled glove box. Infrared (IR) spectra were recorded on a Thermo Scientific Nicolet iS5 spectrometer equipped with an iD3 attenuated total reflectance (ATR) attachment (diamond crystal) or using CaF_2 or KBr solution cells. High resolution mass spectra (HRMS) were obtained with a Waters Micromass Autospec-Ultima (CI) or Agilent 6530 QTOF (ESI) mass spectrometer. NMR spectra were recorded on a Varian 400, 500, or 600 MHz spectrometer. Chemical shifts (δ) are reported in ppm and are referenced to the residual solvent (^{1}H: THF-d_8, 1.72 ppm; $CDCl_3$, 7.26 ppm; C_6D_6, 7.15 ppm, C_7D_8, 2.08 ppm; ^{13}C: THF-d_8, 67.21 ppm; $CDCl_3$, 77.0 ppm, C_6D_6, 128.0 ppm). The ^{77}Se NMR data were referenced to an external 60% (v/v) Me_2Se standard in $CDCl_3$ set at δ 0.0 ppm. Elemental analyses were performed with a Thermo Scientific Flash 2000 Organic Elemental Analyzer. Melting points were measured using a Stanford Research Systems MPA100 OptiMelt automated melting point apparatus and are uncorrected.

6.3.2 Synthesis and characterization

1-(2,6-diisopropylphenyl)-3,3,5,5-tetramethylpiperidine-2,6-dione (1). The compound 2,6-di-*iso*-propyl aniline (1.81 mL, 9.59 mmol, 1 eq) was added to a stirred solution of 2,2,4,4-tetramethylglutaryl dichloride (2.16 g, 9.59 mmol) and triethylamine (4.01 mL, 28.75 mmol, 3 eq) in CH_2Cl_2 (10 mL). The resultant solution was stirred for 1.5 h at ambient temperature and then heated at 40 °C for 1 h. The volatiles were then removed under reduced pressure and the residue was washed with a mixture of hexanes/CH_2Cl_2 (2:1 v:v) (60 mL). The filtrate was collected and concentrated under reduced pressure. Purification via column chromatography (2:1 v/v CH_2Cl_2/hexanes, SiO_2) afforded the desired compound as a white solid (2.82 g, 8.56 mmol, 90% yield). m.p. = 141-143 °C. ^{1}H NMR ($CDCl_3$, 399.68 MHz): δ 1.13 (d, J = 7.05 Hz, 12H), 1.43 (s, 12H), 1.96 (s, 2H), 2.59 (sept., J = 7.1 Hz, 2H), 7.20 (d, J = 7.8 Hz, 2H), 7.36 (t, J = 7.8 Hz, 1H). ^{13}C NMR ($CDCl_3$, 100.50 MHz): δ 23.72, 28.62, 39.30, 45.59, 123.66, 128.96, 131.38, 145.28, 177.95. IR (ATR): $\nu_{C=O}$ = 1723, 1679 cm^{-1}. HRMS (CI): $[M+H]^+$ calcd for $C_{21}H_{32}NO_2$: 330.2433; Found: 330.2433. Anal. Calcd for $C_{21}H_{31}NO_2$: C, 76.55; H, 9.48; N, 4.25. Found: C, 76.88; H, 9.42; N, 4.30.

1-(2,6-diisopropylphenyl)-6-hydroxy-3,3,5,5-tetramethylpiperidin-2-one (2). To a stirred solution of **1** (1.27 g, 3.85 mmol) in CH_2Cl_2 (10 mL), DIBAL-H (1.0 M in hexanes, 5.8 mL, 1.5 eq, 5.8 mmol) was added dropwise over the course of 10 min at -78 °C. The resultant solution was stirred at this temperature for 4 h, after which time H_2O (5.8 mL) was carefully added followed by 2 M aqueous NaOH (1.7 mL). After warming to room temperature, the mixture was poured into a saturated solution of Rochelle's salt (35 mL) and extracted with CH_2Cl_2 (5 × 20 mL). The combined organic layers were then

washed with H_2O, followed by brine, and subsequently dried with Na_2SO_4. Removal of the volatiles under reduced pressure afforded a crude white solid, which was purified via column chromatography (2:1 CH_2Cl_2/hexanes then CH_2Cl_2, SiO_2) to afford the desired compound as a white solid (0.61 g, 1.84 mmol, 48% yield). m.p. = 240-242 °C. ^{1}H NMR ($CDCl_3$, 399.68 MHz): δ 1.09-1.14 (m, 9H), 1.22 (d, J = 6.7 Hz, 3H), 1.25 (d, J = 7.0 Hz, 3H), 1.29 (s, 3H), 1.34 (s, 3H), 1.37 (s, 3H), 1.58 (d, J = 1.2 Hz, 1H), 2.14 (d, J = 14.1 Hz, 1H), 2.27 (d, J = 4.3 Hz, 1H), 3.03 (sept., J = 7.0 Hz, 1H), 3.17 (sept., J = 7.0 Hz, 1H), 4.56 (dd, J_1 = 1.18 Hz, J_2 = 4.3 Hz, 1H), 7.18-7.20 (m, 2H), 7.32 (t, J = 7.4 Hz, 1H). ^{13}C NMR ($CDCl_3$, 100.50 MHz): δ 23.34, 23.89, 24.25, 24.89, 25.62, 26.64, 28.09, 28.42, 30.09, 31.61, 35.08, 38.07, 44.23, 89.96, 124.22, 124.30, 128.53, 135.53, 145.80, 148.45, 176.26. IR (ATR): ν_{O-H} = 3383cm^{-1}; $\nu_{C=O}$ = 1618 cm^{-1}. HRMS (CI): $[M+H]^+$ calcd for $C_{21}H_{34}NO_2$: 332.2590; Found: 332.2589. Anal. Calcd for $C_{21}H_{33}NO_2$: C, 76.09; H, 10.03; N, 4.23. Found: C, 76.03; H, 10.05; N, 4.19.

6-chloro-1-(2,6-diisopropylphenyl)-3,3,5,5-tetramethylpiperidin-2-one (3). To a Schlenk flask containing **2** (1.05 g, 3.17 mmol) and DMF (3 drops) in THF (10 mL), thionyl chloride (0.69 mL, 3 eq, 9.50 mmol) was added with stirring at ambient temperature. The resultant solution was stirred under an inert atmosphere for 12 h, after which the volatiles were removed under reduced pressure to afford the desired compound as an off-white solid (1.10 g, 3.14 mmol, 99% yield). Cooling a saturated solution of **3** in hexanes to -30 °C in a glove box freezer afforded colorless single crystals suitable for a single crystal X-ray diffraction analysis. m.p. = 186-189 °C (dec.). ^{1}H NMR (C_6D_6, 399.68 MHz): δ 0.94 (s, 3H), 1.08 (d, J = 7.0 Hz, 3H), 1.12 (d, J = 7.0 Hz, 3H), 1.14-1.19 (m, 4H), 1.30 (s overlapping d, J = 6.7 Hz, 6H), 1.44 (s overlapping d, J = 6.7 Hz, 6H), 2.29 (d, J =

14.1 Hz, 1H), 3.01 (sept., J = 7.0 Hz, 1H), 3.31 (sept., J = 7.0 Hz, 1H), 5.42 (d, J = 2.4 Hz, 1H), 7.07 (dd, J_1 = 1.9 Hz, J_2 = 7.0, 1H), 7.17-7.24 (m, 2H). ^{13}C NMR (C_6D_6, 100.50 MHz): δ 22.63, 23.58, 24.00, 25.33, 26.23, 27.96, 29.18, 29.25, 29.98, 32.24, 36.97, 38.42, 43.74, 90.74, 124.33, 125.11, 129.14, 136.69, 145.21, 148.23, 175.38. IR (CH_2Cl_2, CaF_2): $\nu_{C=O}$ = 1666 cm^{-1}. HRMS (CI): $[M+H]^+$ calcd for $C_{21}H_{33}ClNO$: 350.2251; Found: 350.2244. Anal. Calcd for $C_{21}H_{32}ClNO$: C, 72.08; H, 9.22; N, 4.00. Found: C, 71.67; H, 9.11; N, 3.81.

4-isopropyl-7,7,9,9,10,10-hexamethyl-8,9,9a,10-tetrahydropyrido[1,2-a]indol-6(7H)-one (5). A vial was charged with **3** (75 mg, 0.21 mmol), NaHMDS (47 mg, 0.26 mmol, 1.2 eq), benzene (5 mL), and a stir bar. After stirring at ambient temperature for 1 h, the mixture was passed through a PTFE filter and the remaining volatiles were removed under reduced pressure. Purification via column chromatography (2:1 CH_2Cl_2/hexanes, SiO_2) afforded the desired compound as a colorless crystalline compound (63 mg, 0.20 mmol, 94% yield). Slow evaporation of a saturated solution of diethyl ether/n-pentane (1:1 v/v) afforded colorless single crystals suitable for a single crystal X-ray diffraction analysis. m.p. = 91-92 °C. ^{1}H NMR (C_6D_6, 399.68 MHz): δ 0.91 (d, J = 8.2 Hz, 6H), 0.95 (s, 3H), 1.13 (s, 3H), 1.18 (d, J = 7.0 Hz, 3H), 1.36 (d overlapping d, J = 6.7 Hz, 8H), 1.64 (d, J = 6.7 Hz, 3H), 3.42 (s, 1H), 3.58 (sept., J = 7.0 Hz, 1H), 6.78 (dd, J_1 = 1.2 Hz, J_2 = 7.4 Hz, 1H), 7.09 (t, J = 7.4 Hz, 1H), 7.19 (dd, J_1 = 1.2 Hz, J_2 = 7.8 Hz, 1H). ^{13}C NMR (C_6D_6, 100.50 MHz): δ 22.64, 24.61, 24.96, 25.46, 27.25, 28.48, 29.69, 30.67, 31.83, 34.08, 39.49, 45.88, 52.18, 81.03, 118.69, 125.45, 126.04, 139.53, 139.69, 144.39, 176.78. IR (ATR): $\nu_{C=O}$ = 1651 cm^{-1}. HRMS (CI): $[M]^+$ calcd for $C_{21}H_{31}NO$: 313.2405; Found: 313.2406. Anal. Calcd for $C_{21}H_{31}NO$: C, 80.46; H, 9.97; N, 4.47. Found: C, 80.69; H, 9.84; N, 4.46.

1-(2,6-diisopropylphenyl)-3,3,5,5-tetramethyl-6-thioxopiperidin-2-one (6). A stirred solution of **3** (100 mg, 0.29 mmol) and S_8 (18 mg, 0.56 mmol, 2 eq) in toluene (8 mL) was cooled to 0 °C. To the colorless solution, NaHMDS (63 mg, 0.34 mmol, 1.2 eq) in toluene (1 mL) was added dropwise which immediately resulted in the formation of a bright yellow color. Stirring was continued at this temperature for 1 h, after which time the volatiles were removed under reduced pressure and the residue was purified by flash chromatography (1:1 v/v CH_2Cl_2/hexane, SiO_2) to yield the desired compound as a bright yellow, crystalline solid (20 mg, 0.06 mmol, 20% yield). m.p. = 133-135 °C. ^{1}H NMR ($CDCl_3$, 400.09 MHz): δ 1.09 (d, *J* = 6.7 Hz, 6H), 1.14 (d, *J* = 6.7 Hz, 6H), 1.46 (s, 6H), 1.56 (s, 6H), 2.04 (s, 2H), 2.55 (sept., *J* = 6.7 Hz, 2H), 7.21 (d, *J* = 7.8 Hz, 2H), 7.38 (t, *J* = 7.8 Hz, 1H). ^{1}H NMR (THF-d_8, 399.77 MHz): δ 1.05 (d, *J* = 6.7 Hz, 6H), 1.10 (d, *J* = 6.7 Hz, 6H), 1.41 (s, 6H), 1.53 (s, 6H), 2.07 (s, 2H), 2.59 (sept., *J* = 6.7 Hz, 2H), 7.14 (d, *J* = 7.4 Hz, 2H), 7.26 (t, *J* = 7.4, 1H). ^{13}C NMR ($CDCl_3$, 100.60 MHz): δ 23.88, 24.07, 28.55, 29.15, 32.81, 39.47, 45.41, 46.05, 124.08, 128.97, 136.21, 144.59, 175.86, 219.02. ^{13}C NMR (THF-d_8, 100.52 MHz): δ 24.13, 24.44, 29.25, 29.33, 33.27, 40.15, 46.14, 46.38, 124.51, 129.24, 137.56, 145.51, 176.26, 220.08. IR (ATR): $\nu_{C=O}$ = 1713 cm^{-1}, $\nu_{C=S}$ = 1193 cm^{-1}. HRMS (CI): $[M+H]^+$ calcd for $C_{21}H_{32}NOS$: 346.2205; Found: 346.2211. Anal. Calcd for $C_{21}H_{31}NOS$: C, 73.00; H, 9.04; N, 4.05; S, 9.28. Found: C, 72.88; H, 8.83; N, 4.27; S, 9.23.

4-(2,6-diisopropylphenyl)-1-ethyl-6,6,8,8-tetramethyl-2-phenyl-4-azaspiro[2.5]oct-1-en-5-one (7). A 10 mL Schlenk flask was charged with **3** (75 mg, 0.21 mmol), 1-phenyl-1-butyne (0.11 g, 12.2 µl, 0.86 mmol, 4 eq), toluene (5 mL), and a stir bar. The solution was cooled to 0 °C and NaHMDS (47 mg, 0.26 mmol, 1.2 eq) in toluene

(1 mL) was added dropwise via syringe. After stirring at this temperature for 1 h, the cooling bath was removed and stirring was continued for 2 h at ambient temperature. The residual volatiles were then removed under reduced pressure and the crude mixture was purified via column chromatography (5:1 v/v hexane/EtOAc, SiO_2) to afford the desired compound as a white solid (51 mg, 0.11 mmol, 54% yield). Evaporation of a saturated pentane solution afforded colorless crystalline plates suitable for single crystal X-ray diffraction analysis. m.p.= 124-126 °C. ^{1}H NMR (C_6D_6, 399.68 MHz): δ 0.44 (d, J = 6.7 Hz, 3H), 0.60 (s, 3H), 0.74 (t, J = 7.4 Hz, 3H), 1.22 (dd, J_1 = 1.6 Hz, J_2 = 6.7 Hz, 3H), 1.29 (d, J = 6.7 Hz, 3H), 1.36-1.41 (m, 6H), 1.60 (d, J = 9.0 Hz, 6H), 3.43 (d, J = 14.1 Hz, 1H), 1.99 (qd, J_1 = 1.6 Hz, J_2 = 7.4, 2H), 2.19 (d, J = 14.1 Hz, 1H), 2.87 (sept., J = 7.0 Hz, 1H), 3.45 (sept., J = 7.0 Hz, 1H), 6.93 (dd, J_1 = 2.0 Hz, J_2 = 7.0 Hz, 1H), 6.98 (t, J = 7.4 Hz, 1H), 7.07-7.12 (m, 4H), 7.47 (d, J = 7.8 Hz, 2H). ^{13}C NMR (C_6D_6, 100.50 MHz): δ 12.64, 19.25, 22.30, 22.48, 24.93, 25.53, 26.30, 28.63, 28.80, 29.46, 30.38, 32.47, 37.28, 38.38, 52.48, 58.47, 120.83, 123.19, 123.78, 128.12, 128.46, 128.92, 129.49, 129.80, 136.33, 147.03, 149.12, 177.02. IR (ATR): $\nu_{C=O}$ = 1637 cm^{-1}. HRMS (CI): $[M+H]^+$ calcd for $C_{31}H_{42}NO$: 444.3266; Found: 444.3271. Anal. Calcd for $C_{31}H_{41}NO$: C, 83.92; H, 9.31; N, 3.16. Found: C, 83.53; H, 9.49; N, 2.96.

1-(2,6-diisopropylphenyl)-6-mercapto-3,3,5,5-tetramethylpiperidin-2-one (8). Method A: A solution of **3** (146 mg, 0.42 mmol) and CS_2 (95 mg, 75 µl, 3 eq) in toluene (10 mL) was cooled to 0 °C with stirring. To the solution, NaHMDS (99 mg, 0.54 mmol, 1.3 eq) in toluene (1 mL) was added dropwise over a period of 5 min. The reaction solution gradually changed color from light orange to a dark purple color over the course of the addition. The reaction mixture was allowed to warm to room temperature overnight, after

which time a yellow reaction mixture with visible precipitate was observed. The residue was purified via column chromatography (10:1 hexane/EtOAc, SiO_2) to afford **8** (34 mg, 0.09 mmol, 23% yield) as an off-white solid as well as **6** (30 mg, 0.09 mmol, 21% yield). Method B: After cooling a Schlenk flask containing **3** (50 mg, 0.14 mmol) in toluene (10 mL) to 0 °C, the atmosphere was evacuated. The reaction vessel was then placed under an atmosphere of COS (g) (1 atm) and stirred. NaHMDS (37 mg, 0.20 mmol, 1.4 eq) in toluene (1 mL) was added slowly to the solution, which gradually turned yellow. After 1 h the cooling bath was removed and the reaction mixture was left stirring overnight. The residue was purified by column chromatography (10:1 v/v hexane/EtOAc, SiO_2) to afford **8** (28 mg, 0.08 mmol, 57% yield). m.p. = 157-159 °C. ^{1}H NMR ($CDCl_3$, 400.09 MHz): δ 1.11 (dd, J_1 = 1.2 Hz, J_2 = 5.1 Hz, 6H), 1.22 (s, 3H), 1.28 (t, J = 7.0 Hz, 6H), 1.34 (s, 3H), 1.40 (d, J = 5.1 Hz, 6H), 1.61 (d, J = 5.9 Hz, 1H), 1.67 (dd, J_1 = 1.6 Hz, J_2 = 14.5 Hz, 1H), 2.17 (d, J = 14.5, Hz, 1H), 2.98 (sept., J = 7.0 Hz, 1H), 3.07 (sept., J = 7.0 Hz, 1H), 4.77 (dd, J_1 = 1.6 Hz, J_2 = 5.9 Hz, 1H), 7.19 (t, J = 7.8 Hz, 2H), 7.32 (t, J = 7.8 Hz, 1H). ^{13}C NMR ($CDCl_3$, 100.60 MHz): δ 23.27, 23.35, 24.16, 24.99, 27.14, 28.02, 28.19, 28.89, 30.46, 31.22, 35.49, 38.24, 46.47, 71.73, 124.19, 124.28, 128.47, 136.23, 145.19, 148.07, 175.94. IR (ATR): $\nu_{C=O}$ = 1650 cm^{-1}. HRMS (ESI): $[M+H]^+$ calcd for $C_{21}H_{34}NOS$: 348.2356, Found: 348.2358. Anal. Calcd for $C_{21}H_{33}NOS$: C, 72.57; H, 9.57; N, 4.03; S, 9.22. Found: C, 72.24; H, 9.74; N, 3.98; S, 8.88.

1-(2,6-diisopropylphenyl)-3,3,5,5-tetramethyl-keto-piperidinyl-iridium (I) (1,5-cyclooctadiene) chloride (9). A Schlenk flask which was completely covered with aluminum foil was charged with **3** (100 mg, 0.29 mmol) and $[Ir(COD)Cl]_2$ (95.9 mg, 0.14 mmol, 0.5 eq.) and toluene (10 mL). The solution was cooled to 0 °C and NaHMDS (68

mg, 0.37 mmol, 1.3 eq.) in toluene (1 mL) was added dropwise with stirring. The reaction mixture was left in the dark overnight and allowed to warm to ambient temperature. The solvent was then removed under reduced pressure and the residue was purified by column chromatography (2:1 v/v CH_2Cl_2/hexane, SiO_2) to afford the desired compound as a red-orange solid (16 mg, 0.02 mmol, 9% yield). Crystals suitable for a single crystal X-ray diffraction analysis were obtained by slow evaporation of a heptanes solution of **9** over 48 h. m.p. = 187-189 °C (dec.). ^{1}H NMR ($CDCl_3$, 399.68 MHz): δ 0.95 (d, J = 6.7 Hz, 3H), 1.08 (dd, J_1 = 3.1 Hz, J_2 = 6.7 Hz, 6H), 1.21 (s, 4H), 1.37 (d, J = 6.3 Hz, 3H), 1.41 (d, J = 6.3 Hz, 6H), 1.53 (bs, 3H), 1.69-1.83 (m, 3H), 2.01-2.07 (m, 1H), 2.2 (s, 3H), 2.31 (sept., J = 7.8 Hz, 1H), 2.45 (sept., J = 6.7 Hz, 1H), 2.56 (d overlapping d, J_1 = 12.3 Hz, J_2 = 12.3 Hz, 2H), 3.50-3.55 (m, 1H), 3.59 (sept., J = 6.7 Hz, 1H), 4.69-4.74 (m, 1H), 4.80-4.86 (m, 1H), 7.14 (dd, J_1 = 1.6 Hz, J_2 = 7.4 Hz, 1H), 7.33 (dd, J_1 = 1.6 Hz, J_2 = 7.8 Hz, 1H), 7.41 (t, J = 7.4 Hz, 1H). ^{13}C NMR ($CDCl_3$, 100.60 MHz): δ 22.51, 23.65, 25.16, 25.43, 26.26, 26.83, 28.29, 28.42, 28.50, 29.53, 31.50, 32.09, 32.91, 34.42, 39.08, 42.55, 53.32, 53.53, 56.78, 92.55, 93.17, 122.47, 124.96, 129.28, 139.25, 145.43, 146.81, 176.72, 287.65. IR (ATR): $\nu_{C=O}$ = 1713 cm^{-1}. HRMS (ESI): $[M\text{-}Cl]^+$ calcd for $C_{29}H_{43}IrNO$: 614.2970; Found: 614.2971. Anal. Calcd for $C_{29}H_{43}ClIrNO$: C, 53.64; H, 6.68; N, 2.16. Found: C, 53.99; H, 6.73; N, 2.01.

1-(2,6-diisopropylphenyl)-3,3,5,5-tetramethyl-keto-piperidinyl-iridium(I) (dicarbonyl) chloride (10). Carbon monoxide was bubbled through a solution of **9** (20 mg, 0.03 mmol) in CH_2Cl_2 (3 mL) which immediately turned bright yellow. After the solvent had evaporated, hexanes (3 mL) was added and CO was continued to be bubbled through the solution until the solvent had evaporated; this process was repeated one more

time. The bright yellow solid was dried under reduced pressure, washed with a minimal amount of hexanes, and dried under reduced pressure again to afford the desired compound **10** as a bright yellow solid (17 mg, 0.03 mmol, 94% yield). m.p. = 128-130 °C (dec.). ^{1}H NMR ($CDCl_3$ 399.77 MHz): δ 0.94 (d, *J* = 7.0 Hz, 3H), 1.03 (d, *J* = 6.7 Hz, 3H), 1.34 (d, *J* = 6.3 Hz, 3H), 1.40 (d, *J* = 6.7 Hz, 3H), 1.44 (s, 3H), 1.50 (s, 3H), 1.65 (s, 3H), 1.97 (d overlapping s, 4H), 2.19 (d, *J* = 14.5 Hz, 1H), 2.72 (sept., *J* = 6.7 Hz, 1H), 2.96 (sept., *J* = 6.7 Hz, 1H), 7.29 (d, *J* = 7.8 Hz, 2H), 7.49 (t, *J* = 7.8 Hz, 1H). ^{13}C NMR ($CDCl_3$, 100.52 MHz): δ 22.66, 23.34, 25.13, 25.19, 28.39, 28.86, 29.61, 31.78, 33.04, 38.86, 45.21, 49.79, 124.06, 124.81, 138.79, 143.96, 144.94, 169.57, 175.72, 181.51, 280.64. IR (CH_2Cl_2, KBr): $\nu_{C=O}$ = 1756 cm^{-1}, 1986 cm^{-1}, 2068 cm^{-1}. HRMS (ESI): $[M+Na]^+$ calcd for $C_{23}H_{31}ClIrNO_3Na$: 620.1506; Found: 620.1511. Anal. Calcd for $C_{23}H_{31}ClIrNO_3$: C, 46.26; H, 5.23; N, 2.35. Found: C, 46.61; H, 5.58; N, 2.01.

1-(2,6-diisopropylphenyl)-3,3,5,5-tetramethyl-6-selenoxopiperidin-2-one (11). To a vial containing **3** (75 mg, 0.21 mmol) and selenium powder (51 mg, 0.65 mmol, 3 eq) in C_6D_6 (5 mL), NaHMDS (51 mg, 0.28 mmol, 1.3 eq) was added with stirring. The reaction mixture was left overnight after which time it was filtered through a PTFE filter. The resultant residue was purified via column chromatography (1:1 v/v CH_2Cl_2/hexane, SiO_2) to afford the desired compound as a magenta crystalline solid (46 mg, 0.12 mmol, 55% yield). m.p. = 128-130 °C. ^{1}H NMR ($CDCl_3$, 400.09 MHz): δ 1.10 (d, *J* = 7.0 Hz, 6H), 1.16 (d, *J* = 7.0 Hz, 6H), 1.46 (s, 6H), 1.62 (s, 6H), 2.07 (s, 2H), 2.59 (sept., *J* = 7.0 Hz, 2H), 7.21 (d, *J* = 7.8 Hz, 2H), 7.39 (t, *J* = 7.8 Hz, 1H). ^{13}C NMR ($CDCl_3$, 125.60 MHz): δ 23.95, 24.09. 28.63, 29.03, 33.58, 39.61, 45.44, 48.96, 125.14, 128.99, 138.24, 144.34, 174.85, 228.01. ^{77}Se NMR (acetone-d_6, 144.44 MHz): δ 1179.71. IR (ATR): $\nu_{C=O}$ = 1715 cm^{-1}.

HRMS (ESI): $[M+Na]^+$ calcd for $C_{21}H_{31}NOSeNa$: 416.1464; Found: 416.1470. Anal. Calcd for $C_{21}H_{31}NOS$: C, 64.27; H, 7.96; N, 3.57. Found: C, 64.44; H, 7.84; N, 3.32.

6.3.3 X-Ray Crystallography Information and Data

Colorless, single crystals of **3** were obtained by cooling a saturated hexane solution of **3** to -30 °C; this compound crystallized in the orthorhombic $P2_12_12_1$ space group with four molecules of **3**. Colorless, single crystals of **5** were obtained by slow evaporation of a saturated solution of diethyl ether/n-pentane (1:1 v/v); this compound crystallized in the monoclinic $P12_1/c1$ space group with four molecules of **5**. Colorless single crystals of **7** were grown by slow evaporation of a pentane solution; this compound crystallized in the monoclinic $P12_1/n1$space group with four molecules of **7** and four molecules of pentane, which was removed using SQUEEZE. Orange, single crystals of **9** were obtained by the slow evaporation of a heptane solution; this compound crystallized in the monoclinic $P12_1/c1$ space group with four molecules of **9**. Crystallographic measurements were carried out on a Rigaku Mini CCD, Nonius Kappa CCD, or Rigaku AFC-12 with Saturn 724+ CCD area detector diffractometer using graphite monochromated Mo-Kα radiation (λ = 0.71073 Å) at 100 K, 120 K, or 150 K using an Oxford Cryostream low temperature device. A sample of suitable size and quality was selected and mounted onto a nylon loop. Data reductions were performed using DENZO-SMN.[133] The structures were solved by direct methods which successfully located most of the non-hydrogen atoms. Subsequent refinements on *F*2 using the SHELXTL/PC package (version 6)[134] allowed the location of the remaining non-hydrogen atoms. Key details of the crystal and structure refinement data are summarized in Table S1. Further crystallographic details may be found in the respective CIFs which were deposited at the Cambridge Crystallographic Data Centre, Cambridge,

UK. The CCDC reference numbers for **3**, **5**, **7**, and **9** were assigned as 1024535, 1024536, 1024537, and 1024538, respectively.

Table 6.1: Summary of crystal data, data collection, and structure refinement details.

	3	**5**	**7**[a]	**9**
Formula	$C_{21}H_{32}NOCl$	$C_{21}H_{31}NO$	$C_{31}H_{41}NO$	$C_{29}H_{43}ClIrNO$
M_r	349.9	313.5	443.7	649.3
crystal size	0.20 × 0.20 × 0.20	0.23 × 0.18 × 0.08	0.20 × 0.20 × 0.20	0.34 × 0.10 × 0.06
crystal system	orthorhombic	monoclinic	monoclinic	monoclinic
space group	$P2_12_12_1$	$P12_1/c1$	$P12_1/n1$	$P12_1/c1$
a (Å)	11.6015(19)	8.9044(5)	8.6897(5)	15.8695(19)
b (Å)	12.8220(22)	11.5431(6)	29.0766(18)	11.8315(13)
c (Å)	13.4282(23)	17.7110(8)	10.8005(7)	14.60161(17)
α (°)	90.000(0)	90.000(0)	90.000(0)	90.000(0)
β (°)	90.000(0)	92.232(3)	106.809(3)	96.061(3)
γ (°)	90.000(0)	90.000(0)	90.000(0)	90.000(0)
V (Å^3)	1997.50(6)	1825.20(3)	2612.33(25)	2726.27(10)
Z	4	4	4	4
ρ_{calc} (g cm^{-3})	1.16	1.14	1.13	1.58
μ (mm^{-1})	0.199	0.069	0.066	5.016
F(000)	760.0	688.0	968.0	1304.0
T (K)	150(2)	120(2)	120(2)	100(2)
scan mode	ω	ω, φ	ω, φ	ω, φ
hkl range	-13 → 13 -15 → 15 -15 → 15	-10 → 10 -13 → 13 -21 → 20	-10 → 10 -34 → 34 -12 → 12	-18 → 18 -14 → 12 -17 → 17
measd reflns	17572	70507	141864	30408
unique reflns	3505 [0.067]	3217 [0.049]	4602 [0.069]	4778 [0.057]
refinement reflns	3505	3217	4602	4778
refined parameters	225	216	307	306
GOF on F^2	1.006	1.006	1.006	1.006
R1[b] (all data)	0.041 (0.044)	0.039 (0.046)	0.043 (0.055)	0.033(0.035)
wR2[c](all data)	0.107 (0.110)	0.098 (0.109)	0.119 (0.139)	0.090 (0.092)
ρ_{fin} (max/min) (e Å^{-3})	0.343 -0.213	0.287 -0.219	0.290 -0.234	1.732 -2.695

[a] A highly disordered molecule of pentane was removed using SQUEEZE. [b] $R1 = \Sigma||Fo| - |Fc||/\Sigma|Fo|$.
[c] $wR2 = \{[\Sigma w(Fo^2 - Fc^2)^2]/[\Sigma w(Fo^2)^2]\}^{1/2}$.

6.3.4: NMR Characterization Data

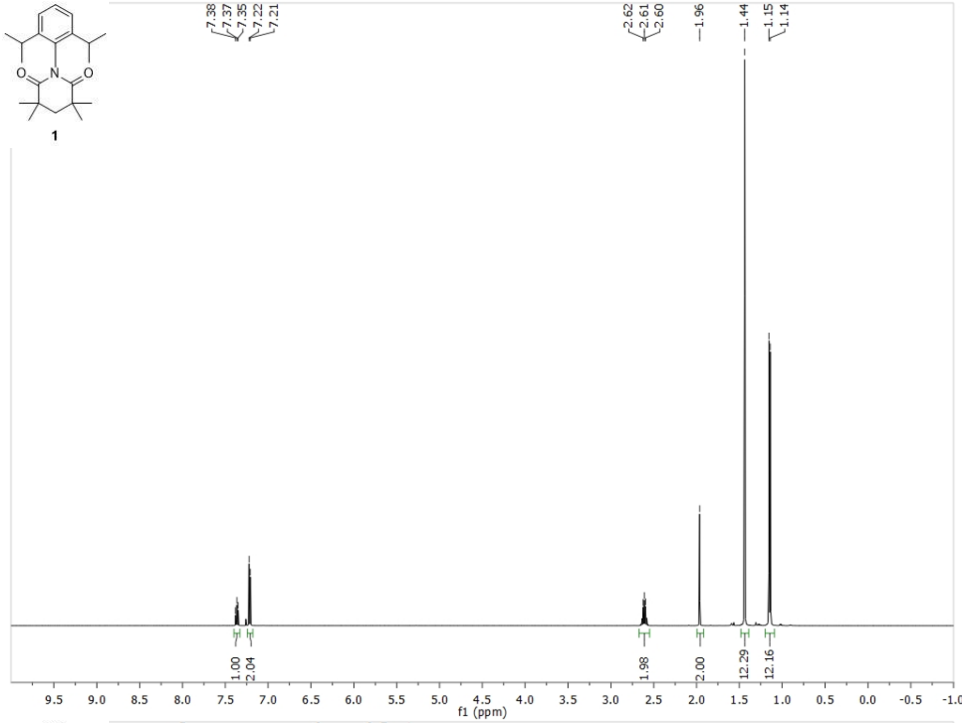

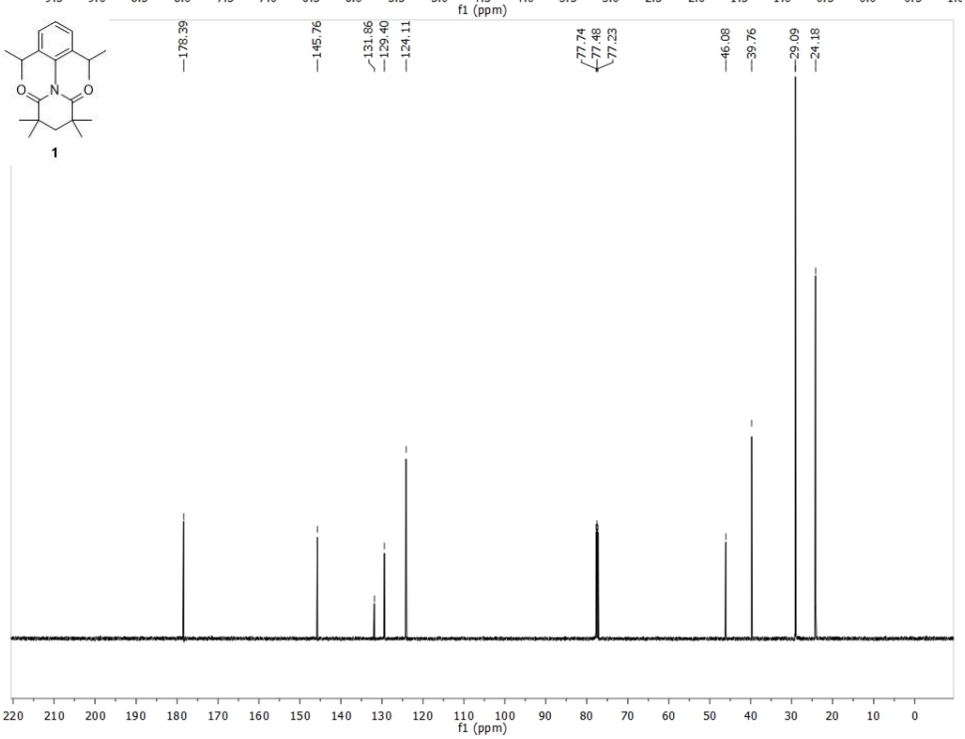

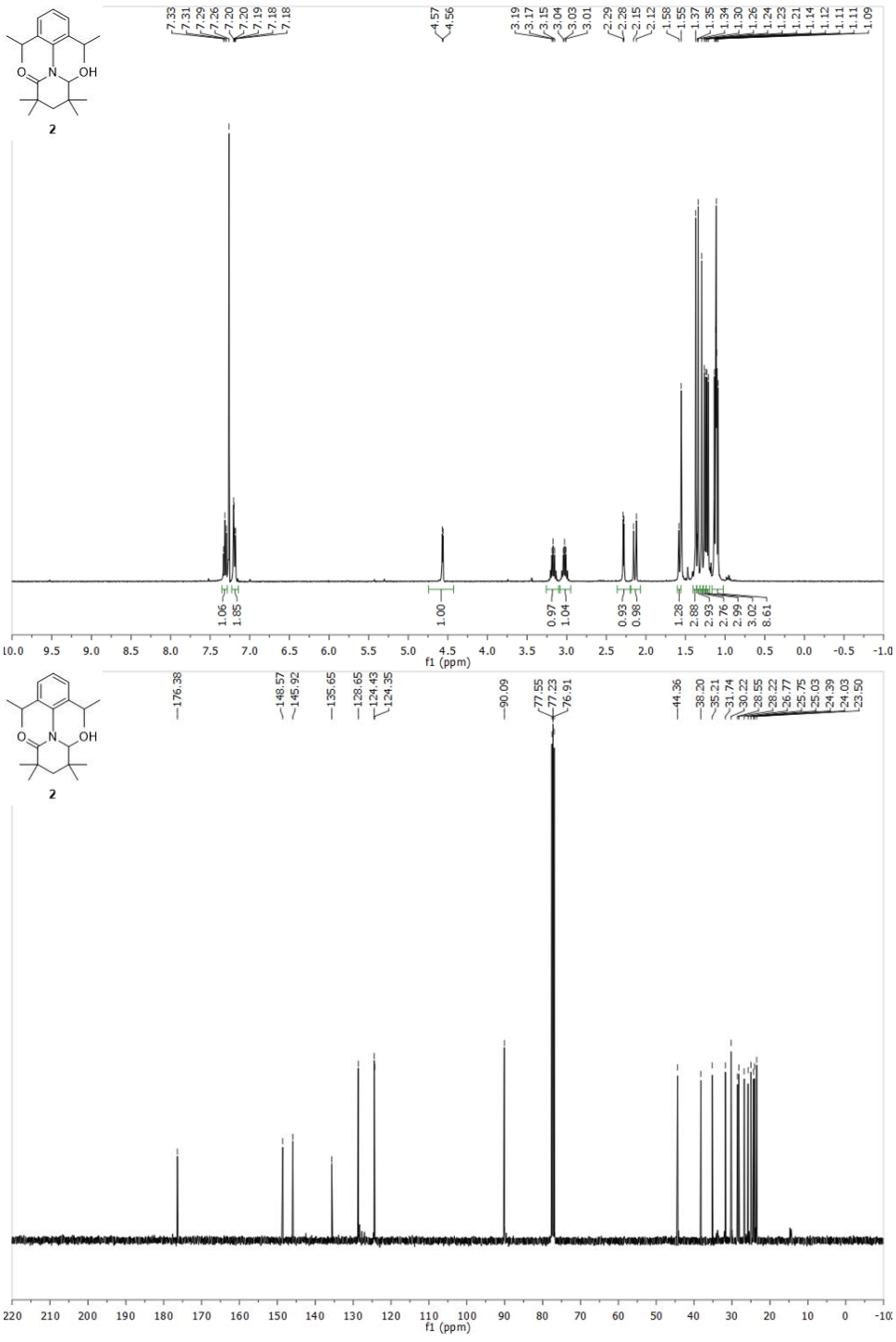
2
7.33
7.31
7.29
7.26
7.20
7.20
7.19
7.18
7.18
4.57
4.56
3.19
3.17
3.15
3.04
3.03
3.01
2.29
2.28
2.15
2.12
1.58
1.55
1.37
1.35
1.34
1.30
1.26
1.24
1.23
1.21
1.14
1.12
1.11
1.11
1.09
1.06
1.85
1.00
0.97
1.04
0.93
0.98
1.28
2.88
2.93
2.76
2.99
3.02
8.61
f1 (ppm)
2
176.38
148.57
145.92
135.65
128.65
124.43
124.35
90.09
77.55
77.23
76.91
44.36
38.20
35.21
31.74
30.22
28.55
28.22
26.77
25.75
25.03
24.39
24.03
23.50
f1 (ppm)

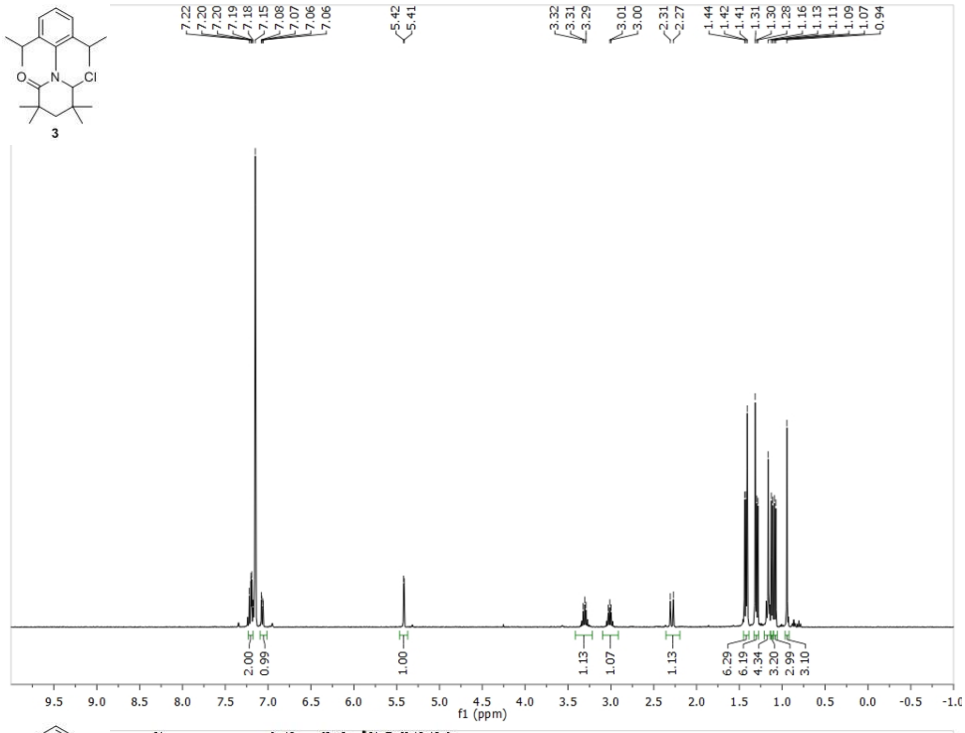
3
7.22
7.20
7.20
7.19
7.18
7.15
7.08
7.07
7.06
7.06
5.42
5.41
3.32
3.31
3.29
3.01
3.00
2.31
2.27
1.44
1.42
1.41
1.31
1.30
1.28
1.16
1.13
1.11
1.09
1.07
0.94
2.00
0.99
1.00
1.13
1.07
1.13
6.29
6.19
4.34
3.20
2.99
3.10
f1 (ppm)

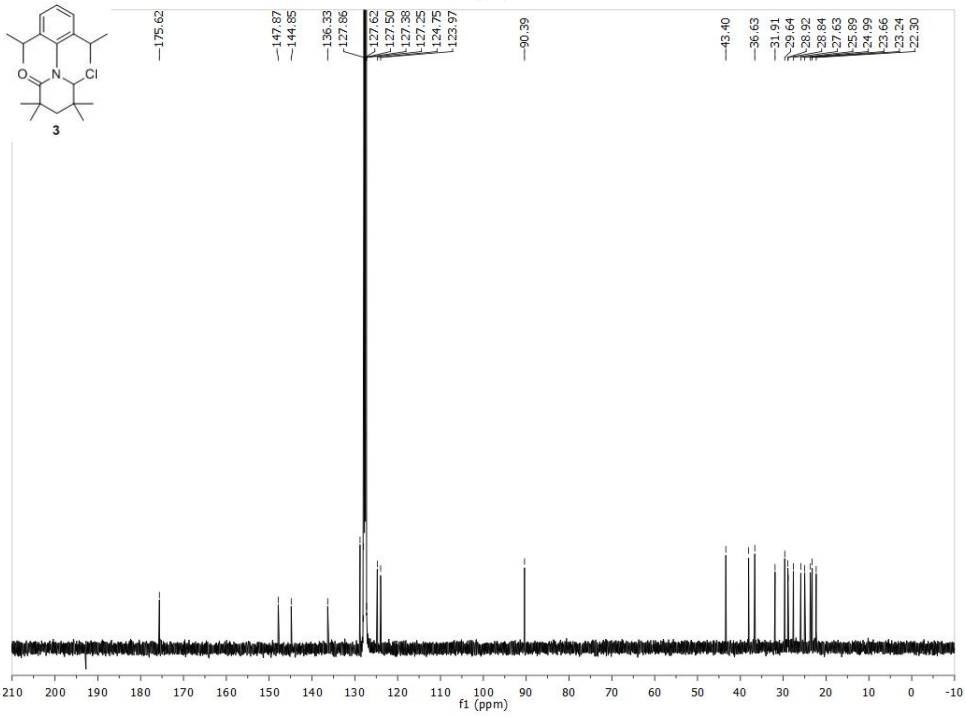
3
175.62
147.87
144.85
136.33
127.86
127.62
127.50
127.38
127.25
124.75
123.97
90.39
43.40
36.63
31.91
29.64
28.92
28.84
27.63
25.89
24.99
23.66
23.24
22.30
f1 (ppm)

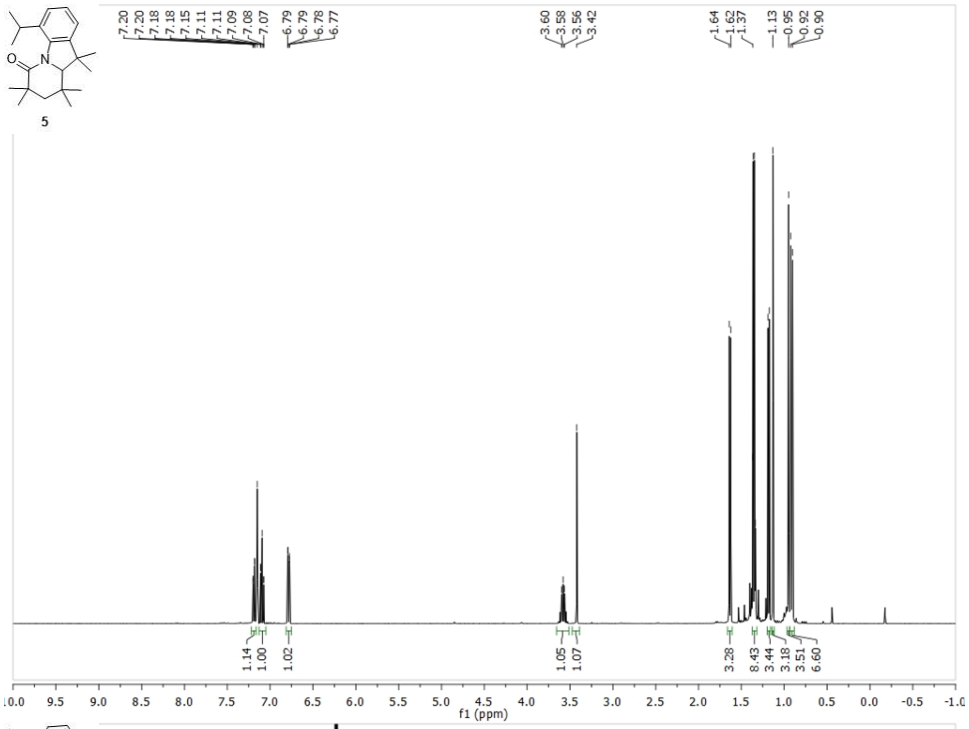
5
7.20
7.20
7.18
7.18
7.15
7.11
7.11
7.09
7.08
7.07
6.79
6.79
6.78
6.77
3.60
3.58
3.56
3.42
1.64
1.62
1.37
1.13
0.95
0.92
0.90
1.14
1.00
1.02
1.05
1.07
3.28
8.43
3.44
3.18
3.51
6.60
f1 (ppm)

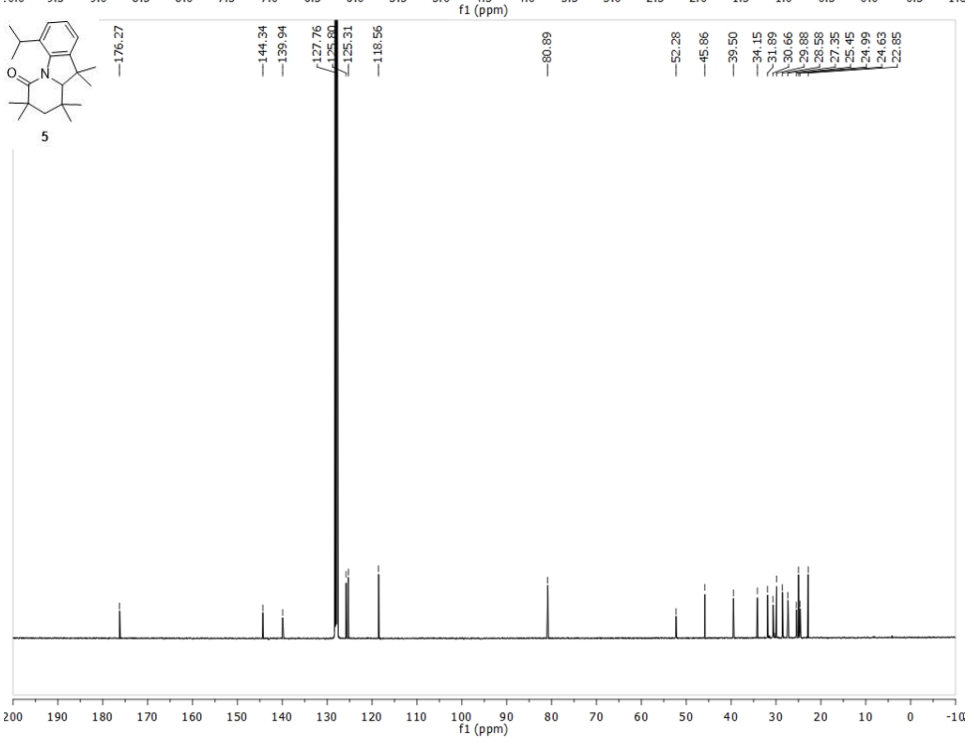
5
176.27
144.34
139.94
127.76
125.80
125.31
118.56
80.89
52.28
45.86
39.50
34.15
31.89
30.66
29.88
28.58
27.35
25.45
24.99
24.63
22.85
f1 (ppm)

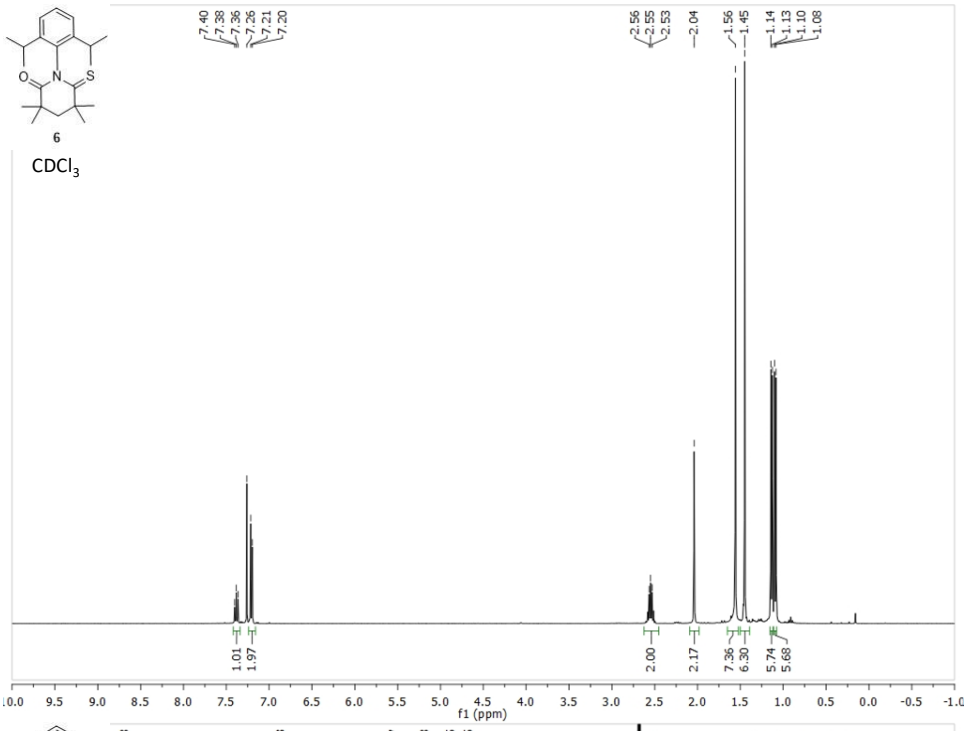
6
CDCl3
7.40
7.38
7.36
7.26
7.21
7.20
2.56
2.55
2.53
2.04
1.56
1.45
1.14
1.13
1.10
1.08
1.01
1.97
2.00
2.17
7.36
6.30
5.74
5.68
f1 (ppm)

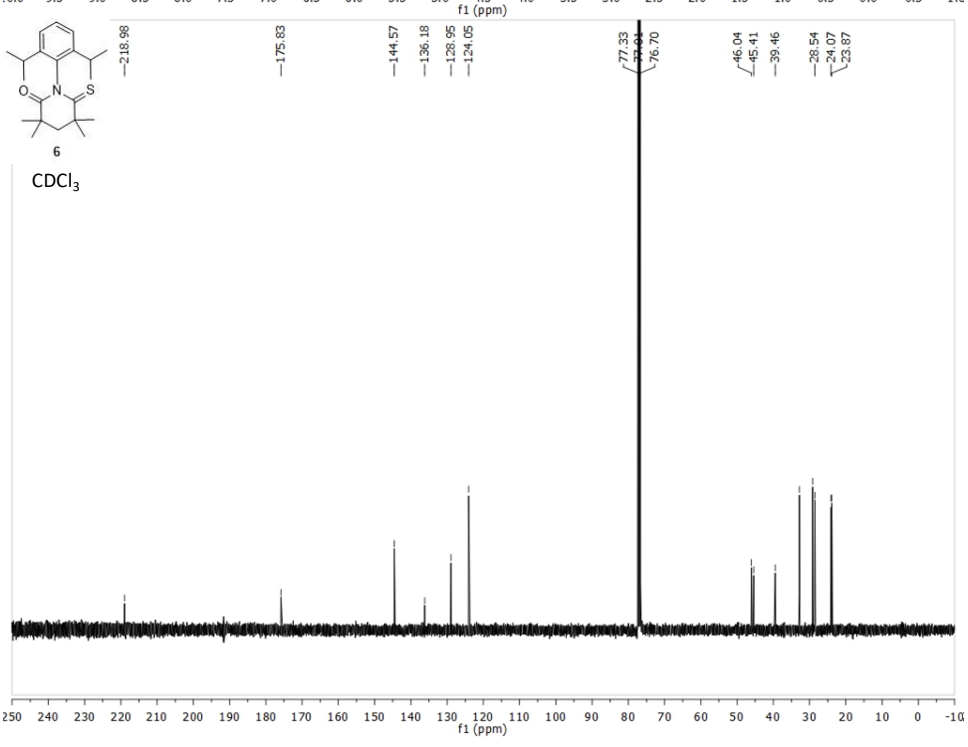
6
CDCl3
218.98
175.83
144.57
136.18
128.95
124.05
77.33
77.01
76.70
46.04
45.41
39.46
28.54
24.07
23.87
f1 (ppm)

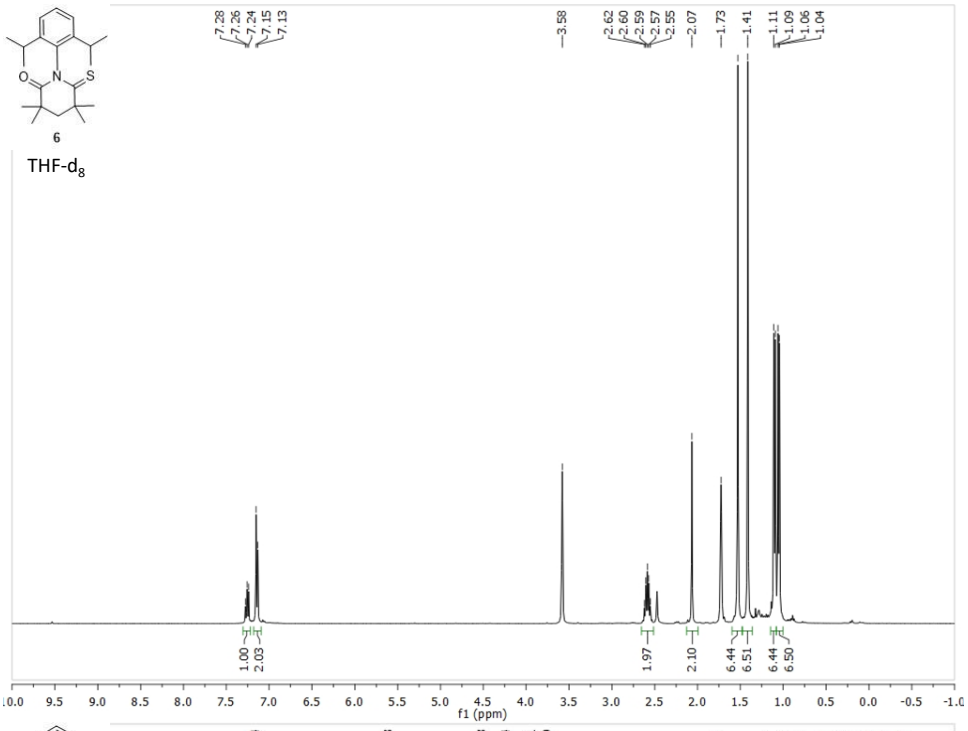
6
THF-d8
7.28
7.26
7.24
7.15
7.13
3.58
2.62
2.60
2.59
2.57
2.55
2.07
1.73
1.41
1.11
1.09
1.06
1.04
1.00
2.03
1.97
2.10
6.44
6.51
6.44
6.50
f1 (ppm)

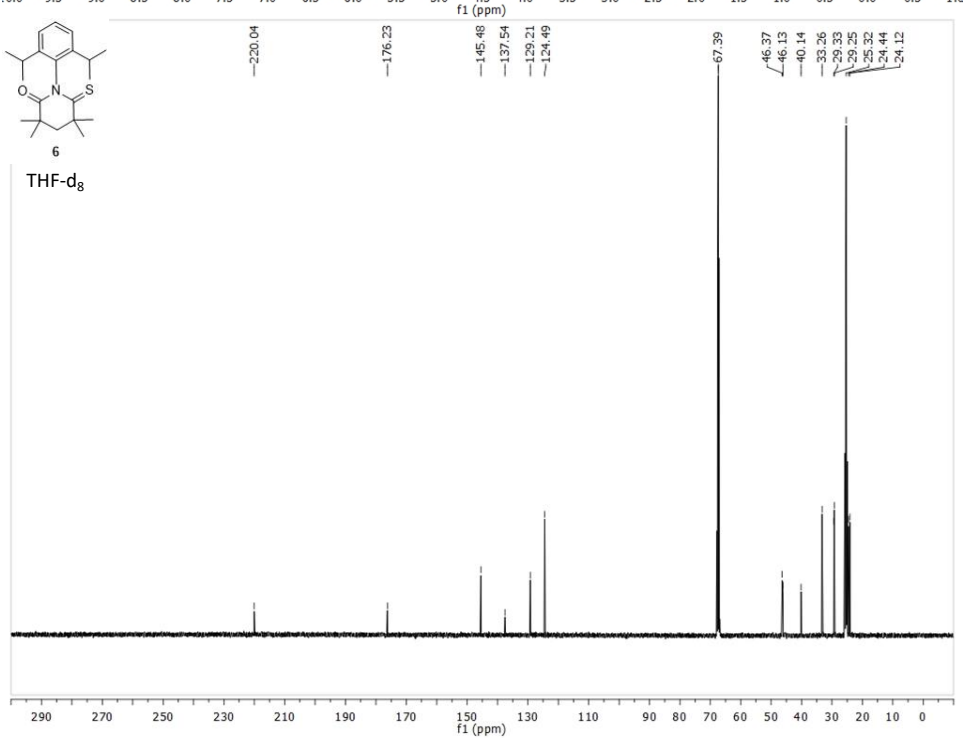
6
THF-d8
220.04
176.23
145.48
137.54
129.21
124.49
67.39
46.37
46.13
40.14
33.26
29.33
29.25
25.32
24.44
24.12
f1 (ppm)

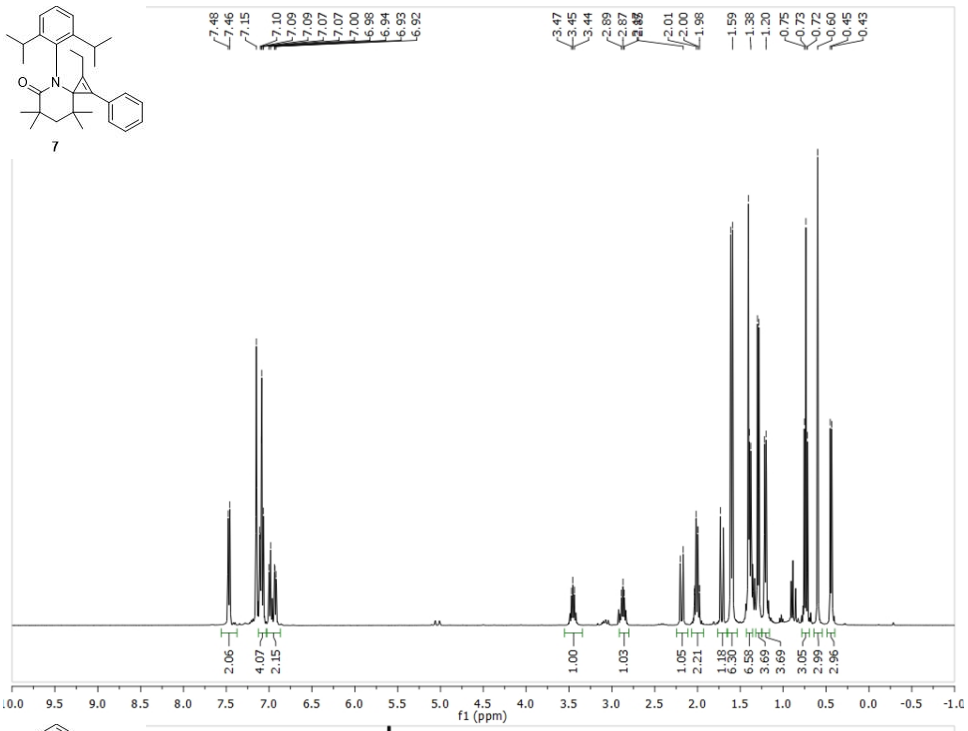
7.48
7.46
7.15
7.10
7.09
7.09
7.07
7.07
7.00
6.98
6.94
6.93
6.92
3.47
3.45
3.44
2.89
2.87
2.01
2.00
1.98
1.59
1.38
1.20
0.75
0.73
0.72
0.60
0.45
0.43
2.06
4.07
2.15
1.00
1.03
1.05
2.21
1.18
6.30
6.58
3.69
3.69
3.05
2.99
2.96
f1 (ppm)

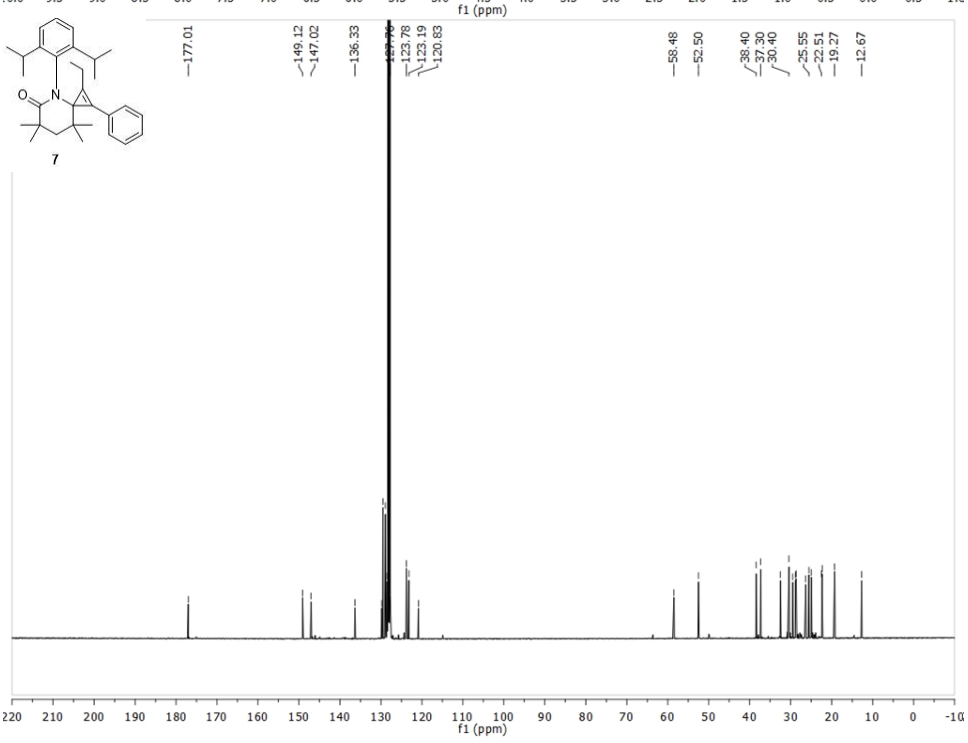
177.01
149.12
147.02
136.33
123.78
123.19
120.83
58.48
52.50
38.40
37.30
30.40
25.55
22.51
19.27
12.67
f1 (ppm)

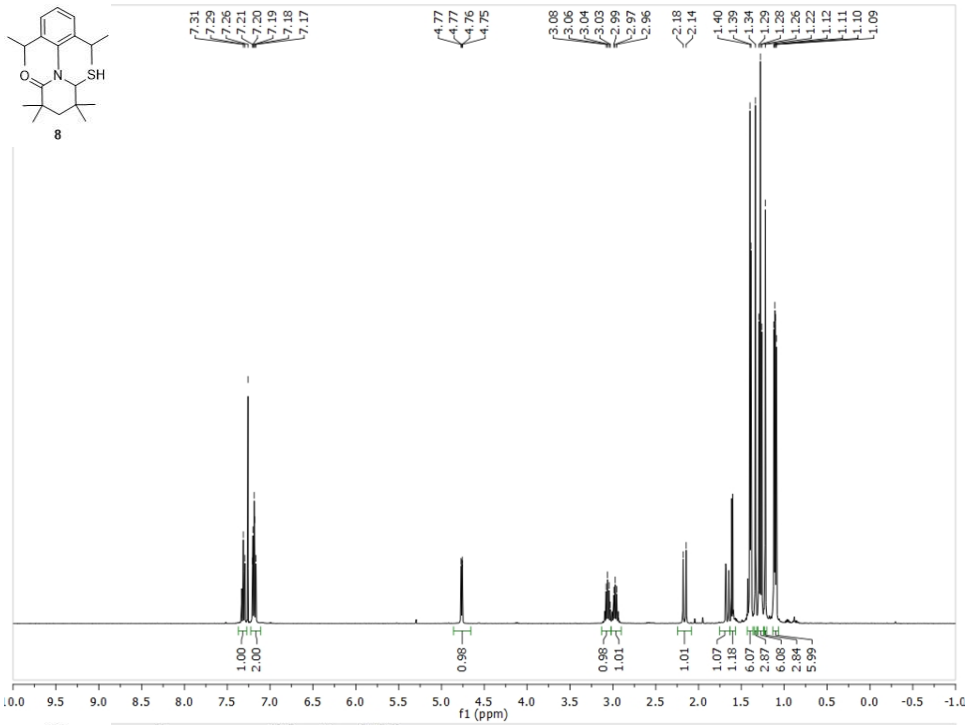
8
7.31
7.29
7.26
7.21
7.20
7.19
7.18
7.17
4.77
4.76
4.75
3.08
3.06
3.04
3.03
2.99
2.97
2.96
2.18
2.14
1.40
1.39
1.34
1.29
1.28
1.26
1.22
1.12
1.11
1.10
1.09
1.00
2.00
0.98
0.98
1.01
1.01
1.07
1.18
6.07
2.87
6.08
2.84
5.99
f1 (ppm)

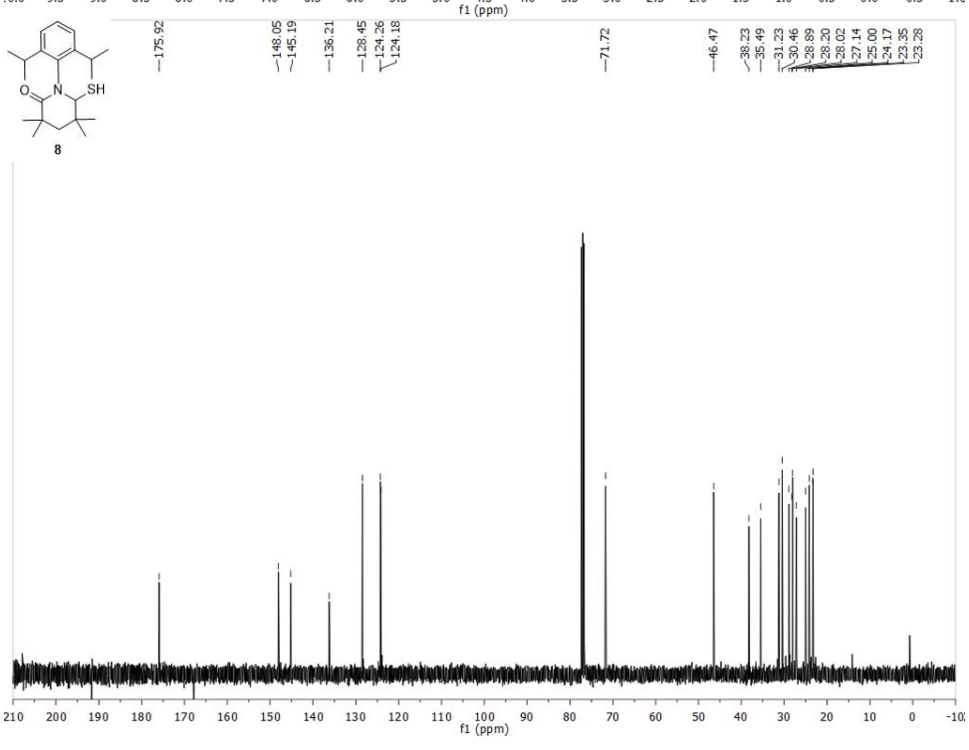
8
175.92
148.05
145.19
136.21
128.45
124.26
124.18
71.72
46.47
38.23
35.49
31.23
30.46
28.89
28.20
28.02
27.14
25.00
24.17
23.35
23.28
f1 (ppm)

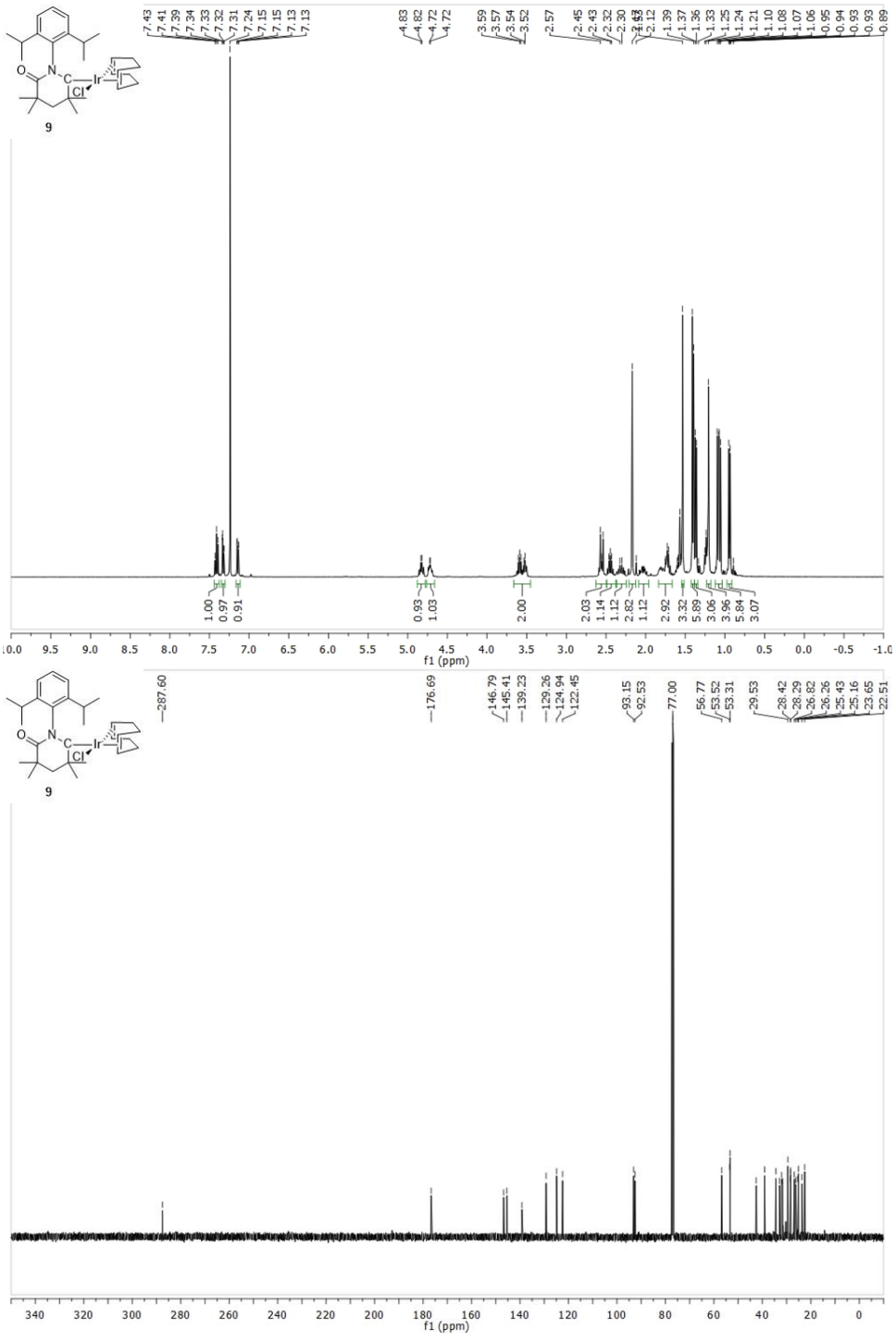
9
9
f1 (ppm)
f1 (ppm)

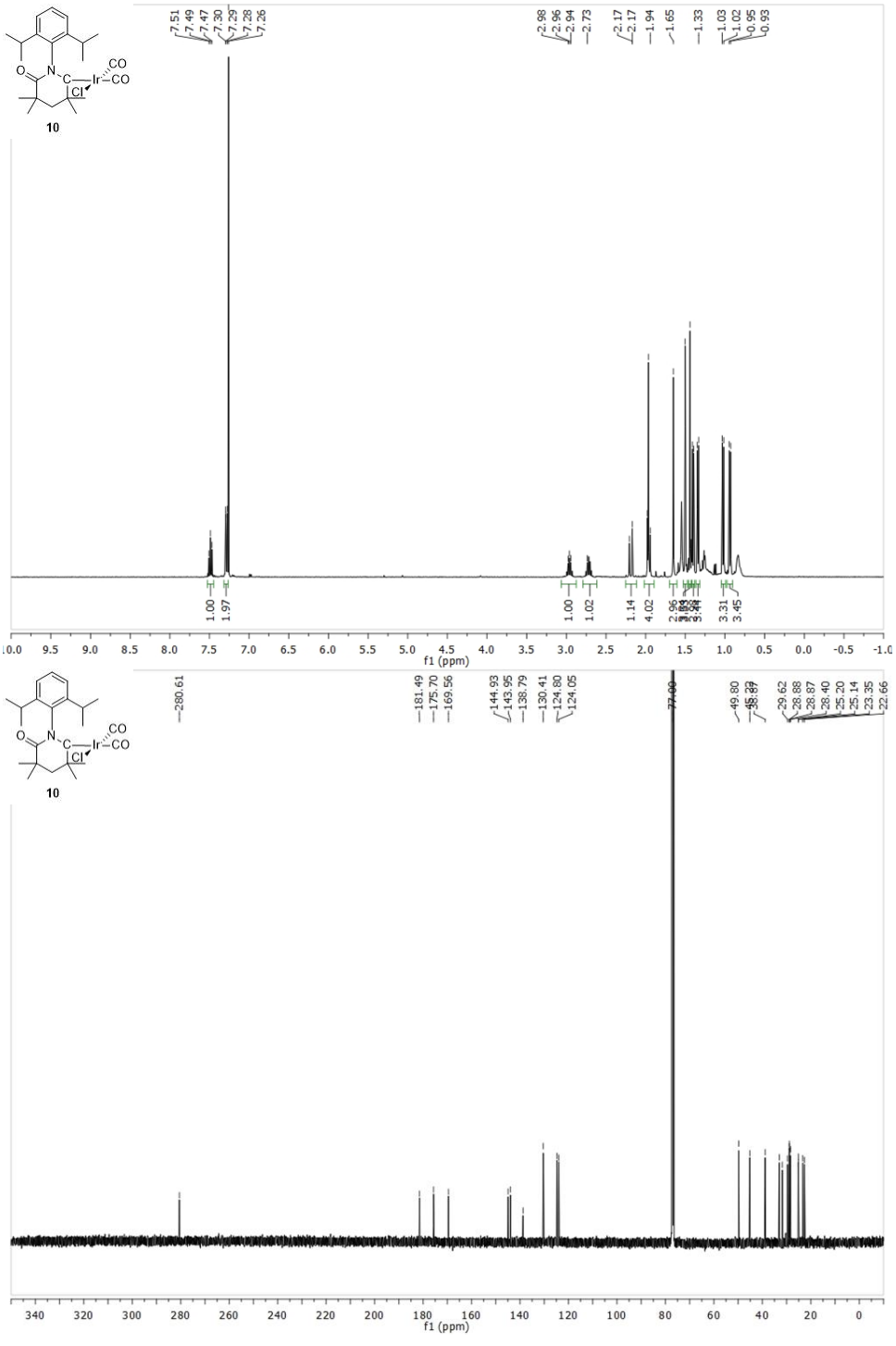
10
7.51
7.49
7.47
7.30
7.29
7.28
7.26
2.98
2.96
2.94
2.73
2.17
2.17
1.94
1.65
1.33
1.03
1.02
0.95
0.93
1.00
1.97
1.00
1.02
1.14
4.02
3.31
3.45
f1 (ppm)
10
280.61
181.49
175.70
169.56
144.93
143.95
138.79
130.41
124.80
124.05
77.00
49.80
29.62
28.88
28.87
28.40
25.20
25.14
23.35
22.66
f1 (ppm)

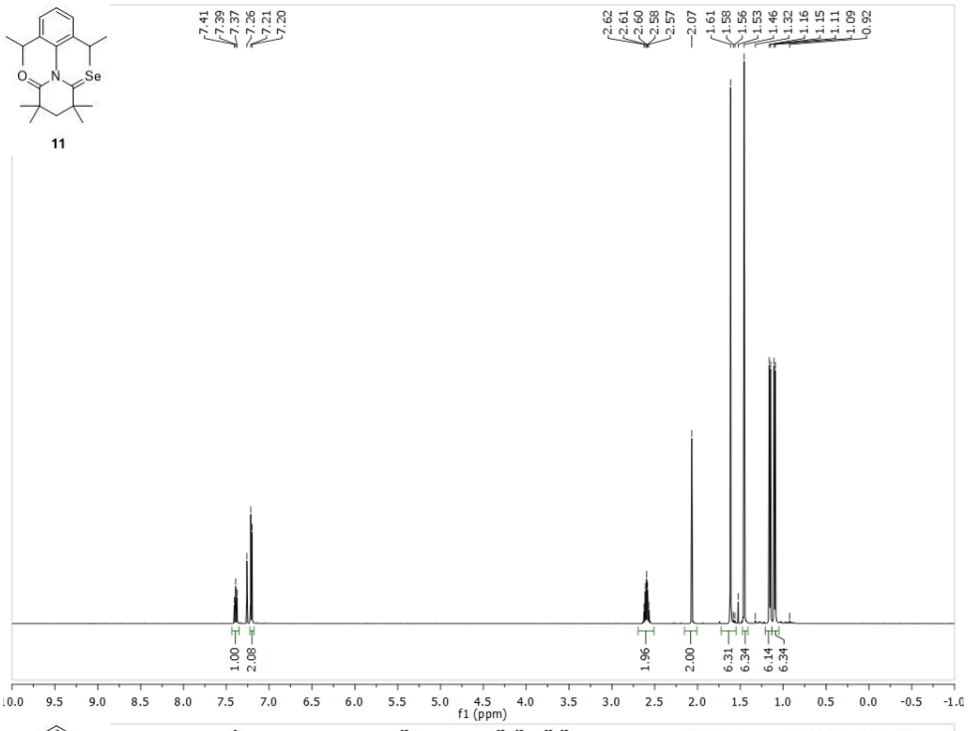
11
7.41
7.39
7.37
7.26
7.21
7.20
2.62
2.61
2.60
2.58
2.57
2.07
1.61
1.58
1.56
1.53
1.46
1.32
1.16
1.15
1.11
1.09
0.92
1.00
2.08
1.96
2.00
6.31
6.34
6.14
6.34
f1 (ppm)

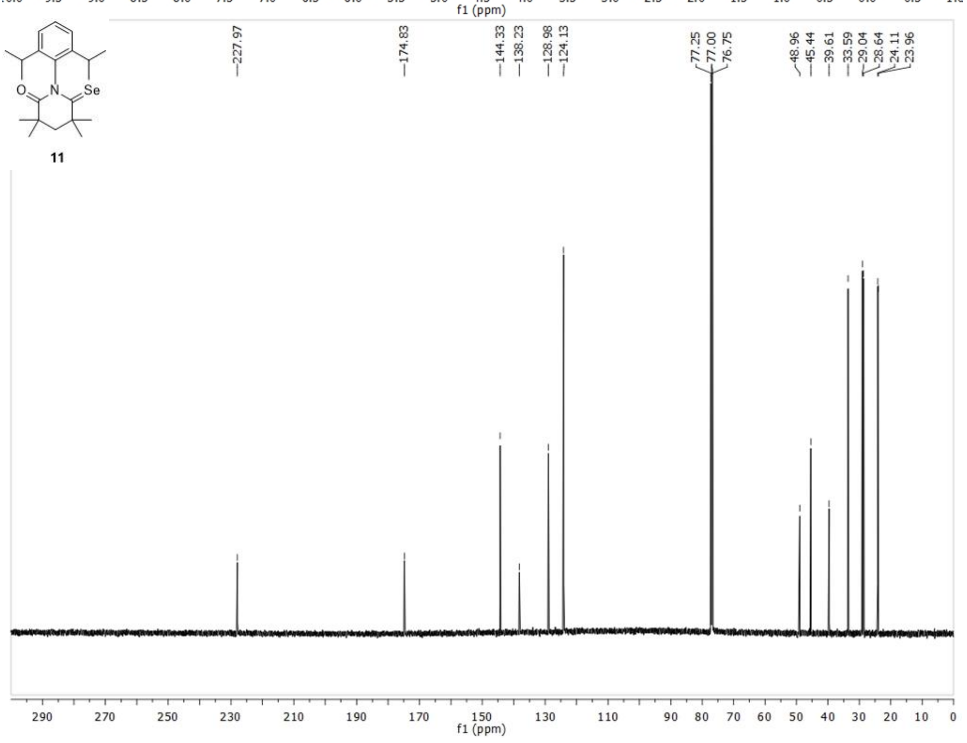
11
227.97
174.83
144.33
138.23
128.98
124.13
77.25
77.00
76.75
48.96
45.44
39.61
33.59
29.04
28.64
24.11
23.96
f1 (ppm)

O
N
Se

11

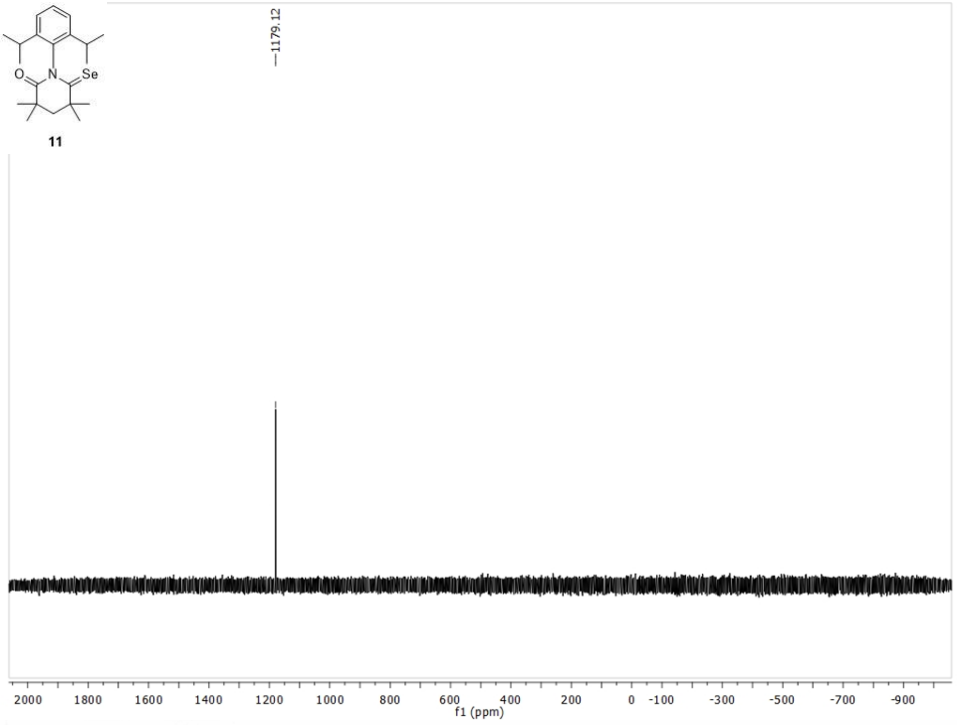
179.12
2000
1800
1600
1400
1200
1000
800
600
400
200
0
-100
-300
-500
-700
-900
f1 (ppm)

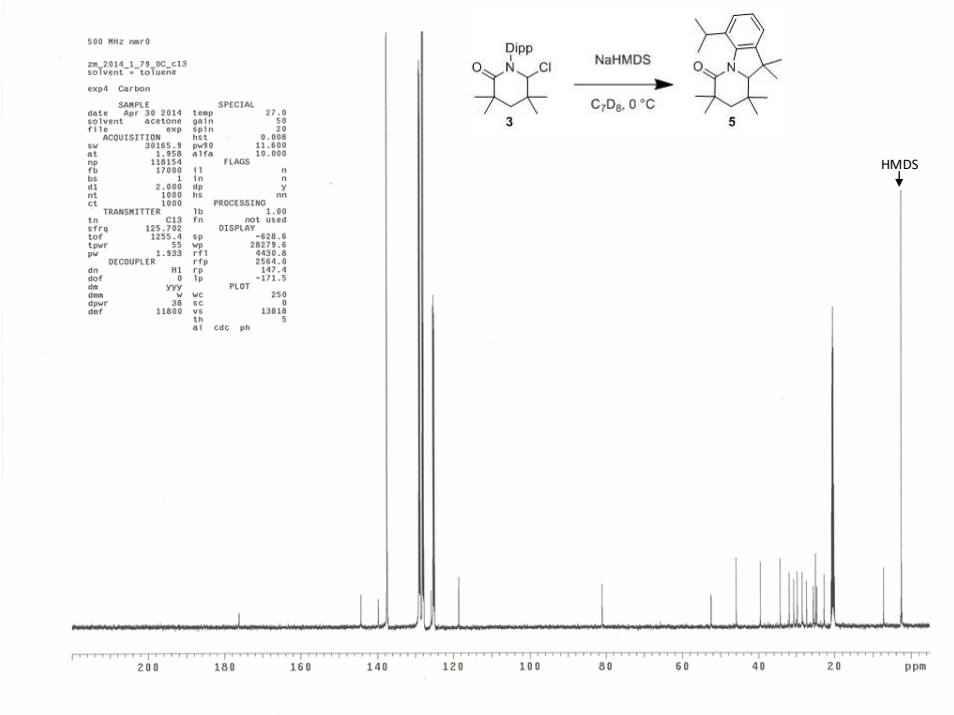
500 MHz nmr0
zm_2014_1_79_0C_c13
solvent = toluene
exp4 Carbon
SAMPLE
date Apr 30 2014
solvent acetone
file exp
ACQUISITION
sw 30165.9
at 1.958
np 118154
fb 17000
bs 1
d1 2.000
nt 1000
ct 1000
TRANSMITTER
tn C13
sfrq 125.702
tof 1255.4
tpwr 55
pw 1.933
DECOUPLER
dn H1
dof 0
dm yyy
dmm w
dpwr 38
dmf 11800
SPECIAL
temp 27.0
gain 50
spin 20
hst 0.008
pw90 11.600
alfa 10.000
FLAGS
il n
in n
dp y
hs nn
PROCESSING
lb 1.00
fn not used
DISPLAY
sp -628.6
wp 28279.6
rfl 4430.8
rfp 2564.0
rp 147.4
lp -171.5
PLOT
wc 250
sc 0
vs 13818
th 5
al cdc ph
Dipp
N
Cl
O
3
NaHMDS
C7D8, 0 °C
5
HMDS
200
180
160
140
120
100
80
60
40
20
ppm

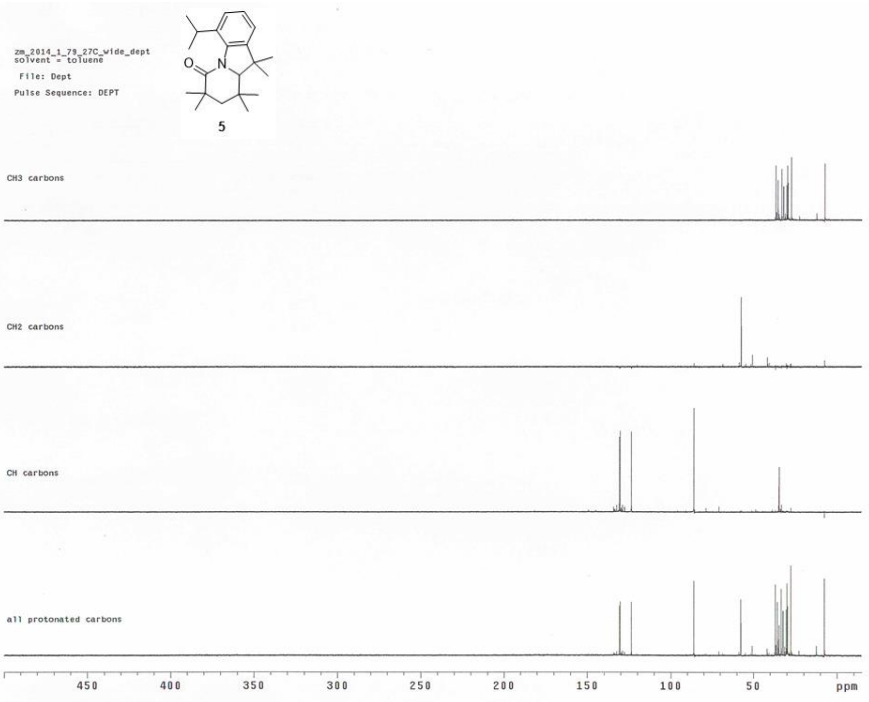
zm_2014_1_79_27C_wide_dept
solvent = toluene
File: Dept
Pulse Sequence: DEPT
5
CH3 carbons
CH2 carbons
CH carbons
all protonated carbons
450
400
350
300
250
200
150
100
50
ppm

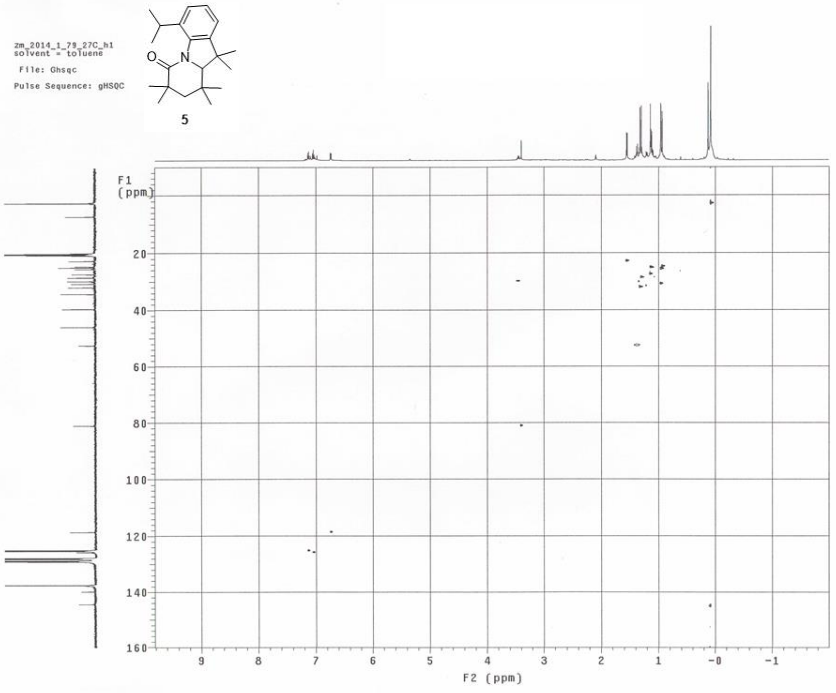
zm_2014_1_79_27C_h1
solvent = toluene
File: Ghsqc
Pulse Sequence: gHSQC
5
F1
(ppm)
20
40
60
80
100
120
140
160
9
8
7
6
5
4
3
2
1
-0
-1
F2 (ppm)

References

(1) Penn Engineering - ENIAC: Celebrating Penn Engineering History http://www.seas.upenn.edu/about-seas/eniac/operation.php (accessed Feb 5, 2018).

(2) Haviland, D. The Transistor - History https://www.nobelprize.org/educational/physics/transistor/history/index.html (accessed Feb 6, 2018).

(3) Riordan, M. The Lost History of the Transistor - IEEE Spectrum https://spectrum.ieee.org/tech-history/silicon-revolution/the-lost-history-of-the-transistor (accessed Feb 6, 2018).

(4) The Chip that Jack Built http://www.ti.com/corp/docs/kilbyctr/jackbuilt.shtml (accessed Feb 6, 2018).

(5) Moore, G. E. Cramming More Components on Integrated Circuits. *IEEE Solid State Circuits Soc. Newsl.* **1965**, *20*, 33–35.

(6) *Lithography*; Landis, S., Ed.; Wiley: London, 2011.

(7) Mack, C. *Fundamental Principles of Optical Lithography: The Science of Microfabrication*; John Wiley & Sons, Ltd, 2007.

(8) *Materials and Processes for Next Generation Lithography*; Robinson, A., Lawson, R., Eds.; Elsevier, 2016; Vol. 11.

(9) Willson, C. G.; Dammel, R. R.; Reiser, A. Photoresist Materials: A Historical Perspective. *Proc. SPIE 3051* **1997**, No. July 1997.

(10) Mack, C. A.; Byers, J. D. Exploring the Capabilities of Immersion Lithography through Simulation. *Proc. SPIE 5377* **2004**.

(11) Wei, Y.; Back, D. 193nm Immersion Lithography: Status and Challenges. *SPIE Newsroom* **2007**.

(12) Zimmerman, P. Double Patterning Lithography: Double the Trouble or Double the Fun? *SPIE Newsroom* **2009**, 1–3.

(13) Finders, J.; Dusa, M.; Vleeming, B.; Hepp, B.; Maenhoudt, M.; Cheng, S.; Vandeweyer, T. Double Patterning Lithography for 32 Nm: Critical Dimensions Uniformity and Overlay Control Considerations. *J. Micro/Nanolithography, MEMS MOEMS* **2009**, *8* (1), 11002.

(14) Hori, M.; Nagai, T.; Nakamura, A.; Abe, T.; Wakamatsu, G.; Kakizawa, T.; Anno, Y.; Sugiura, M.; Kusumoto, S.; Yamaguchi, Y.; et al. Sub-40nm Half-Pitch Double Patterning with Resist Freezing Process. *Proc. SPIE* **2008**, *6923* (March 2008), 69230H 1-8.

(15) Chen, Y.; Cheng, Q.; Kang, W. Technological Merits, Process Complexity, and Cost Analysis of Self-Aligned Multiple Patterning. *Proc. SPIE* **2012**, *8326* (March 2012), 832620 1-14.

(16) Zimmerman, P. Double Patterning Lithography: Double the Trouble or Double the Fun? *SPIE Newsroom* **2009**.

(17) Turkot, B.; Carson, S. L.; Lio, A.; Liang, T.; Phillips, M.; McCool, B.; Stenehjem, E.; Crimmins, T.; Zhang, G.; Sivakumar, S. EUV Progress toward HVM

Readiness. *Proc. SPIE* **2016**, *9776* (March 2016).
(18) Moore, S. K. EUV Lithography Finally Ready for Chip Manufacturing https://spectrum.ieee.org/semiconductors/nanotechnology/euv-lithography-finally-ready-for-chip-manufacturing (accessed Feb 21, 2018).
(19) Pease, R. F.; Chou, S. Y. Lithography and Other Patterning Techniques for Future Electronics. *Proc. IEEE* **2008**, *96* (2), 248–270.
(20) Leibler, L. Theory of Microphase Separation in Block Copolymers. *Macromolecules* **1980**, *13* (6), 1602–1617.
(21) Bates, F. S.; Fredrickson, G. H. Block Copolymer Thermodynamics: Theory and Experiment. *Annu. Rev. Phys. Chem.* **1990**, *41* (1), 525–557.
(22) Bates, F. S.; Fredrickson, G. H. Block Copolymers-Designer Soft Materials. *Phys. Today* **1999**, *52* (2), 32–38.
(23) Kim, H. C.; Park, S. M.; Hinsberg, W. D.; Division, I. R. Block Copolymer Based Nanostructures: Materials, Processes, and Applications to Electronics. *Chem. Rev.* **2010**, *110* (1), 146–177.
(24) Matsen, M. W.; Bates, F. S. Unifying Weak- and Strong-Segregation Block Copolymer Theories. *Macromolecules* **1996**, *29* (4), 1091–1098.
(25) Matsen, M. W. Equilibrium Behavior of Asymmetric ABA Triblock Copolymer Melts. *J. Chem. Phys.* **2000**, *113* (13), 5539.
(26) Sinturel, C.; Bates, F. S.; Hillmyer, M. A. High χ-Low N Block Polymers: How Far Can We Go? *ACS Macro Lett.* **2015**, *4* (9), 1044–1050.
(27) Henkee, C. S.; Thomas, E. L.; Fetters, L. J. The Effect of Surface Constraints on the Ordering of Block Copolymer Domains. *J. Mater. Sci.* **1988**, *23*, 1685–1694.
(28) Matsen, M. W. Self-Assembly of Block Copolymers in Thin Films. *Curr. Opin. Colloid Interface Sci.* **1998**, *3*, 40–47.
(29) Coulon, G.; Russell, T. P.; Deline, V. R.; Green, P. F. Surface-Induced Orientation of Symmetric, Diblock Copolymers: A Secondary Ion Mass Spectrometry Study Introduction Most of T H E Investigations Involving Molten Block Co. *Macromol.* **1989**, *22*, 2581–2589.
(30) Coulon, G.; Collin, B.; Ausserre, D.; Chatenay, D.; Russell, T. P. Islands and Holes on the Free Surface of Thin Diblock Copolymer Films. I. Characteristics of Formation and Growth. *J. Phys. Fr.* **1990**, *51*, 2801–2811.
(31) Mansky, P.; Russell, T. P.; Hawker, C. J.; Pitsikalis, M.; Mays, J. Ordered Diblock Copolymer Films on Random Copolymer Brushes. *Macromolecules* **1997**, *30*, 6810–6813.
(32) Russell, T. P.; Coulon, G.; Deline, V. R.; Miller, D. C. Characteristics of the Surface-Induced Orientation for Symmetric Diblock PS/PMMA Copolymers. *Macromolecules* **1989**, *22*, 4600–4606.
(33) Smith, A. P.; Douglas, J. F.; Meredith, J. C.; Amis, E. J.; Karim, A. Combinatorial Study of Surface Pattern Formation in Thin Block Copolymer Films. *Phys. Rev. Lett.* **2001**, *87* (1), 15503.
(34) Maher, M. J.; Bates, C. M.; Blachut, G.; Sirard, S.; Self, J. L.; Carlson, M. C.;

Dean, L. M.; Cushen, J. D.; Durand, W. J.; Hayes, C. O.; et al. Interfacial Design for Block Copolymer Thin Films. *Chem. Mater.* **2014**, *26* (3), 1471–1479.
(35) Kim, S.; Bates, C. M.; Thio, A.; Cushen, J. D.; Ellison, C. J.; Willson, C. G.; Bates, F. S. Consequences of Surface Neutralization in Diblock Copolymer Thin Films. *ACS Nano* **2013**, *7* (11), 9905–9919.
(36) Shelton, C. K.; Epps, T. H. Decoupling Substrate Surface Interactions in Block Polymer Thin Film Self-Assembly. *Macromolecules* **2015**, *48*, 4572–4580.
(37) Peters, R. D.; Yang, X. M.; Kim, T. K.; Sohn, B. H.; Nealey, P. F. Using Self-Assembled Monolayers Exposed to X-Rays To Control the Wetting Behavior of Thin Films of Diblock Copolymers. *Langmuir* **2000**, *16*, 4625–4631.
(38) Mansky, P. Controlling Polymer-Surface Interactions with Random Copolymer Brushes. *Science (80-.).* **1997**, *275* (5305), 1458–1460.
(39) Ji, S.; Liu, C.-C.; Gon Son, J.; Gotrik, K.; W Craig, G. S.; Gopalan, P.; Himpsel, F. J.; Char, K.; Nealey, P. F. Generalization of the Use of Random Copolymers To Control the Wetting Behavior of Block Copolymer Films. *Macromolecules* **2008**, *41*, 9098–9103.
(40) Bates, C. M.; Strahan, J. R.; Santos, L. J.; Mueller, B. K.; Bamgbade, B. O.; Lee, J. A.; Katzenstein, J. M.; Ellison, C. J.; Willson, C. G. Polymeric Cross-Linked Surface Treatments for Controlling Block Copolymer Orientation in Thin Films. *Langmuir* **2011**, *27* (5), 2000–2006.
(41) Keen, I.; Yu, A.; Cheng, H.-H.; Jack, K. S.; Nicholson, T. M.; Whittaker, A. K.; Blakey, I. Control of the Orientation of Symmetric Poly(styrene)-Block-poly(D,L-lactide) Block Copolymers Using Statistical Copolymers of Dissimilar Composition. *Langmuir* **2012**, *28* (15876–15888).
(42) Kennemur, J. G.; Hillmyer, M. A.; Bates, F. S. Synthesis, Thermodynamics, and Dynamics of Poly(4-Tert- Butylstyrene-b-methyl Methacrylate). *Macromolecules* **2012**, *45*, 7228–7236.
(43) Bates, Christopher, M.; Seshimo, T.; Maher, Michael, J.; Durand, William, J.; Cushen, Julia, D.; Dean, Leon, M.; Blachut, G.; Ellison, Christopher, J.; Willson, C. G. Polarity-Switching Top Coats Enable Orientation of Sub-10-Nm Block Copolymer Domains. *Science (80-.).* **2012**, *338* (November), 775–779.
(44) Lane, A. P.; Yang, X.; Maher, M. J.; Blachut, G.; Asano, Y.; Someya, Y.; Mallavarapu, A.; Sirard, S. M.; Ellison, C. J.; Willson, C. G. Directed Self-Assembly and Pattern Transfer of Five Nanometer Block Copolymer Lamellae. *ACS Nano* **2017**, *11* (8), 7656–7665.
(45) Darling, S. B. Directing the Self-Assembly of Block Copolymers. *Prog. Polym. Sci* **2007**, *32*, 1152–1204.
(46) Ruiz, R.; Kang, H.; Detcheverry, F. A.; Dobisz, E.; Kercher, D. S.; Albrecht, T. R.; De Pablo, J. J.; Nealey, P. F. Density Multiplication and Improved Lithography by Directed Block Copolymer Assembly. *Science (80-.).* **2008**, *321*, 936–939.
(47) Bita, I.; Yang, Joel, K. W.; Jung, Yeon, S.; Ross, Caroline, A.; Thomas, Edwin, L.; Berggren, Karl, K. Graphoepitaxy of Self-Assembled Block Copolymers on Two-

Dimensional Periodic Patterned Templates. *Science (80-.).* **2008**, *321*, 939–943.
(48) Stoykovich, M. P.; Nealey, P. F. Block Copolymers and Conventional Lithography. *Mater. Today* **2006**, *9* (9), 20–29.
(49) Gu, X.; Gunkel, I.; Russell, T. P. Pattern Transfer Using Block Copolymers. *Philos. Trans. R. Soc. A Math. Phys. Eng. Sci.* **2013**, *371* (2000).
(50) Asakawa, K.; Hiraoka, T.; Hieda, H.; Sakurai, M.; Kamata, Y.; Naito, K. Nano-Patterning for Patterned Media Using Block-Copolymers. *J. Photopolym. Sci. Technol.* **2002**, *15* (3), 465–470.
(51) Cummins, C.; Ghoshal, T.; Holmes, J. D.; Morris, M. A. Strategies for Inorganic Incorporation Using Neat Block Copolymer Thin Films for Etch Mask Function and Nanotechnological Application. *Adv. Mater.* **5586**, *28* (27), 5586–5618.
(52) Leng, C. Z.; Losego, M. D. Vapor Phase Infiltration (VPI) for Transforming Polymers into Organic–inorganic Hybrid Materials: A Critical Review of Current Progress and Future Challenges. *Mater. Horiz.* **2017**, *4*, 747–771.
(53) Gabor, A. H.; Lehner, E. A.; Mao, G.; Schneggenburger, L. A.; Ober, C. K. Synthesis and Lithographic Characterization of Block Copolymer Resists Consisting of Both Poly(styrene) Blocks and Hydrosiloxane-Modified Poly(diene) Blocks. *Chem. Mater* **1994**, *6*, 927–934.
(54) Colburn, M.; Grot, A.; Choi, B. J.; Amistoso, M.; Bailey, T.; Sreenivasan, S. V; Ekerdt, J. G.; Willson, C. G. Patterning Nonflat Substrates with a Low Pressure, Room Temperature, Imprint Lithography Process. *J. Vac. Sci. Technol. B* **2001**, *19* (6), 2162–2172.
(55) Durand, W. J.; Blachut, G.; Maher, M. J.; Sirard, S.; Tein, S.; Carlson, M. C.; Asano, Y.; Zhou, S. X.; Lane, A. P.; Bates, C. M.; et al. Design of High-χ Block Copolymers for Lithography. *J. Polym. Sci. Part A Polym. Chem.* **2015**, *53* (2), 344–352.
(56) Ferguson, J. D.; Weimer, A. W.; George, S. M. Atomic Layer Deposition of Al 2 O 3 Films on Polyethylene Particles. *Chem. Mater.* **2004**, *16*, 5602–5609.
(57) George, S. M. Atomic Layer Deposition: An Overview. *Chem. Rev.* **2010**, *110* (1), 111–131.
(58) Mackus, A. J. M.; Bol, A. A.; Kessels, W. M. M. The Use of Atomic Layer Deposition in Advanced Nanopatterning. *Nanoscale* **2014**, *6*, 10941–10960.
(59) Gay, G.; Baron, T.; Agraffeil, C.; Salhi, B.; Chevolleau, T.; Cunge, G.; Grampeix, H.; Tortai, J.-H.; Martin, F.; Jalaguier, E.; et al. CMOS Compatible Strategy Based on Selective Atomic Layer Deposition of a Hard Mask for Transferring Block Copolymer Lithography Patterns. *Nanotechnology* **2010**, *21*, 435301-.
(60) Peng, Q.; Tseng, Y. C.; Darling, S. B.; Elam, J. W. A Route to Nanoscopic Materials via Sequential Infiltration Synthesis on Block Copolymer Templates. *ACS Nano* **2011**, *5* (6), 4600–4606.
(61) Peng, Q.; Tseng, Y. C.; Darling, S. B.; Elam, J. W. Nanoscopic Patterned Materials with Tunable Dimensions via Atomic Layer Deposition on Block Copolymers. *Adv. Mater.* **2010**, *22* (45), 5129–5133.

(62) Tseng, Y. C.; Peng, Q.; Ocola, L. E.; Elam, J. W.; Darling, S. B. Enhanced Block Copolymer Lithography Using Sequential Infiltration Synthesis. *J. Phys. Chem. C* **2011**, *115* (36), 17725–17729.
(63) Dandley, E. C.; Needham, C. D.; Williams, P. S.; Brozena, A. H.; Oldham, C. J.; Parsons, G. N. Temperature-Dependent Reaction between Trimethylaluminum and Poly(methyl Methacrylate) during Sequential Vapor Infiltration: Experimental and Ab Initio Analysis. *J. Mater. Chem. C* **2014**, *2* (44), 9416–9424.
(64) Choi, J. W.; Li, Z.; Black, C. T.; Sweat, D. P.; Wang, X.; Gopalan, P. Patterning at the 10 Nanometer Length Scale Using a Strongly Segregating Block Copolymer Thin Film and Vapor Phase Infiltration of Inorganic Precursors. *Nanoscale* **2016**, *8* (22), 11595–11601.
(65) Ruiz, R.; Wan, L.; Lille, J.; Patel, K. C.; Dobisz, E.; Johnston, D. E.; Kisslinger, K.; Black, C. T. Image Quality and Pattern Transfer in Directed Self Assembly with Block-Selective Atomic Layer Deposition. *J. Vac. Sci. Technol. B, Nanotechnol. Microelectron. Mater. Process. Meas. Phenom.* **2012**, *30* (6), 06F202.
(66) Frechet, J. M.; Eichler, E. Poly(p-Tert-Butoxycarbonyloxystyrene): A Convenient Precursor to P-Hydroxystyrene Resins. *Polymer (Guildf).* **1983**, *24*, 995–1000.
(67) Ito, H. Chemical Amplification Resists: History and Development within IBM. *IBM Journal of Research and Development*. 2000, pp 119–130.
(68) Macdonald, S. A.; Schlosser, H.; Ito, H.; Clecak, N. J.; Willson, C. G. Plasma-Developable Photoresist Systems Based on Chemical Amplification. *Chem. Mater* **1991**, *3*, 435–442.
(69) Postnikov, S. V.; Somervell, M. H.; Henderson, C. L.; Katz, S.; Willson, C. G.; Byers, J.; Qin, A.; Qinghuang, L. Top Surface Imaging Through Silylation. *Proc. SPIE 3333*, 997–1008.
(70) Berkeley, U. C. Silylation of Poiy (T-BOC) Styrene Resists: Performance and Mechanisms C. A. Spence, S. A. MacDonaldt and H. Schiossert 509 Cory, Hall, E.R.L., U.C. Berkeley, Ca. 94720. *Proc. SPIE* **1990**, *1262*.
(71) Roland, B.; Lombaerts, R.; Jakus, C.; Coopmans, F. The Mechanism Of The Desire Process. *Proc. SPIE* **1987**, *811*, 55.
(72) Hutton, R. S. Application of Plasmask R Resist and the DESIRE Process to Lithography at 248 Nm. *J. Vac. Sci. Technol. B Microelectron. Nanom. Struct.* **1990**, *8* (6), 1502.
(73) Conlon, D. A.; Crivello, J. V.; Lee, J. L.; O'Brien, M. J. Synthesis, Characterization, and Deblocking of Poly(4-Tert- Butoxystyrene) and Poly(4-Tert-Butoxy-α-Methylstyrene). *Macromolecules* **1989**, *22* (2), 509–516.
(74) Peter, S.; Meyer, H.; Baschnagel, J. Thickness-Dependent Reduction of the Glass-Transition Temperature in Thin Polymer Films with a Free Surface. *J. Polym. Sci. Part B Polym. Phys.* **2006**, *44* (20), 2951–2967.
(75) Wu, W.-L.; Van Zanten, J. H.; Orts, W. J. Film Thickness Dependent Thermal Expansion in Ultrathin Poly(methy1 Methacrylate) Films on Silicon.

Macromolecules **1996**, *28*, 771–774.
(76) Kim, J. H.; Jang, J.; Lee, D.-Y.; Zin, W.-C. Thickness and Composition Dependence of the Glass Transition Temperature in Thin Homogeneous Polymer Blend Films. *Macromolecules* **2002**, *35*, 311–313.
(77) Pye, J. E.; Rohald, K. A.; Baker, E. A.; Roth, C. B. Physical Aging in Ultrathin Polystyrene Films: Evidence of a Gradient in Dynamics at the Free Surface and Its Connection to the Glass Transition Temperature Reductions. *Macromolecules* **2010**, *43*, 8296–8303.
(78) Singh, L.; Ludovice, P. J.; Henderson, C. L. Influence of Film Thickness, Molecular Weight, and Substrate on the Physical Properties of Photoresist Polymer Thin Films. *Proc. SPIE* **2003**, *5039* (404), 1008–1018.
(79) Kim, J. H.; Jang, J.; Zin, W. C. Thickness Dependence of the Glass Transition Temperature in Thin Polymer Films. *Langmuir* **2001**, *17* (17), 2703–2710.
(80) Taira, K.; Takahashi, J.; Yanagihara, K. Effect of Silylation Condition on the Silylated Image in the DESIRE Process. *Proc. SPIE* **1991**, *1466*, 570–582.
(81) Dalnoki-Veress, K.; Forrest, J. A.; Murray, C.; Gigault, C.; Dutcher, J. R. Molecular Weight Dependence of Reductions in the Glass Transition Temperature of Thin, Freely Standing Polymer Films. *Phys. Rev. E* **2001**, *63*, 31801.
(82) Kojima, K.; Sawamoto, M.; Higashimura, T. Block Copolymers of P-Tert-Butoxystyrene with Isobutyl Vinyl Ether or Styrene Derivatives via Sequential Living Cationic Polymerization: Synthesis of Amphiphilic Macromolecules with a Poly(p-Vinylphenol) Segment. *Macromolecules* **1991**, *24* (10), 2658–2662.
(83) Higaki, Y.; Otsuka, H.; Takahara, A. Synthesis of Well-Defined Poly(styrene)-B-Poly(P-Tert-Butoxystyrene) Multiblock Copolymer from Poly(alkoxyamine) Macroinitiator. *Polymer (Guildf).* **2003**, *44*, 7095–7101.
(84) Asari, T.; Matsuo, S.; Takano, A.; Matsushita, Y. Preparation and Characterization of Diblock Copolymers of the AB and CD Types and Their Self-Assembled Structure by Hydrogen Bonding Interaction. *Polym. J.* **2006**, *38* (3), 258–263.
(85) Gobius, G.; Sart, D.; Vukovic, I.; Alberda Van Ekenstein, G.; Polushkin, E.; Loos, K.; Ten Brinke, G. Self-Assembly of Supramolecular Triblock Copolymer Complexes. *Macromolecules* **2010**, *43*, 2970–2980.
(86) Faber, M.; Hofman, A. H.; Loos, K.; Brinke, G. ten. Highly Ordered Structure Formation in RAFT-Synthesized PtBOS- *B* -P4VP Diblock Copolymers. *Macromol. Rapid Commun.* **2016**, *37* (11), 911–919.
(87) Dynamic Secondary Ion Mass Spectrometry https://www.nrel.gov/materials-science/dynamic-secondary-ion.html (accessed Mar 31, 2018).
(88) X-Ray and UV Photoelectron Spectroscopy https://www.nrel.gov/materials-science/xray-uv-photoelectron.html (accessed Apr 1, 2018).
(89) Hamley, I. W.; Castelletto, V. Small-Angle Scattering of Block Copolymers in the Melt, Solution and Crystal States. *Prog. Polym. Sci.* **2004**, *29*, 909–948.
(90) Maher, M. J.; Self, J. L.; Stasiak, P.; Blachut, G.; Ellison, C. J.; Matsen, M. W.; Bates, C. M.; Willson, C. G. Structure, Stability, and Reorganization of 0.5

L0Topography in Block Copolymer Thin Films. *ACS Nano* **2016**, *10* (11), 10152–10160.
(91) Hahn, F. E.; Jahnke, M. C. Heterocyclic Carbenes: Synthesis and Coordination Chemistry. *Angew. Chemie, Int. Ed.* **2008**, *47* (17), 3122–3172.
(92) Hopkinson, M. N.; Richter, C.; Schedler, M.; Glorius, F. An Overview of N-Heterocyclic Carbenes. *Nat. (London, United Kingdom)* **2014**, *510* (7506), 485–496.
(93) Melaimi, M.; Soleilhavoup, M.; Bertrand, G. Stable Cyclic Carbenes and Related Species beyond Diaminocarbenes. *Angew. Chemie, Int. Ed.* **2010**, *49* (47), 8810–8849.
(94) Hudnall, T. W.; Bielawski, C. W. An N,N'-diamidocarbene: Studies in C-H Insertion, Reversible Carbonylation, and Transition-Metal Coordination Chemistry. *J. Am. Chem. Soc.* **2009**, *131* (44), 16039–16041.
(95) Hudnall, T. W.; Moerdyk, J. P.; Bielawski, C. W. Ammonia N-H Activation by a N,N'-diamidocarbene. *Chem. Commun. (Cambridge, United Kingdom)* **2010**, *46* (24), 4288–4290.
(96) Hudnall, T. W.; Tennyson, A. G.; Bielawski, C. W. A Seven-Membered N,N'-Diamidocarbene. *Organometallics* **2010**, *29* (20), 4569–4578.
(97) Blake, G. A.; Moerdyk, J. P.; Bielawski, C. W. Tuning the Electronic Properties of Carbenes: A Systematic Comparison of Neighboring Amino versus Amido Groups. *Organometallics* **2012**, *31* (8), 3373–3378.
(98) Moerdyk, J. P.; Bielawski, C. W. Reductive Generation of Stable, Five-Membered N,N'-diamidocarbenes. *Chem. Commun. (Cambridge, United Kingdom)* **2014**, *50* (35), 4551–4553.
(99) Cesar, V.; Lugan, N.; Lavigne, G. A Stable Anionic N-Heterocyclic Carbene and Its Zwitterionic Complexes. *J. Am. Chem. Soc.* **2008**, *130* (34), 11286–11287.
(100) Benhamou, L.; Cesar, V.; Gornitzka, H.; Lugan, N.; Lavigne, G. Imidazol-2-Ylidene-4-Olate: An Anionic N-Heterocyclic Carbene Pre-Programmed for Further Derivatization. *Chem. Commun. (Cambridge, United Kingdom)* **2009**, No. 31, 4720–4722.
(101) Cesar, V.; Lugan, N.; Lavigne, G. Reprogramming of a Malonic N-Heterocyclic Carbene: A Simple Backbone Modification with Dramatic Consequences on the Ligand's Donor Properties. *Eur. J. Inorg. Chem.* **2010**, No. 3, 361–365.
(102) Hobbs, M. G.; Forster, T. D.; Borau-Garcia, J.; Knapp, C. J.; Tuononen, H. M.; Roesler, R. The Influence of Electron Delocalization upon the Stability and Structure of Potential N-Heterocyclic Carbene Precursors with 1,3-Diaryl-Imidazolidine-4,5-Dione Skeletons. *New J. Chem.* **2010**, *34* (7), 1295–1308.
(103) Braun, M.; Frank, W.; Reiss, G. J.; Ganter, C. An N-Heterocyclic Carbene Ligand with an Oxalamide Backbone. *Organometallics* **2010**, *29* (20), 4418–4420.
(104) Braun, M.; Frank, W.; Ganter, C. Reactivity of an Oxalamide-Based N-Heterocyclic Carbene. *Organometallics* **2012**, *31* (5), 1927–1934.
(105) Makhloufi, A.; Frank, W.; Ganter, C. Diamino- and Mixed Amino-Amido-N-

Heterocyclic Carbenes Based on Triazine Backbones. *Organometallics* **2012**, *31* (5), 2001–2008.
(106) Makhloufi, A.; Frank, W.; Ganter, C. Converting Caffeine to Electronically Different N-Heterocyclic Carbenes with a Hypoxanthine Backbone. *Organometallics* **2012**, *31* (20), 7272–7277.
(107) Makhloufi, A.; Wahl, M.; Frank, W.; Ganter, C. A New Mixed Amino-Amido N-Heterocyclic Carbene Based on Anthranilic Acid. *Organometallics* **2013**, *32* (3), 854–861.
(108) Tapu, D.; McCarty, Z.; McMillen, C. A Stable Janus bis(maloNHC) and Its Zwitterionic Coinage Metal Complexes. *Chem. Commun.* **2014**.
(109) Moerdyk, J. P.; Bielawski, C. W. N,N'-Diamidocarbenes Facilitate Selective C[n.63743]H Insertions and Transfer Hydrogenation. *Chem. - A Eur. J.* **2013**, *19* (44), 14773–14776.
(110) Moerdyk, J. P.; Bielawski, C. W. Diamidocarbenes as Versatile and Reversible [2 + 1] Cycloaddition Reagents. *Nat. Chem.* **2012**, *4* (4), 275–280.
(111) Moerdyk, J. P.; Bielawski, C. W. Alkyne and Reversible Nitrile Activation: N,N'-Diamidocarbene-Facilitated Synthesis of Cyclopropenes, Cyclopropenones, and Azirines. *J. Am. Chem. Soc.* **2012**, *134* (14), 6116–6119.
(112) Lavallo, V.; Canac, Y.; Prasang, C.; Donnadieu, B.; Bertrand, G. Stable Cyclic (Alkyl)(amino)carbenes as Rigid or Flexible, Bulky, Electron-Rich Ligands for Transition-Metal Catalysts: A Quaternary Carbon Atom Makes the Difference. *Angew. Chemie, Int. Ed.* **2005**, *44* (35), 5705–5709.
(113) Lavallo, V.; Canac, Y.; Donnadieu, B.; Schoeller, W. W.; Bertrand, G. CO Fixation to Stable Acyclic and Cyclic Alkyl Amino Carbenes: Stable Amino Ketenes with a Small HOMO-LUMO Gap. *Angew. Chemie, Int. Ed.* **2006**, *45* (21), 3488–3491.
(114) Frey, G. D.; Lavallo, V.; Donnadieu, B.; Schoeller, W. W.; Bertrand, G. Facile Splitting of Hydrogen and Ammonia by Nucleophilic Activation at a Single Carbon Center. *Sci. (Washington, DC, United States)* **2007**, *316* (5823), 439–441.
(115) Martin, D.; Canac, Y.; Lavallo, V.; Bertrand, G. Comparative Reactivity of Different Types of Stable Cyclic and Acyclic Mono- and Diamino Carbenes with Simple Organic Substrates. *J. Am. Chem. Soc.* **2014**, *136* (13), 5023–5030.
(116) Soleilhavoup, M.; Bertrand, G. Cyclic (Alkyl)(Amino)Carbenes (CAACs): Stable Carbenes on the Rise. *Acc. Chem. Res.* **2015**, *48* (2), 256–266.
(117) Renner, C. A.; Greene, F. D. Diaziridinones (2,3-Diazacyclopropanones). A Cis-Fused Example. Lone Pair-Lone Pair Destabilization. *J. Org. Chem.* **1976**, *41* (17), 2813–2819.
(118) Batsanov, S. S. Van Der Waals Radii of Elements. *Inorg. Mater. (Translation Neorg. Mater.* **2001**, *37* (9), 871–885.
(119) Tretiakov, M.; Shermolovich, Y. G.; Singh, A. P.; Samuel, P. P.; Roesky, H. W.; Niepoetter, B.; Visscher, A.; Stalke, D. Lewis-Base Stabilized Diiodine Adducts with N-Heterocyclic Chalcogenamides. *Dalt. Trans.* **2013**, *42* (36), 12940–12946.

(120) Delaude, L. Betaine Adducts of N-Heterocyclic Carbenes. Synthesis, Properties, and Reactivity. *Eur. J. Inorg. Chem.* **2009**, No. 13, 1681–1699.
(121) Moltzen, E. K.; Klabunde, K. J.; Senning, A. Carbon Monosulfide: A Review. *Chem. Rev. (Washington, DC, United States)* **1988**, *88* (2), 391–406.
(122) Hans, M.; Wouters, J.; Demonceau, A.; Delaude, L. Synthesis and Organocatalytic Applications of Imidazol(in)ium-2-Thiocarboxylates. *European J. Org. Chem.* **2011**, *2011* (35), 7083–7091.
(123) Procopio, L. J.; Carroll, P. J.; Berry, D. H. Reactions of Carbon Dioxide and Carbon Disulfide with η2-Silanimine Complexes of Zirconium: Facile Deoxygenation and Desulfurization Reactions. *Organometallics* **1993**, *12* (8), 3087–3093.
(124) Kelly III, R. A.; Clavier, H.; Giudice, S.; Scott, N. M.; Stevens, E. D.; Bordner, J.; Samardjiev, I.; Hoff, C. D.; Cavallo, L.; Nolan, S. P. Determination of N-Heterocyclic Carbene (NHC) Steric and Electronic Parameters Using the [(NHC)Ir(CO)2Cl] System. *Organometallics* **2008**, *27* (2), 202–210.
(125) Wolf, S.; Plenio, H. Synthesis of (NHC)Rh(cod)Cl and (NHC)RhCl(CO)2 Complexes - Translation of the Rh- into the Ir-Scale for the Electronic Properties of NHC Ligands. *J. Organomet. Chem.* **2009**, *694* (9–10), 1487–1492.
(126) Vorfalt, T.; Leuthaeusser, S.; Plenio, H. An [(NHC)(NHCEWG)RuCl2(CHPh)] Complex for the Efficient Formation of Sterically Hindered Olefins by Ring-Closing Metathesis. *Angew. Chemie, Int. Ed.* **2009**, *48* (28), 5191–5194, S5191/1–S5191/25.
(127) Iglesias, M.; Beetstra, D. J.; Kariuki, B.; Cavell, K. J.; Dervisi, A.; Fallis, I. A. Synthesis and Structural Features of Rhodium Complexes of Expanded Ring N-Heterocyclic Carbenes. *Eur. J. Inorg. Chem.* **2009**, No. 13, 1913–1919.
(128) Lavallo, V.; Mafhouz, J.; Canac, Y.; Donnadieu, B.; Schoeller, W. W.; Bertrand, G. Synthesis, Reactivity, and Ligand Properties of a Stable Alkyl Carbene. *J. Am. Chem. Soc.* **2004**, *126* (28), 8670–8671.
(129) Olivier, B.; Martin, H.; D., M. C.; David, M.; Guy, B. 31P NMR Chemical Shifts of Carbene–Phosphinidene Adducts as an Indicator of the π-Accepting Properties of Carbenes. *Angew. Chemie Int. Ed.* **2013**, *52* (10), 2939–2943.
(130) Liske, A.; Verlinden, K.; Buhl, H.; Schaper, K.; Ganter, C. Determining the π-Acceptor Properties of N-Heterocyclic Carbenes by Measuring the 77Se NMR Chemical Shifts of Their Selenium Adducts. *Organometallics* **2013**, *32* (19), 5269–5272.
(131) Verlinden, K.; Buhl, H.; Frank, W.; Ganter, C. Determining the Ligand Properties of N-Heterocyclic Carbenes from 77Se NMR Parameters. *Eur. J. Inorg. Chem.* **2015**, *2015* (14), 2416–2425.
(132) Renner, C. A.; Greene, F. D. No Title. *J. Org. Chem.* **1976**, *41*, 2813.
(133) Otwinowski, Z.; Minor, W. [20] Processing of X-Ray Diffraction Data Collected in Oscillation Mode. *Methods Enzymol.* **1997**, *276*, 307–326.
(134) Sheldrick, G. M. No Title. *Acta. Cryst.* **2008**, *A64*, 112.

(135) Biju, A. T.; Hirano, K.; Froehlich, R.; Glorius, F. Switching the Electron-Donor Properties of N-Heterocyclic Carbenes by a Facile Deprotonation Strategy. *Chem. - An Asian J.* **2009**, *4* (12), 1786–1789.
(136) Benhamou, L.; Vujkovic, N.; Cesar, V.; Gornitzka, H.; Lugan, N.; Lavigne, G. Facile Derivatization of A "chemo-active" NHC Incorporating an Enolate Backbone and Relevant Tuning of Its Electronic Properties. *Organometallics* **2010**, *29* (11), 2616–2630.
(137) Mushinski, R. M.; Squires, B. M.; Sincerbox, K. A.; Hudnall, T. W. Amino-Acrylamido Carbenes: Modulating Carbene Reactivity via Decoration with an A,β-Unsaturated Carbonyl Moiety. *Organometallics* **2012**, *31* (13), 4862–4870.
(138) Cesar, V.; Mallardo, V.; Nano, A.; Dahm, G.; Lugan, N.; Lavigne, G.; Bellemin-Laponnaz, S. IMes-Acac: Hybrid Combination of Diaminocarbene and Acetylacetonato Sub-Units into a New Anionic Ambidentate NHC Ligand. *Chem. Commun. (Cambridge, United Kingdom)* **2015**, *51* (25), 5271–5274.